Non-invasive prediction of bone mechanical properties of the mouse tibia in longitudinal preclinical studies

Sara Oliviero

Doctor of Philosophy

Supervisors:
Dr Enrico Dall'Ara
Prof Timothy Skerry

Internal examiner: Dr Claudia Mazzà
External examiner: Prof Michael Fagan

The University of Sheffield
Faculty of Medicine, Dentistry & Health
Department of Oncology and Metabolism

January 2019

ACKNOWLEDGEMENTS

I would like to acknowledge all the people who supported me throughout my PhD, such an important time for my career and my life.

First of all, I am very thankful to my supervisor Dr Enrico Dall'Ara for his constant support and for being an excellent example of researcher. Enrico always guided me and encouraged my independence at the same time. My work and professional development would not have been possible without him.

I also would like to acknowledge my second supervisor Prof Tim Skerry for the fruitful discussions and useful advice.

I want to thank my wonderful sister Valentina and my parents, Fortunato and Adriana. Being away from them has been sometimes hard. I want to thank them for the lovely little things they do every day for me. I also want to thank Nadia for our amazing 15-years-long friendship.

I have been very lucky to join the Integrative MusculoSkeletal Biomechanics (IMSB) group, excellent researchers and wonderful colleagues. I thank Dr Yuan Chen and Dr Maya Boudiffa who helped me so much at the beginning of my PhD. I also thank Dr Mario Giorgi for the many times we worked together, a great experience not only from the scientific point of view. I have been very lucky to start my PhD 'journey' at the same time as Ivan, a great friend and pianist! Thanks to Cristiana for being an amazing friend and flatmate. I also thank Andrè for cheering me up in stressful moments!

Lastly, I would like to kindly acknowledge my funding: the Engineering and Physical Sciences Research Council (EPSRC, MultiSim project, Grant number: EP/K03877X/1) and the National Centre for Replacement, Refinement and Reduction of Animals in Research (NC3Rs, Grant numbers: NC/K000780/1 and NC/R001073/1). This work would not have been possible without their support.

PUBLICATIONS IN SCIENTIFIC JOURNALS

Oliviero, S., Lu, Y., Viceconti, M. & Dall'Ara, E. 2017. Effect of integration time on the morphometric, densitometric and mechanical properties of the mouse tibia. *Journal of Biomechanics,* 65**,** 203-211.

Oliviero, S., Giorgi, M., Dall'Ara, E. 2018. Validation of finite element models of the mouse tibia using digital volume correlation. *Journal of the Mechanical Behavior of Biomedical Materials,* 86, 172-184.

PRESENTATIONS IN INTERNATIONAL CONFERENCES

Oliviero S, Chen Y, Lu Y, Boudiffa M, Bellantuono I, Viceconti M, Dall'Ara E. Reduction of radiation dose for *in vivo* microCT imaging of the mouse tibia, 22nd Congress of the European Society of Biomechanics (ESB), 10 – 13 July 2016, Lyon, France. *Oral presentation*.

Oliviero S, Giorgi M, Dall'Ara E. Validation of microCT-based Finite Element models of the mouse tibia using Digital Volume Correlation, 23rd Congress of the European Society of Biomechanics (ESB), 2 – 5 July 2017, Seville, Spain. *Oral presentation*.

Oliviero S, Giorgi M, Dall'Ara E. Validation of Finite Element models of the mouse tibia for preclinical applications, 6th European Conference on Computational Mechanics (ECCM), 11 – 15 June 2018, Glasgow, United Kingdom. *Oral presentation*.

Oliviero S, Boudiffa M, Miller RA, Bellantuono I, Dall'Ara E. Effect of age on the morphological and mechanical properties of the mouse tibia, 8th World Congress of Biomechanics (WCB), 8 – 12 July 2018, Dublin, Ireland. *Poster presentation*.

ABSTRACT

The mouse tibia is a common site to investigate bone remodelling and the effect of treatments preclinically. It can be monitored using *in vivo* micro-Computed Tomography (microCT) imaging in order to track longitudinal changes in its morphometric and densitometric properties. Additionally, microCT images can be converted into micro-Finite Element (microFE) models for the non-invasive estimation of mechanical properties. Therefore, the combination of *in vivo* imaging and microFE modelling can provide comprehensive analyses about bone changes over space and time. However, repeated ionizing radiation exposure can have a significant effect on the bone properties; also, microFE models need to be validated against experimental measurements before application. The aim of this PhD project was to provide the best practice for the definition and validation of the *in vivo* microCT scanning procedure for the mouse tibia in preclinical studies. First, different scanning protocols have been tested by quantifying the accuracy of the image-based measurements against high resolution scans. One of the procedures has been selected as the best compromise between measurement accuracy and nominal radiation dose. Afterwards, microFE predictions of local and structural mechanical properties obtained using the selected scanning protocol have been validated. The experimental data for the validation has been obtained using the Digital Volume Correlation (DVC) approach, the only method which can provide volumetric measurements of local displacements under loading. Good to excellent correlations between the measured and predicted displacements were found. Errors in predictions of structural properties were in the order of 10-15%. Lastly, the protocol has been tested *in vivo*. The right tibia of 24 mice has been scanned *in vivo* five times, while the left tibia has been used as non-irradiated control. Non-significant or minimal radiation effects were found on the morphometric, densitometric and mechanical properties of the tibia. In conclusion, a scanning procedure for longitudinal *in vivo* microCT imaging of the whole mouse tibia has been defined and validated. The protocol will be used in future studies for investigating the effect of bone interventions.

ABBREVIATIONS

B6: C57BL/6 mouse

BAL: BalbC mouse

BMC: bone mineral content

BMD: bone mineral density

Ct.Ar: cortical bone area

Ct.Ar/Tt.Ar: cortical area fraction

Ct.Th: cortical thickness

DIC: Digital Image Correlation

DVC: Digital Volume Correlation

IT: integration time

LS1: load step 1

LS2: load step 2

LS3: load step 3

microCT: micro-Computed Tomography

microFE: micro-Finite Element

NS: nodal spacing

OVX: ovariectomy

PTH: parathyroid hormone

Tb.BV/TV: trabecular bone volume fraction

Tb.N: trabecular number

Tb.Sp: trabecular separation

Tb.Th: trabecular thickness

TMD: tissue mineral density

Tt.Ar: total cross-sectional area

WT: wild type

TABLE OF CONTENTS

CHAPTER 1

INTRODUCTION AND THEORETICAL BACKGROUND

SUMMARY

Bone is a complex tissue and understanding how it adapts to external stimuli is important to develop new treatments for bone diseases. Mouse models are commonly used for this purpose and for testing new interventions before clinical trials. In mouse models, *in vivo* micro-Computed Tomography (microCT) imaging can be used to monitor bone over time and therefore assess the effect of interventions longitudinally. Also, microCT images can be converted into micro-Finite Element (microFE) models for predicting biomechanical properties non-invasively. Therefore, the combination of *in vivo* microCT imaging and FE modelling is a powerful tool for comprehensive investigation of bone adaptation.

The aim of this study is to define and validate a suitable *in vivo* microCT scanning procedure for the investigation of morphometric, densitometric and biomechanical properties of the mouse tibia in preclinical studies. This is obtained through the following three objectives: 1) to select a scanning procedure which constitutes a compromise between image quality and radiation dose; 2) to validate microCT-based microFE models of the tibia obtained using the selected scanning procedure against DVC experimental measurements; 3) to quantify the effect of repeated *in vivo* imaging in order to confirm that the selected scanning procedure is acceptable for longitudinal application.

In this chapter, an introduction about the techniques used in this study is provided. First of all, an introduction about bone tissue and the mouse tibia is given. Subsequently, the principles of microCT imaging and FE modelling are described.

1.1 INTRODUCTION

Bone is a complex tissue, characterized by a multiscale structure. At the tissue level, bone undergoes modelling and remodeling, which aim at improving its mechanical competence at the macroscale (Lanyon, 1987, Dunlop et al., 2009, Kameo et al., 2018). These processes are mechano-regulated, which gives bone the ability to adapt to external stimuli in order to optimize its local and structural mechanical properties according to subject-specific or environmental needs. For example, it has been reported that exercise increases bone mass in different populations, including prepubescent children and premenopausal women (Fuchs et al., 2001, Kato et al., 2005, Vainionpää et al., 2006). In bone diseases, e.g. osteoporosis, this ability is impaired, leading to bone loss, higher fragility and higher risk of fracture (Melton et al., 2003). It is estimated that the rate of mortality is 20-30% in patients who underwent an osteoporotic hip fracture (Johnell and Kanis, 2005) and costs associated to treatments are significant ($25.3 billion expected by 2025 in the United States) (Li et al., 2015). Therefore, developing effective bone interventions (e.g. physical activity and/or pharmacological treatments) is crucial for improving the quality of life in patients and for reducing the costs associated to their treatment. In this framework, animal models are used to test potential interventions before clinical translation, as required by regulatory bodies. A common model applied for this purpose is the mouse tibia, which has the advantage that it can be imaged *in vivo* longitudinally. This is achieved by using micro-Computed Tomography (microCT) imaging, which has become the gold standard for imaging rodents bones *in vivo* since the mid-2000s (Bouxsein et al., 2010). With this technique, small rodents can be monitored over time by acquiring multiple images at subsequent time points, which provide accurate information about spatio-temporal bone changes. MicroCT imaging has been used in many different applications, including the investigation of bone growth, bone response to mechanical loading and to pharmacological treatments (Brodt and Silva, 2010, Levchuk et al., 2012, Razi et al., 2015). The information obtained from microCT images includes the three-dimensional bone geometry at the microstructural level and the local mineral density. Additionally, microCT images can be converted into micro-

Finite Element (microFE) models, which can predict the local and structural mechanical properties of the tibia non-invasively, if properly validated against experimental measurements. Therefore, the combination of longitudinal imaging and finite element modelling can be used to comprehensively assess how bone interventions affect the bone structure and mechanical competence in mice. Two main limitations are currently associated with this approach, which have been the focus of this PhD project. The first one is related to the potential detrimental effects of repeated ionising radiation exposure on bone, while the second one is the lack of validation of the prediction of biomechanical properties of the mouse tibia with microCT-based microFE models. These are further discussed in Chapter 2, where relevant literature is reported.

The aim of this chapter is to provide an introduction to bone tissue and the main techniques used to investigate the effect of interventions on it, including mouse models, microCT imaging and finite element modelling.

1.2 AIM OF THE STUDY

The combination of *in vivo* microCT imaging and microFE modelling constitutes a powerful tool for investigating the bone response to interventions in mouse models. The aim of this study is to provide the best practice procedure for the definition and validation of the *in vivo* microCT scanning procedure for the investigation of morphometric, densitometric and biomechanical properties of the mouse tibia in preclinical studies. This aim has been obtained by reaching the following three main objectives:

- To select a scanning procedure which provides the required accuracy in the image-based measurements of bone properties while reducing the induced radiation dose. In order to address this objective, four different scanning procedures have been used to measure the morphometric, densitometric and mechanical properties of four mouse tibiae. Measurement accuracy has been quantified against high resolution images. The best procedure has been selected based on both the accuracy of the obtained measurements and the associated radiation dose (Chapter 3).

- To validate the microFE models obtained using the selected scanning procedure at both the local and structural level. The DVC method has been applied to six tibiae to measure local displacements experimentally, which have been compared to the model predictions. Global stiffness and strength have also been measured experimentally and compared to those estimated from the models (Chapter 4).
- To evaluate the effect of repeated microCT scans *in vivo*, associated with the selected scanning procedure. MicroCT images collected during a longitudinal study (performed by Dr Mario Giorgi in the framework of the MultiSim project, EPSRC Grant number: EP/K03877X/1) were used for this analysis. The right tibia of 20 mice was scanned *in vivo* at multiple time points, while the left tibia was used as non-irradiated control. The effect of radiation was measured on the morphometric, densitometric and mechanical properties by comparing the right and left tibiae (Chapter 5).

1.3 BONE TISSUE

Bone is a hard tissue, which has the main functions of supporting the body and protecting internal organs, as well as serving for calcium storage (Cowin et al., 1987, Kameo et al., 2018). According to their shape, bones can be classified in long, short and flat. Generally, long bones have a load-bearing function mainly (e.g. the femur and tibia), while flat bones have protective function (e.g. the skull). Histologically, bone tissue can be classified in cortical and trabecular bone. Cortical bone is characterised by a porosity of 5-10% and constitutes approximately the 80% of the skeleton (Cowin et al., 1987). Trabecular bone is characterised by a porosity of 45-95% and its geometrical structure is a complex three-dimensional network of rods and plates (Fig. 1.1). In long bones, the diaphysis (shaft) is mainly made of cortical tissue, while trabecular bone is located at the epiphyses, facilitating the transmission of the load through the joints (Silva and Gibson, 1997). At the microstructural level, bone is a composite material made of collagen fibres mineralised by hydroxyapatite ($Ca_{10}(PO_4)_6OH_2$) crystals, organised in a complex hierarchical arrangement (Cowin et al., 1987).

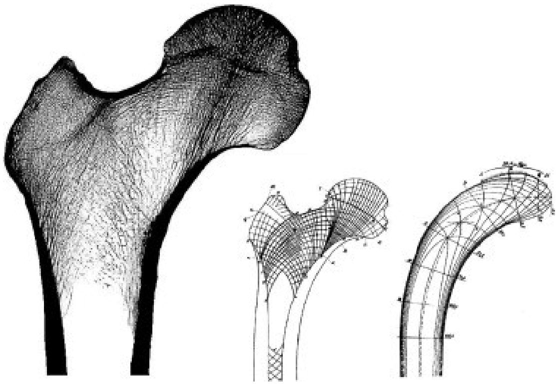

Figure 1.1*. Trabecular architecture in the mid-frontal section of the proximal femur (left). To the right comparison between a sketch of the trabeculae by the anatomist Meyer and the trajectories of principal stresses in a crane model analysed by Culmann in the second half of the 19th century (adapted from (Huiskes, 2000)). Image reproduced from (Fratzl and Weinkamer, 2007).*

At this scale, bone undergoes continuous renewal processes (modelling and remodelling), which are carried out and regulated by bone cells. The three main cell types present in bone are osteoblasts (bone forming cells), osteoclasts (bone resorbing cells) and osteocytes. Both modelling and remodelling are believed to be triggered by mechanical stimuli as proposed by Wolff's law (Wolff, 1870, Wolff, 2010). In particular, osteocytes, which are embedded in the bone matrix, are believed to sense the local magnitude of strains and to communicate with osteoblasts and osteoclasts through biochemical signalling in order to regulate the adaptation processes (Lanyon, 1987). In modelling, bone adaption to external loads is achieved by new bone formation in the locations of high strains and bone resorption in those of low strains (Dunlop et al., 2009). In remodelling, the two processes are coupled, with osteoclast activity followed by osteoblast activity at the same location (Dunlop et al., 2009). Through these processes, an optimised structure at the tissue scale is achieved, as observed for example in the human femur, where trabeculae orientation is aligned with the principal stress directions (Fig. 1.1).

Although there is a large body of evidence supporting the hypothesis that bone adaptation is mechano-regulated, the underlying mechanisms are still not fully understood (Kameo et al., 2018). Nevertheless, investigating the bone adaptation process is essential to develop effective treatments for bone diseases. In this framework, animal models are commonly used to obtain further insight into the remodelling mechanisms and to test potential interventions preclinically.

1.3.1 Mouse models

Mouse models are commonly used for investigating bone adaptation (Birkhold et al., 2016, Brodt and Silva, 2010, Holguin et al., 2014, Main et al., 2014, Schulte et al., 2013b, Silva et al., 2012). Their main advantage is the possibility to scan bones at high resolution *in vivo* (Paragraph 1.4.6), which provides information about bone changes over space and time. Another advantage is the environmental controllability, e.g. it is possible to control the mouse diet, to test different drug dosages and regimes of administration, as well as to control the amount of load applied on the bone of interest by using passive loading (Paragraph 2.2.3). The most common strains used in bone research are C57BL/6 (Birkhold et al., 2016, Holguin et al., 2014, Klinck et al., 2008, Main et al., 2014) and BalbC mice (Brodt and Silva, 2010, Klinck et al., 2008). In terms of anatomical sites, the tibio-fibular complex and the 6th caudal vertebra are commonly used. Studies on the caudal vertebra have investigated the bone response to mechanical loading and the relationship between local strains and bone apposition and resorption (Levchuk et al., 2014, Schulte et al., 2013a). The main advantage of focusing on the vertebra is the presence of a large amount of trabecular bone, whose behaviour is of interest since it seems to be more mechano-responsive compared to cortical tissue (Schulte et al., 2013a). On the other hand, for the caudal vertebra, which is located in the mouse tail, it is more difficult to evaluate the physiological loading, and its mechano-responsiveness could be different from that of a long bone. Additionally, applying an external load to the vertebra is an invasive procedure, requiring surgically implanting two pins in the adjacent vertebral bodies (Schulte et al., 2013a). Therefore, the focus of this study was the tibia, which is a load-bearing bone in physiological conditions and can be passively loaded non-invasively (Paragraph 2.2.3), by applying a load between the flexed knee and ankle (De Souza et al., 2005).

1.3.2 Mouse tibio-fibular complex

While in humans the tibia and fibula are two separate bones, in the mouse they are fused at the distal extremity (Fig. 1.2), therefore they are referred to as the tibio-fibular complex (Bab et al., 2007). The total length of the tibia is about 15-20 mm, while the diameter at the midshaft is about 800-1200 μm. At the proximal side, the tibia articulates with the femur through the medial and lateral condyles, while at the distal side it articulates with the talus and calcaneus through the medial and lateral malleoli (Fig. 1.2). Towards the proximal extremity, the tibia is characterised by a natural curvature. At the level of maximal convexity, the tibial ridge is present and the cross-sectional area is maximal, which improves the bending stiffness (Bab et al., 2007). The proximal epiphysis of the bone is characterised by the presence of the growth plate, which separates the condyles from the shaft (Fig. 1.2). The growth plate is made of a cartilaginous non- or partially mineralised tissue and is responsible of the majority of the tibial longitudinal growth (Bab et al., 2007). Above the growth plate, the epiphyseal trabeculae are present, while just below the growth plate there is the primary spongiosa, which is a mineralised but non-organised trabecular structure. Distally from the primary spongiosa, a minimal amount of trabecular bone is present, which extends for approximately 1 mm. No trabecular tissue is present in the remaining bone and the diaphysis of the tibia is made of cortical bone only. The proximal fibula is connected to the tibia through a cartilaginous tissue, while distally they are connected through the tibio-fibular junction, which is located at approximately 9 mm from the proximal end. The proximal growth plate and the tibio-fibular junction are often used as anatomical landmarks for morphometric analyses (Paragraph 2.2.1).

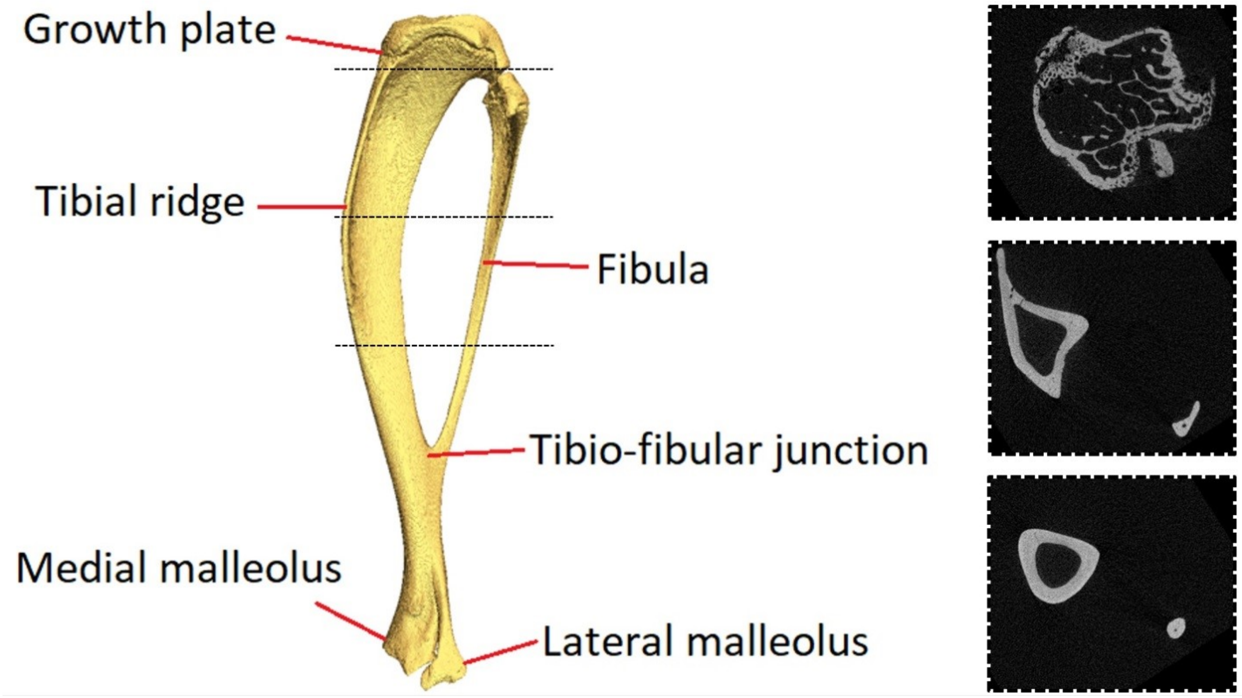

Figure 1.2. *Rostro-lateral view and cross-sections of the mouse tibio-fibular complex.*

1.4 MICRO-COMPUTED TOMOGRAPHY (MICRO-CT) IMAGING

Micro-Computed Tomography (microCT) imaging was introduced for the first time in 1989 (Feldkamp et al., 1989) and is now considered the gold standard for assessing the bone architecture in rodents non-destructively (Bouxsein et al., 2010). The following paragraphs describe how microCT images are acquired and analysed in order to obtain morphometric and densitometric measurements. It is also reported how microCT imaging is applied *in vivo* and how radiation dose induced on the animal is estimated.

1.4.1 Working principle

In microCT, bone is exposed to X-rays at multiple viewing angles and attenuation coefficients are used to reconstruct a 3D image of the bone. In the final image, each voxel is associated with a grey level, which is proportional to the local density of the material. In *ex vivo* applications, the spatial resolution achieved can be as low as a few microns, while for *in vivo* application it is typically around 10 μm.

The main components of a microCT system are the X-ray source, the collimator and the detector

(Fig. 1.3) (Bouxsein et al., 2010). The X-ray source is composed of a cathode and an anode placed into a vacuum tube, to which a voltage is applied. This provokes the emissions of electrons from the cathode, which are then accelerated and collected at the anode. The high-speed collision between the electrons and the anode releases X-ray photons. In microCT systems, the spectrum of energy is polychromatic, since the emitted X-ray photons are characterised by a range of wavelengths and therefore a range of energies. The collimator and filters, placed between the X-ray source and the sample, are used to narrow the energy spectrum (Kazakia et al., 2008). After that, the beam passes through the sample where X-rays are attenuated. Lastly, the beam exiting the sample is detected by a 2D charge-coupled device (CCD) array.

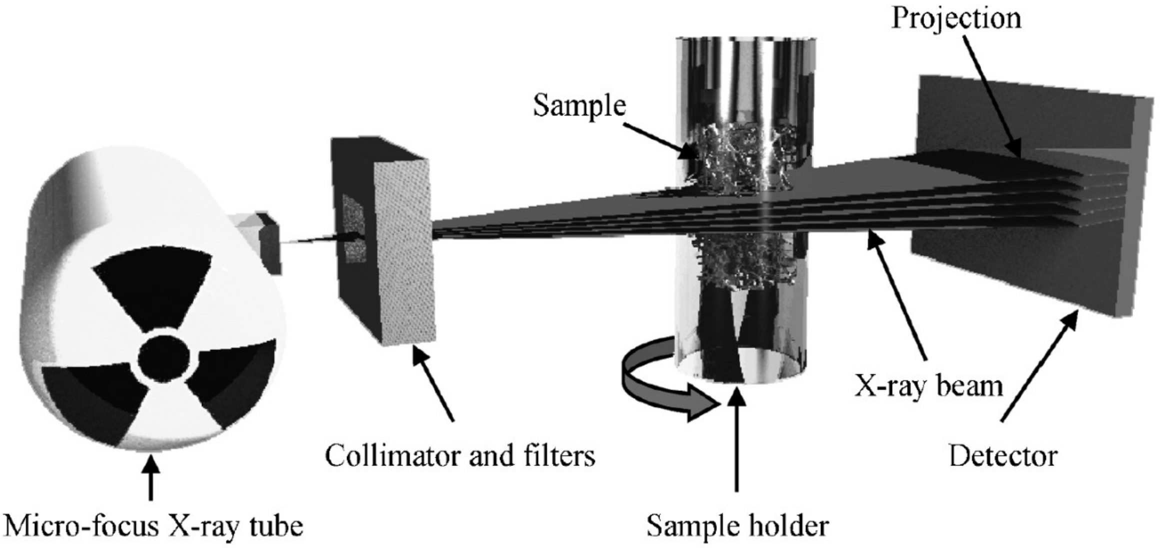

***Figure 1.3**. Key components and operating principle for standard desktop mCT scanner. A microfocus X-ray tube emits X-rays that are collimated and filtered to narrow the energy spectrum. The X-rays pass through the object and are recorded by a 2D charge-coupled device (CCD) array. A full scan involves a set of projections under different rotations of the object. (Image reproduced with permission from (Stauber and Müller, 2008)). Image reproduced with permission from (Bouxsein et al., 2010).*

For a homogeneous material of thickness *x*, the attenuation follows the following law

$$I = I_0 \, e^{-\mu x} \tag{1.1}$$

where I_0 is the intensity of the incident beam and I is the intensity of the exiting beam, from which the attenuation coefficient of the material μ [mm^{-1}] can be obtained. For heterogeneous materials and complex geometries, the spatial distribution of local attenuation coefficients is obtained by rotating the sample and acquiring projections at multiple viewing angles. The three-dimensional image is reconstructed by using back-projection algorithms (Bouxsein et al., 2010).

The parameters defining a scanning procedure are the voltage applied to the X-ray tube [kVp], the current generated in the X-ray tube [µA], the voxel size [µm], the number of projections (or alternatively the rotation step between subsequent projections [°]), the integration time (time the sample is exposed to radiation at each rotation step [ms]) and the frame averaging (number of images acquired at each rotation step). Increasing the number of projections, the integration time and frame averaging contribute to improve the image quality (Campbell and Sophocleous, 2014). However, longer scans are not always feasible due to time constraints and costs. Moreover, increasing the scanning time results usually in an increased induced ionising radiation, which is fundamental to take into account for *in vivo* applications.

1.4.2 Beam hardening artifacts

Beam hardening artifacts are caused by the fact that the spectrum of energy produced by the X-ray source is polychromatic (i.e. it contains photons characterised by different wavelengths). The portion of the beam characterised by lower energy (longer wavelengths) is preferentially attenuated by the sample, while the high-energy portion (higher wavelengths) passes through the sample more easily. Therefore, the mean energy of the beam exiting the sample is higher compared to the energy of the incident one, which is referred as beam hardening. During the reconstruction phase, when the 2D images collected by the CCD array are back-projected, this results in the presence of lower grey levels in the inner portions of the sample, especially for thicker structures (Ritman, 2004). Additionally, beam hardening results in the sample being exposed to an amount of ‘useless’ radiation, since the lower-energy portion of the spectrum, which does not exit the sample, does not produce measurable information (Ritman, 2004). To reduce beam hardening artifacts, an aluminium or copper/aluminium filter is placed between the X-ray source and the sample, which stops the lower-energy portion of the beam (Bouxsein et al., 2010). Additionally, correction algorithms have been developed, which are applied during the reconstruction phase (Kazakia et al., 2008, Mulder et al., 2004, Nuzzo et al., 2002). These are based on scanning a step wedge phantom characterised by increasing thickness, which is used to derive beam hardening correction factors in function of the structure thickness.

1.4.3 Density measurements

In microCT images, the grey level associated to each voxel is a measurement of the local attenuation coefficient, which can be linked to the local density of the material if the system is properly calibrated. The most common approach for calibration is based on scanning a phantom of known density. Hydroxyapatite (HA) phantoms are normally used for this purpose, which contain at least two insertions of known densities. After scanning the phantom, the average grey levels associated to each insertion in the image and the known densities are used to obtain a calibration curve (Bouxsein et al., 2010, Kazakia et al., 2008).

Nevertheless, voxel-level density measurements are affected by different sources of errors, including the setting of the scanning parameters (Paragraph 1.4.1) and beam hardening artifacts (Paragraph 1.4.2). Therefore, it is recommended that the average densities over larger regions of interest are calculated (Bouxsein et al., 2010). Tissue mineral density (TMD, [mgHA/cc]) is defined as the average density in the bone tissue, while bone mineral density (BMD, [mgHA/cc]) is defined as the average density in the total bone volume, which includes the marrow region (Tassani et al., 2011).

1.4.4 Image processing

Once the microCT images are acquired and reconstructed, the key steps in microCT image processing and analysis are registration, filtration and segmentation.

Accurate image registration is important in order to analyse consistent regions of interest across different samples or different microCT images of the same sample. Registration is the process of superimposing two images through a rigid 3D roto-translation according to an optimisation criterion (Boyd et al., 2006b). One of the images is used as reference, while the second is roto-translated and a metric is calculated in order to quantify the similarity between the two images. The procedure is repeated iteratively until the similarity is maximised. Different metrics can be used to find the optimal position and orientation, including mean squared difference of intensities, normalised correlation and mutual information. Among those, it has been shown that mutual information provides the best performance in terms of both accuracy and efficiency for registering microCT images of C57BL/6 mouse femur (Boyd et al., 2006b). After the registration procedure, the moved image is written in the new reference system by using an interpolator in order to compute the new grey levels. Lanczos interpolator is commonly used, which is associated with low interpolation errors (Meijering, 2000). It has been demonstrated that image registration significantly improves the reproducibility of morphometric parameters (Paragraph 1.4.5) measurements in the mouse and rat tibia (Nishiyama et al., 2010).

Image filtration is normally required in order to reduce the high frequency noise in the image, given by sources of error such as the setting of the scanning parameters and beam hardening artifacts. The most common filter used for microCT images of mouse bones is the Gaussian filter (Birkhold et al., 2014b, Levchuk et al., 2014). Gaussian filtration constitutes a compromise between the conflicting needs of reducing the high-frequency noise and preserving the sharpness of bone edges (Stauber and Müller, 2008).

Segmentation is the procedure for separating mineralised bone from the image background, which is usually done by using a global threshold. As shown in Fig. 1.4, the histogram (frequency plot) of a microCT image normally exhibits two peaks, of which the high-density one (around 1000-1300 mgHA/cc density) corresponds to bone and the low-density one corresponds to the background. Many different methods have been used in literature to select the threshold value, e.g. manual selection (Holguin et al., 2014, Patel et al., 2014), mean of the grey values corresponding to the peaks (Christiansen, 2016), one-third of the bone peak (Main et al., 2014), 25.5% of maximal greyscale value (Klinck et al., 2008), the Otsu algorithm (Bortel et al., 2015). There is no consensus about what is the best method, since each of them may introduce measurement errors according to the image quality (Christiansen, 2016). Guidelines suggest that images have to be inspected by comparing the binary image to the greyscale one in order to check the accuracy of the segmentation step (Bouxsein et al., 2010). More advanced segmentation techniques have also been proposed, e.g. the local threshold method (Waarsing et al., 2004b) and iterative algorithms (Meinel et al., 2005). However, their application remains limited due to their increased complexity.

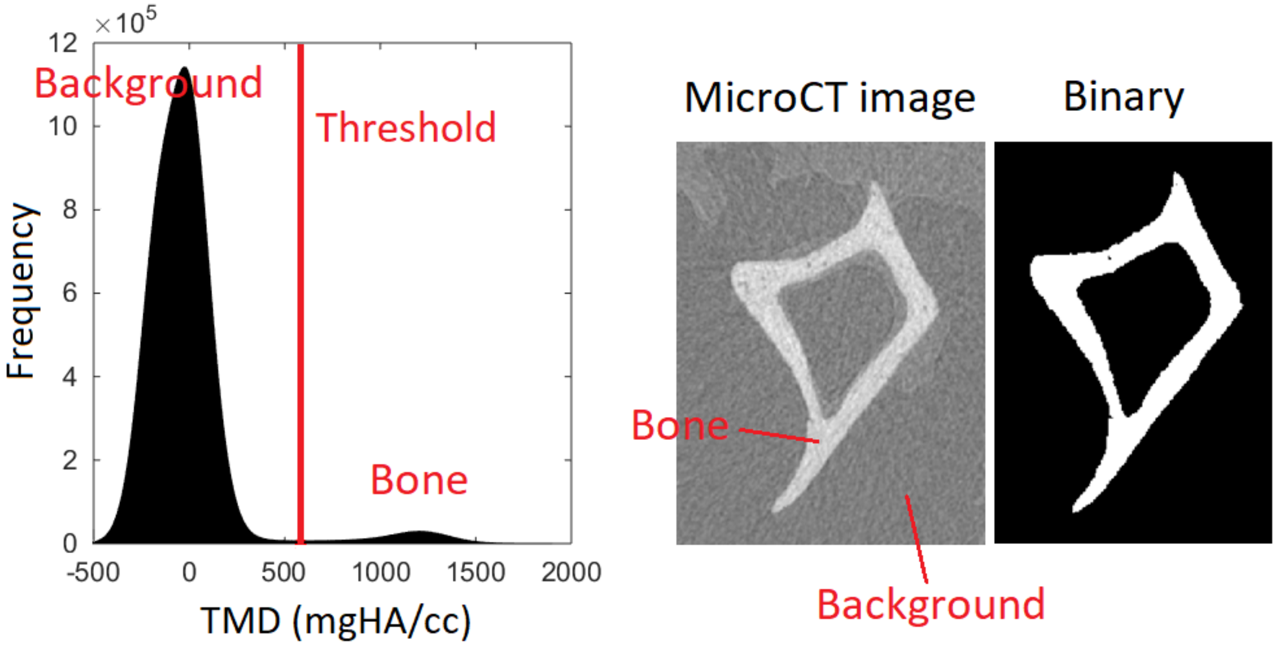

__Figure 1.4__: Example histogram (frequency plot) of a microCT image of the mouse tibia. The threshold value is used to segment the bone volume from the image.

1.4.5 Morphometric parameters

Morphometric parameters constitute the standard method to describe the bone microarchitecture, introduced in order to assure consistency among different studies and facilitate comparisons (Bouxsein et al., 2010). Two different sets of parameters have been defined in order to describe trabecular and cortical bone, respectively. The standard trabecular parameters include bone volume fraction Tb.BV/TV (ratio between the bone volume and the total volume of the region of interest, [%]), trabecular thickness Tb.Th (mean thickness of trabeculae, [µm]), trabecular separation Tb.Sp (mean distance between trabeculae, [µm]) and trabecular number Tb.N (average number of trabeculae per unit length, [1/mm]), which constitute the minimum recommended set of parameters to report in any animal study (Bouxsein et al., 2010). Bone volume fraction is easily obtained after the segmentation step as the ratio between the number of bony voxels and the total number of voxels in the volume of interest. The algorithm to obtain trabecular thickness and separation is based on fitting the largest possible sphere in the bone volume or background respectively, whose centre is located in each of the voxels of interest (Fig. 1.5). Tb.Th and Tb.Sp are subsequently calculated as the average diameter of all spheres. Lastly, trabecular number is obtained from the previous measurements as Tb.N = 1/(Tb.Th+Tb.Sp).

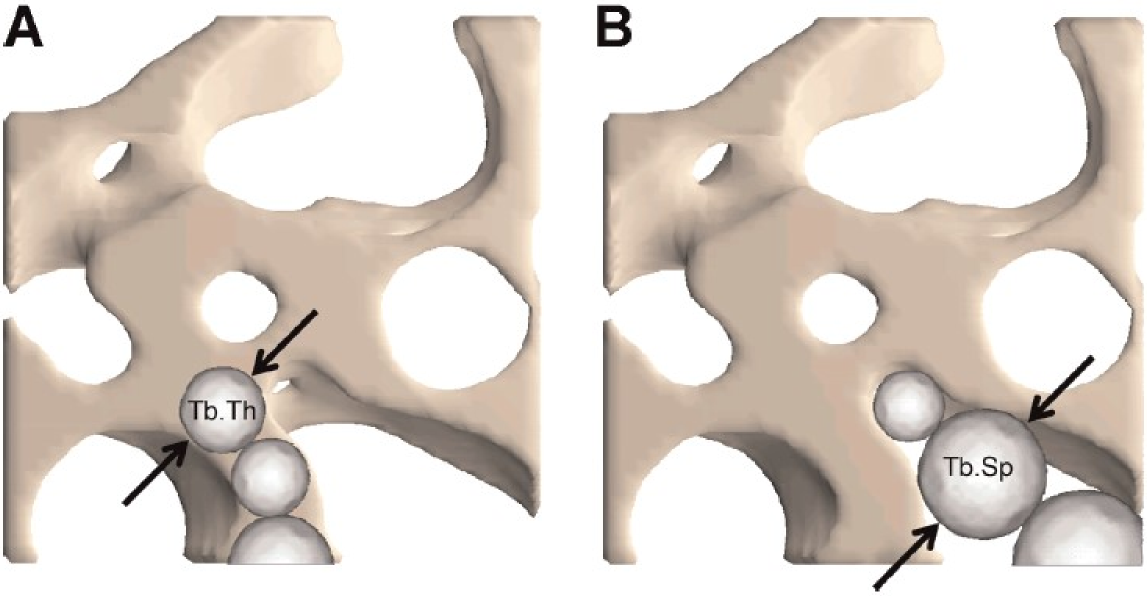

Figure 1.5*: Schematic representation of algorithm used for direct 3D method for calculating trabecular thickness (A) and separation (B). 3D distances are computed by fitting spheres inside the structure (i.e., to assess average trabecular thickness) or inside the background (marrow space, i.e., to assess average trabecular separation). The average diameter of the spheres represents the object thickness, and the standard deviation of the diameter represents the variability in the object thickness. (Image courtesy of Andres Laib, PhD, Scanco Medical AG.) Image reproduced with permission (Bouxsein et al., 2010).*

Additional parameters providing information about the trabecular geometry and arrangement are connectivity density Conn.D (degree of trabecular connectivity normalised by the total volume, [1/mm^2]), structure model index SMI (indicator of the trabecular structure assuming values between 0 and 3, which indicate a parallel-plates structure or cylindrical-rods respectively), and degree of anisotropy DA (indicator of the anisotropy of the structure, where 1 indicates isotropic structure and values >1 indicate increasing anisotropy).

For cortical analysis, standard morphometric parameters are total cross-sectional area (Tt.Ar, [mm^2], Fig. 1.6), cortical bone area (Ct.Ar, [mm^2], Fig. 1.6), cortical area fraction Ct.Ar/Tt.Ar (ratio between cortical bone area and total cross-sectional area, [%]), cortical thickness (Ct.Th, [μm]) (Bouxsein et al., 2010). Cortical areas are calculated as the average area across all slices belonging to the selected volume of interest. Cortical thickness is obtained by using the same approach applied for trabecular thickness, as described previously. Additional parameters commonly reported in literature include marrow area (Ma.Ar, [mm^2]), cortical porosity (Ct.Po, [%]), maximum moment of inertia (I_{max}, [mm^4]), minimum moment of inertia (I_{min}, [mm^4]), polar moment of inertia (J, [mm^4]).

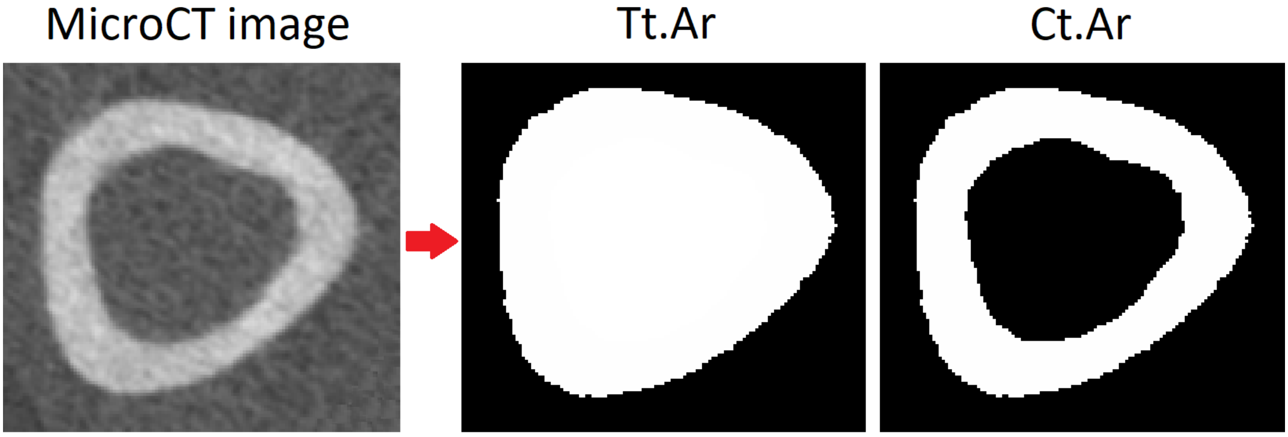

***Figure 1.6**: Example of a microCT cross-section of cortical bone, from which total cross-sectional area (Tt.Ar) and cortical bone area (Ct.Ar) are measured, after the segmentation step.*

1.4.6 *In vivo* microCT imaging

In standard cross-sectional studies, the effect of the intervention of interest is evaluated by scanning the bones *ex vivo* at the end of the study and subsequently comparing the intervention group to a control one (De Souza et al., 2005, Main et al., 2014, Moustafa et al., 2012). The main disadvantage of this approach is that inter-subject differences increase the variability of the results and a larger number of animals is required in order to detect the potential effects of the analysed intervention.

Additionally, no information can be obtained on the temporal development of the observed effects. In order to overcome this limitation, Waarsing and colleagues (2004a) proposed for the first time to use longitudinal *in vivo* microCT scans to assess the temporal changes in the tibia architecture of ovariectomised (OVX) rats. In longitudinal studies, each group of mice is monitored by acquiring multiple *in vivo* microCT images of the same bone at different time points. The variability of the obtained measurements is reduced by normalising the longitudinal data according to the baseline scan, so that relative changes are quantified for each mouse, resulting in a lower number of animals required (Dall'Ara et al., 2016). Additionally, it is possible to assess the temporal variations in the bone adaptation.

In vivo microCT scanning is performed while animals are under anesthesia, which is usually done by isoflurane inhalation (Birkhold et al., 2014, Klinck et al., 2008). A bed is used to support the mouse body, while the leg is fixed to a custom holder and positioned in the field of view of the microCT machine. In *in vivo* microCT machines, the X-ray source rotates around the field of view, in order to facilitate the positioning of the animal and the image acquisition. Compared to *ex vivo* scanning, in *in vivo* scanning a compromise between the scanning time and image quality needs to be found. First of all, there are concerns about the potential side effects of radiation exposure on the animal (Paragraph 2.2.4). Also, a longer scanning time increases the potential moving artifacts in the image, due to the animal breathing (Bouxsein et al., 2010). The time of anesthesia also needs to be limited in order to reduce the potential harm to the animal. Therefore, as mentioned previously, the image resolution achievable *in vivo* is approximately 10 μm. In general, in order to obtain reliable measurements of the bone microarchitecture, it is recommended that the spatial resolution of the imaging technique should be at least three-four times lower than the smallest feature of interest (Christiansen, 2016). In the case of the mouse tibia, trabecular thickness is in the range of 40-60 μm, which makes the spatial resolution achievable *in vivo* acceptable for resolving the structure.

1.4.7 Measurement of radiation dose

Radiation dose induced on the bone during *in vivo* imaging is estimated using an ionisation chamber probe, i.e. a sensor to detect radiation. It is recommended (Bouxsein et al., 2010) that the probe is placed into a tissue-equivalent plastic tube, mimicking the shielding provided by the soft tissues surrounding the bone, e.g. polyetherimide (PEI) or polymethyl methacrylate (PMMA). The measurement is repeated for different scanning protocols by varying each scanning parameter in the range of usage of the microCT scanner, so that a relationship between each scanning parameter and radiation dose is obtained. For example, radiation dose is linearly proportional to the integration time (IT) and to the number of projections acquired. Therefore when varying one (or both) of these parameters, the radiation dose associated to the current procedure (z) can be calculated by rescaling the dose associated to one of the standard scans (y), given that the other parameters do not vary:

$$Radiation\ Dose(z) = \frac{Radiation\ Dose(y)\ IT(z)\ Projections(z)}{IT(y)\ Projections(y)} \tag{1.2}$$

1.5 FINITE ELEMENT (FE) MODELLING

Understanding the mechanical behaviour of structures under loading is a problem of interest in many engineering applications. For simple geometries and material properties, an analytical solution can be found to describe how a structure of interest deforms given an applied load. However, for more complex problems an analytical solution can be difficult to obtain. The Finite Element (FE) method (Burnett, 1987, Fagan, 1996) was developed with the aim to find an approximate solution to problems characterised by complex geometries, material properties and boundary conditions. It was originally applied for solving traditional engineering problems, however its application to biomechanics progressively increased since 1990s (Fagan et al., 2002, Hou et al., 1998, Ulrich et al., 1998, van Rietbergen et al., 1995, Yeni and Fyhrie, 2001). In the following paragraphs, the theory of linear elasticity and the FE method are introduced. Non-linear material properties and contact are not introduced here since the models used in this work did not include them. Lastly, the Digital Volume Correlation (DVC) method is presented, which has been recently used for obtaining experimental data for the validation of FE models.

1.5.1 Linear elasticity

The theory of elasticity was firstly developed by Robert Hooke (1635-1703), based on the observation that for some materials (and simple geometry) the change in the total length (ΔL) under loading is proportional to the applied force (F) (Fig. 1.7). In the one-dimensional case, this linear elastic behaviour is described by the Hooke's law as:

$$F = k\,\Delta L \tag{1.3}$$

The coefficient k is the stiffness of the structure, which depends on both the geometry and the material properties. The above relationship can be rewritten as:

$$\sigma = E\,\varepsilon \tag{1.4}$$

by defining stress (σ) and strain (ε) as follows:

$$\sigma = F/A; \tag{1.5}$$

$$\varepsilon = \Delta L/L \tag{1.6}$$

where A is the cross-sectional area of the sample (Fig. 1.7). The coefficient E, independent from the geometrical dimensions of the sample, is called Young's modulus (or elastic modulus). In the three-dimensional case, the application of the load F also generates a strain in the transverse direction and a second parameter is needed to describe the response of the material, which is called Poisson's ratio, defined as:

$$\nu = -\frac{\varepsilon_x}{\varepsilon_z} \tag{1.7}$$

where ε_x is the transverse strain and ε_z is the axial strain. Similarly to what described for an axial load, if the force F is applied in a direction parallel to the surface A, the shear stress (τ) is defined as

$$\tau = F/A \tag{1.8}$$

When F is applied along x, shear stress is indicated as τzx, while if F is applied along y it is indicated as τzy, where the subscript z indicates that the surface A is perpendicular to the z axis (Fig. 1.7).

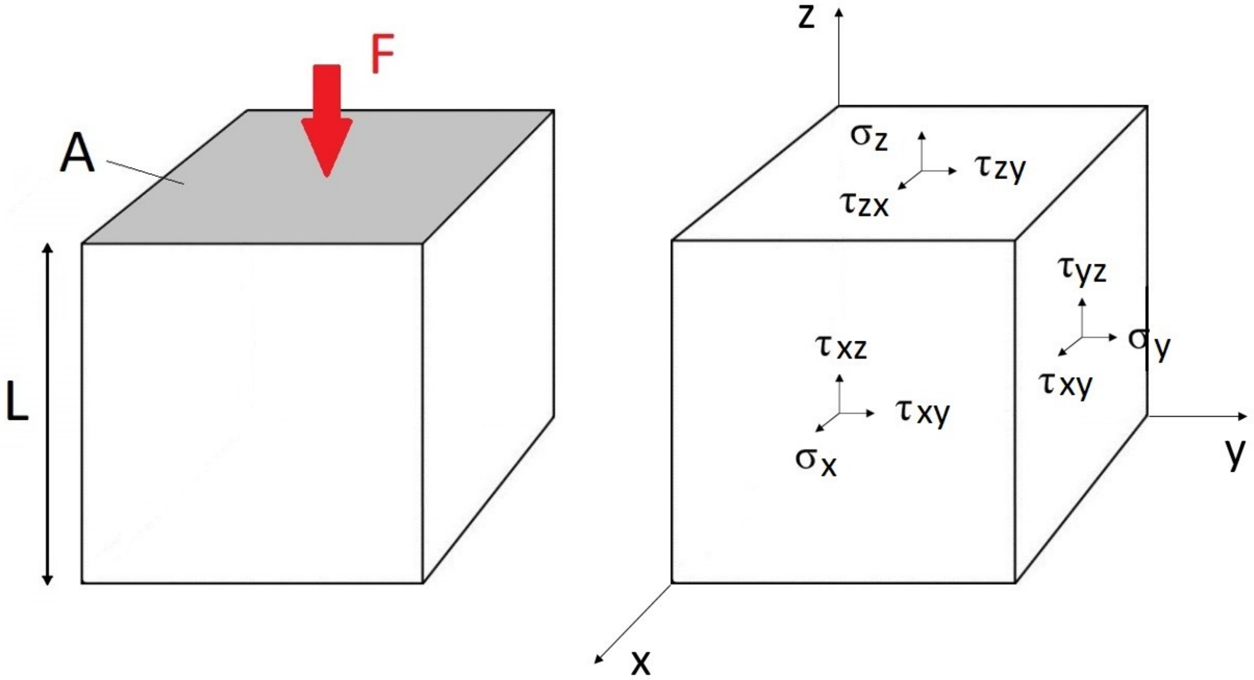

***Figure 1.7**: Schematic representation of a sample loaded in compression by a force F. L is the length of the sample in the z direction, while A is the cross sectional area. On the right side, the definition of axial (σ) and shear (τ) stresses in the Cartesian coordinates is reported.*

A material having the same properties in all directions is called isotropic. For describing the mechanical behaviour of an isotropic linear elastic material, Young’s modulus and Poisson’s ratio are the only parameters needed. By combining the above equations, axial (ε) and shear strains (γ)

under loading can be calculated as

$$\begin{bmatrix} \varepsilon_x \\ \varepsilon_y \\ \varepsilon_z \\ \gamma_{yz} \\ \gamma_{zx} \\ \gamma_{xy} \end{bmatrix} = \begin{bmatrix} \frac{1}{E} & -\frac{\nu}{E} & -\frac{\nu}{E} & 0 & 0 & 0 \\ -\frac{\nu}{E} & \frac{1}{E} & -\frac{\nu}{E} & 0 & 0 & 0 \\ -\frac{\nu}{E} & -\frac{\nu}{E} & \frac{1}{E} & 0 & 0 & 0 \\ 0 & 0 & 0 & \frac{1}{G} & 0 & 0 \\ 0 & 0 & 0 & 0 & \frac{1}{G} & 0 \\ 0 & 0 & 0 & 0 & 0 & \frac{1}{G} \end{bmatrix} \begin{bmatrix} \sigma_x \\ \sigma_y \\ \sigma_z \\ \tau_{yz} \\ \tau_{zx} \\ \tau_{xy} \end{bmatrix} \tag{1.9}$$

G is the shear modulus, equal to

$$G = \frac{E}{2\,(1+\nu)} \tag{1.10}$$

for isotropic materials. Materials exhibiting different behaviours in different directions are called anisotropic. Despite having anisotropic (Carnelli et al., 2011) and non-linear material properties (Bayraktar et al., 2004), bone tissue is often modelled as an isotropic linear elastic material in first approximation, which has provided good accuracy for predicting its mechanical response at both the structural (Schileo et al., 2008, Wolfram et al., 2010) and local level (Chen et al., 2017, Costa et al., 2017).

1.5.2 Principal strains

A structure subjected to a general loading scenario is characterised by a 3D strain condition. For each spatial location in the structure, it is possible to identify specific directions for which the normal strains are maximum (or minimum) and the shear strains are equal to zero. These strains are called principal strains and can be obtained as the eigenvalues of the strain tensor:

$$\begin{vmatrix} \varepsilon_x - \varepsilon_0 & \frac{1}{2}\gamma_{xy} & \frac{1}{2}\gamma_{xz} \\ \frac{1}{2}\gamma_{yx} & \varepsilon_y - \varepsilon_0 & \frac{1}{2}\gamma_{yz} \\ \frac{1}{2}\gamma_{zx} & \frac{1}{2}\gamma_{zy} & \varepsilon_z - \varepsilon_0 \end{vmatrix} = 0 \qquad (1.11)$$

The first principal strain ε_{11} is the most positive and represents the maximum tensile strain at the analysed location, while the third principal strain ε_{33} is the most negative one and represents the maximum compressive strain. The eigenvectors corresponding to each strain direction are called principal directions.

1.5.3 Finite Element (FE) method

In structures characterised by complex geometry and loading condition, the Finite Element (FE) method aims at finding an approximated solution for the distribution of field variables of interest (e.g. strains) numerically. The general approach is that the domain is discretised into elements of simple geometry, for which the elasticity equations are solved. Each element is described by a certain number of nodes, with three degrees of freedom (*x*, *y* and *z* coordinates), and shape functions for interpolating the solution between the mesh nodes. The most common 3D elements used for microFE modelling of bone structures are 8-noded linear hexahedral (van Rietbergen et al., 1995) and 10-noded quadratic tetrahedral elements (Polgar et al., 2001). The main advantage of 8-noded linear hexahedrons is that, given their simple geometry, the solution is relatively straightforward. On the other hand, they cannot recover the smooth boundaries of the bone surface and a good approximation of the real geometry can only be achieved by using smaller elements, which requires higher computational time and resources. 10-noded quadratic tetrahedrons can better approximate the bone surface, but require more complex approaches for the pre-processing (mesh generation) and solution.

In FE analysis, for each element *e*, the displacements (***u***) are approximated as:

$$u^{(e)} = N^{(e)}\, U^{(e)} \tag{1.12}$$

where ***N*** is a matrix containing the shape functions and ***U*** is a vector containing the unknown nodal displacements. Therefore, for the whole structure displacements are approximated by adding up the contributions from all elements E:

$$u = \sum_{e=1}^{E} u^{(e)} \tag{1.13}$$

The equilibrium state of the structure is obtained by minimising the energy of the system Π

$$\frac{\partial}{\partial U} \sum_{e=1}^{E} \Pi^{(e)} = 0 \tag{1.14}$$

The energy of the system Π is a function of the strain energy Λ and the work W done by the external forces F, which are defined as

$$\Pi = \Lambda - W = \frac{1}{2}\, U^T K\, U - U^T F \tag{1.15}$$

This gives the following equilibrium equation:

$$\sum_{e=1}^{E} (K^{(e)}\, U^{(e)} - F^{(e)}) = 0 \tag{1.16}$$

$\boldsymbol{K}^{(e)}$ is the stiffness matrix, which depends on the material properties assigned to each element. For isotropic linear elastic material properties, the stiffness matrix of each element is a function of the Young's modulus and Poisson's ratio (Paragraph 1.5.1). Lastly, the equilibrium equation for the whole structure, given by the contributions of all elements, can be rewritten as

$$K\,U = F \tag{1.17}$$

K is the global stiffness matrix, having dimension NxN, where N is the total number of degrees of freedom in the system, ***U*** (Nx1) is the vector containing the unknown displacements and ***F*** (Nx1) is a vector containing the external forces applied. By solving the above system of equations, the displacements over the whole structure are obtained, from which the strain distribution can be calculated by differentiation.

1.5.4 Validation of FE models

FE models are particularly useful to obtain predictions of quantities that cannot be directly measured, e.g. strains or stresses over the entire bone structure or mechanical properties *in vivo*. However, the model constitutes a simplified representation of the structure of interest, therefore the reliability of its predictions needs to be assessed before the model application. Validation is the process of comparing computational predictions to experimental data in order to assess its accuracy (Anderson et al., 2007). Different approaches have been used for validating FE predictions of strains and displacements in bone structures, which are reviewed in Paragraph 2.4.1. Briefly, strain gauge measurements (Fig. 1.8), Digital Image Correlation (DIC) and Digital Volume Correlation (DVC) can be used (Grassi and Isaksson, 2015). Among those, DVC is the only technique which can provide volumetric measurements of local displacements. In this study, DVC has been applied for the validation of FE models of the mouse tibia for the first time.

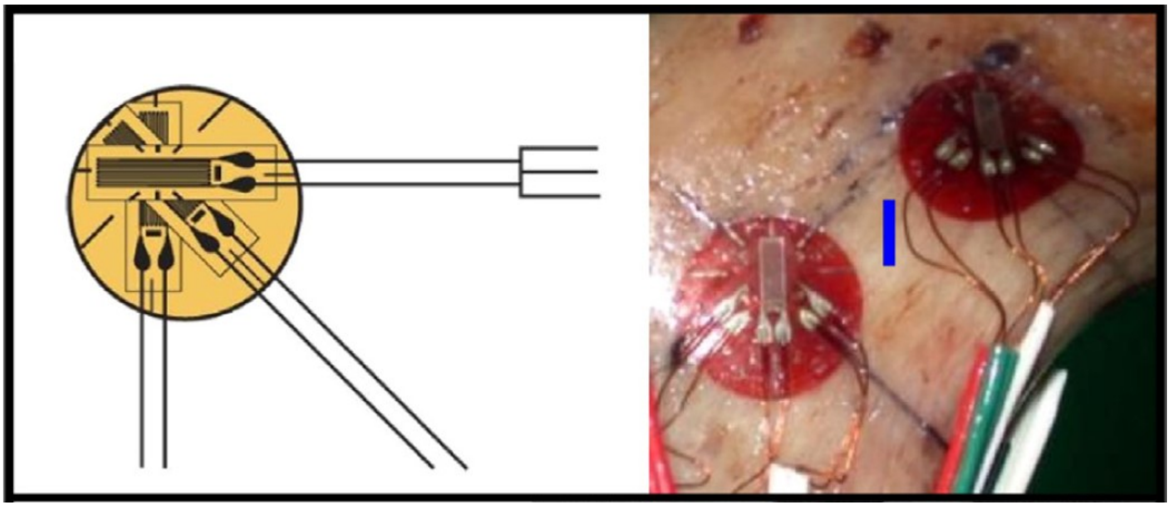

***Figure 1.8:** Strain gauges attached to the bone surface. Image reproduced with permission from (Grassi and Isaksson, 2015).*

1.5.5 Digital Volume Correlation (DVC)

In Digital Volume Correlation (DVC), 3D images acquired in different loading configurations are used to measure local displacements (Bay et al., 1999). DVC has been recently applied to microCT images of bone samples to characterise displacement and strain fields under loading (Grassi and Isaksson, 2015, Roberts et al., 2014) and to validate FE predictions of local displacements (Fig. 1.9) (Chen et al., 2017, Costa et al., 2017, Zauel et al., 2005).

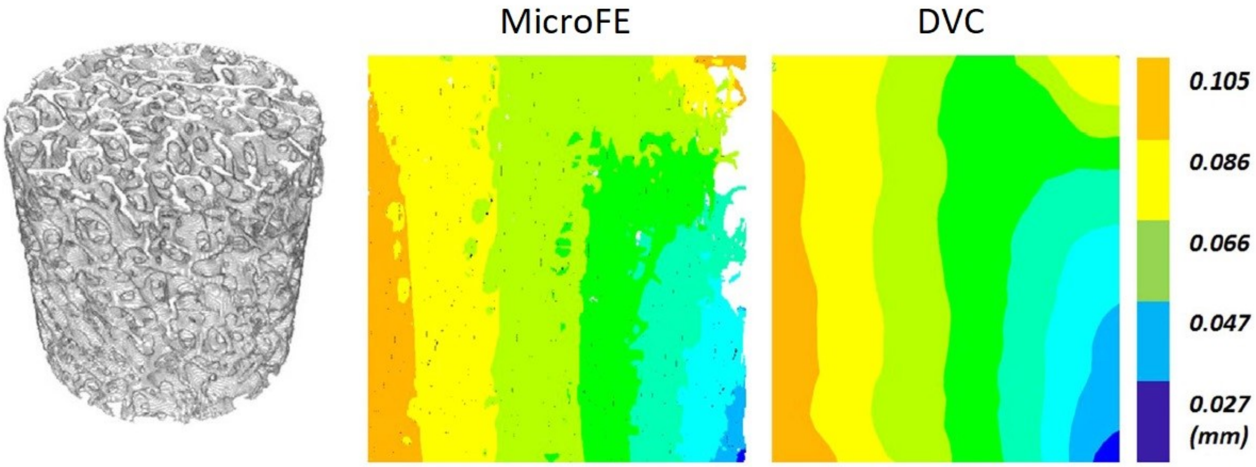

***Figure 1.9:** Contour plot of the displacement along the loading direction Z viewed in the coronal plane for a trabecular bone sample. Predictions from the microFE model and DVC measurements are reported. Adapted from (Chen et al., 2017).*

In DVC, local displacements are calculated by tracking the natural features of the sample from a microCT image acquired in a non-deformed configuration into one acquired under loading. In order to do this, two main approaches can be used, which are referred to as local and global approaches. In both cases, a grid (characterised by a specific nodal spacing, NS) is superimposed to the microCT images, thus dividing them into subsets. In local approaches, each subset is deformed according to a predicted displacement field and a similarity function between the images is calculated based on the microCT intensity values. This procedure is repeated iteratively in order to identify the displacement field which maximises the similarity between the images (Grassi and Isaksson, 2015, Palanca et al., 2015). In global approaches, the deformable registration is based on the continuity assumption on the displacement field, therefore the whole volume of interest is analysed at each iteration and the mapping of each subset depends on the adjacent ones (Barber et al., 2007, Dall'Ara et al., 2014). The displacements which map the first image into the second are calculated by solving the registration equations at each node of the grid and applying a trilinear interpolation between the nodes. The displacement field can also be differentiated to obtain the strain field. It has been reported that the global approach produces lower measurement errors compared to local approaches, but requires higher computational costs (Palanca et al., 2015).

The accuracy of DVC measurements is influenced by both the subset size and image quality. Previous studies reported that by increasing the subset size the measurement accuracy improves following a power law (Dall'Ara et al., 2014, Palanca et al., 2015). However, while for displacements a reasonable compromise can be achieved between accuracy and spatial resolution, for strains acceptable errors can only be obtained at very coarse resolutions. In trabecular bone specimens, the accuracy of DVC measurements of displacements is in the order of a fraction of the voxel for spatial resolutions as low as 5 voxels, while acceptable errors for strains (few hundreds of microstrains) are only achieved at a spatial resolution of 50 voxels (Palanca et al., 2015). In a recent work (Palanca et al., 2017), it has been shown that the accuracy of DVC strain measurements could be improved by using Synchrotron Radiation microCT (SR-microCT) images. However, the high resolution obtained with this technique is achieved by using very high radiation, which influences the material properties of the bone (Barth et al., 2010). Therefore, SR-microCT has only been applied to repeated scans of bone samples in the unloaded configuration, while its combination with mechanical testing is intrinsically limited (Palanca et al., 2017).

CHAPTER 2

MOTIVATION AND LITERATURE REVIEW

SUMMARY

Longitudinal studies on mouse models are used in bone research to investigate bone growth and adaptation to external stimuli. *In vivo* micro-Computed Tomography (microCT) imaging is used to monitor bone changes longitudinally. This technique has been applied to investigate the effect of ovariectomy, which is used as an animal model of osteoporosis, and potential bone treatments, including anabolic drugs (e.g. Parathyroid Hormone, PTH) and mechanical loading. The main disadvantage of longitudinal studies is that repeated radiation exposure can have a significant effect on the bone morphometry, which needs to be minimised by finding a compromise between image quality and radiation dose induced on the animal at each scan.

MicroCT images can also be converted into micro-Finite Element (microFE) models for predicting structural and local mechanical properties non-invasively. They have been mainly used to estimate strain distributions under loading in order to correlate the local mechanical stimulus to the biological response. FE predictions of strains or displacements for the mouse tibia have been validated using either strain gauge measurements or Digital Image Correlation (DIC). However, none of these methods can provide volumetric measurements, which can be overcome by using the Digital Volume Correlation (DVC) approach.

2.1 INTRODUCTION

The aim of this chapter is to review the application of microCT imaging and FE modelling on mouse models, and the main limitations associated with the current approaches, which have been the focus of this work. Longitudinal studies on the mouse tibia are important to investigate bone growth, remodeling and the effect of interventions. Relevant outputs of interest from longitudinal studies include changes in bone geometry and microstructure, changes in bone mineralization and in mechanical properties. The gold standard for monitoring bone *in vivo* is micro-Computed Tomography (microCT) imaging (Paragraph 1.4), which allows the acquisition of bone images at multiple time points, thus tracking its changes over time. Additionally, microCT images acquired *in vivo* can be converted into micro-Finite Element (microFE) models, which can estimate structural and local mechanical properties non-invasively and how they are affected by the studied intervention. The combination of *in vivo* imaging and microFE modelling also constitutes a very powerful tool for the non-invasive estimation of the spatial distribution of displacements and strains under loading, which cannot be directly measured *in vivo*.

Longitudinal *in vivo* imaging have been applied for the first time for investigating the effect of ovariectomy (OVX) on rats (Waarsing et al., 2004a). OVX is the surgical removal of the ovaries, which causes an oestrogen depletion leading to accelerated bone resorption (Laib et al., 2001), and is commonly used as a model for osteoporosis (Boyd et al., 2006a, Waarsing et al., 2004a). Another application is the investigation of developmental patterns, which constitute relevant background information for designing longitudinal studies and for the interpretation of the results (Buie et al., 2008). Lastly, the effect of anabolic interventions has been analysed, including pharmaceutical treatments (Campbell et al., 2014, Levchuk et al., 2012), mechanical loading (Birkhold et al., 2016) and their combination (Meakin et al., 2017).

MicroFE models based on microCT images have been mainly used to predict the strain distributions in the bone under loading, in order to characterise the strain environment induced by passive *in vivo* loading and to identify potential correlations between local mechanical stimuli and biological responses (Birkhold et al., 2016, Patel et al., 2014).

Two main limitations can be identified in the described approach. First of all, for the acquisition of multiple microCT images, the bone is repeatedly exposed to ionising radiation, which could affect the cell activity and bias the results of the study. In some studies, significant changes in the tibia microarchitecture have been reported associated with the repeated *in vivo* scans (Klinck et al., 2008, Willie et al., 2013). But importantly, no significant effects have been reported for other radiation doses or scanning regimes (Buie et al., 2008, Laperre et al., 2011), suggesting that the scanning protocol can be optimised in order to reduce the potential radiation effects. The second limitation is related to the lack of validation for microCT-based microFE models. In general, the credibility of model predictions is subject to validation against adequate experimental data (Anderson et al., 2007). For the mouse tibia, FE models have been validated using a limited amount of strain gauge measurements (Patel et al., 2014, Stadelmann et al., 2009), or using surface measurements of displacements acquired with Digital Image Correlation (DIC) (Sztefek et al., 2010). Therefore, a comprehensive volumetric validation is currently lacking. This could be performed by applying the Digital Volume Correlation (DVC) approach, which has been used on bone samples of different species (Chen et al., 2017, Costa et al., 2017, Zauel et al., 2005).

The aim of this PhD project is to address these limitations through the following main objectives: 1) selecting a scanning procedure which constitutes a compromise between image quality and radiation dose (Chapter 3); 2) validating the outputs of microCT-based microFE models of the tibia generated using the selected scanning procedure against experimental measurements obtained with DVC (Chapter 4); 3) quantifying the effect of repeated *in vivo* imaging associated with the selected scanning procedure (Chapter 5).

In this chapter, it is summarized how microCT imaging and FE modelling are used to measure the morphometric, densitometric and mechanical properties of the mouse tibia and to study the effect of bone interventions. Subsequently, the main limitations of the current approach are discussed.

2.2 MICRO-CT IMAGING OF THE MOUSE TIBIA

Micro-Computed Tomography (microCT) imaging is the gold standard for the high-resolution imaging of rodents' bones (Bouxsein et al., 2010). *Ex vivo* microCT can provide images of the bones with a voxel size down to a few microns, while *in vivo* microCT normally provides the best voxel size of approximately 10 μm, which constitute an adequate resolution given that the dimension of mouse trabeculae is approximately 40-60 μm (Martín-Badosa et al., 2003). The increasing usage of this technique made it necessary to define standard guidelines on how to analyse and report microCT measurements for rodents' bones (Bouxsein et al., 2010), which are summarised here since they have been applied throughout the whole study. In the following paragraphs, the analysis of microCT images is described, including measurement of standard morphometric parameters (Paragraph 2.2.1) and density measurements (Paragraph 2.2.2) for the mouse tibia. Subsequently, the main applications of *in vivo* imaging are summarized (Paragraph 2.2.3). Lastly, considerations about the effect of radiation exposure are reported (Paragraph 2.2.4).

2.2.1 Measurement of morphometric parameters in the mouse tibia

Standard morphometric analyses (Paragraph 1.4.5) in the mouse tibia are performed in two volumes of interest corresponding to the trabecular and cortical bone. As described before, trabecular bone in the mouse tibia is located at the proximal epiphysis, therefore the trabecular volume of interest is selected in this area (Fig. 2.1). Cortical bone can be selected either at the proximal end or, more commonly, at the midshaft (Fig. 2.1).

The trabecular volume of interest is defined by using the proximal growth plate as a reference to identify consistent volumes across different bones. Afterwards, trabeculae are selected by using either manual contouring or semi-automatic techniques (Buie et al., 2007, Kohler et al., 2007). The minimum recommended set of parameters to report in animal studies include bone volume fraction (Tb.BV/TV, [%]), trabecular thickness (Tb.Th, [μm]), trabecular separation (Tb.Sp, [μm]) and trabecular number (Tb.N, [1/mm]) (Bouxsein et al., 2010).

For cortical analysis, the volume of interest is normally selected by using as a reference the tibial midshaft or the tibio-fibular junction. The minimum recommended set of parameters include total cross-sectional area (Tt.Ar, [mm^2]), cortical bone area (Ct.Ar, [mm^2]), cortical area fraction (Ct.Ar/Tt.Ar, [%]), cortical thickness (Ct.Th, [µm]) (Bouxsein et al., 2010).

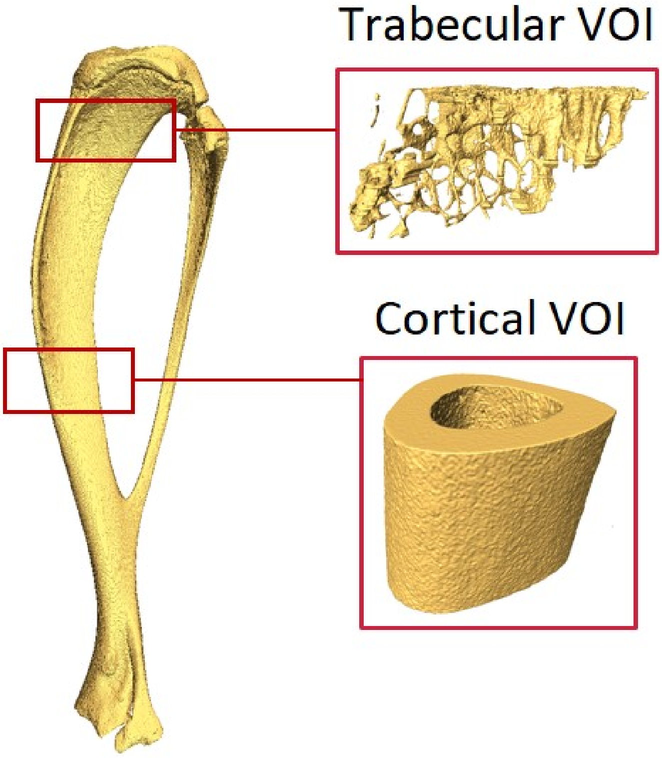

***Figure 2.1**: Volumes of interest (VOIs) for trabecular and cortical morphometric analyses on the mouse tibia.*

Morphometric parameters constitute the standard output of animal studies and have the advantage of being extensively used in literature and therefore easy to compare across different studies. On the other hand, their main limitation is that they are obtained in two defined volumes of interest in the bone, and therefore fail to comprehensively describe the whole tibia (Lu et al., 2016). Additionally, they are based on some operator-dependent procedures, such as the manual identification of the reference slices or the manual contouring of trabecular bone, and depend on the segmentation step, which may decrease their reproducibility (Christiansen, 2016).

2.2.2 Density measurements

As described previously, the attenuation coefficient associated with each voxel can be converted into a density measurement by applying a densitometric calibration equation (Bouxsein et al., 2010, Kazakia et al., 2008). Nevertheless, the presence of noise and artifacts in the image can alter the voxel-level measurements (Kazakia et al., 2008) and, therefore, the average densities over larger regions of interest are normally calculated. Average density measurements in the trabecular and cortical compartments are sometimes reported (Buie et al., 2008, Willie et al., 2013) along with the morphometric parameters described in the previous paragraph. Recently, Lu and colleagues (Lu et al., 2016) have developed a method for evaluating the spatial distribution of bone mineral content (BMC [mg]) over the tibia volume from *in vivo* microCT images. The algorithm is based on dividing the tibia into a defined number of partitions (Fig. 2.2) and calculating the BMC in each sub-volume, in order to comprehensively quantify local bone adaptation over space and time.

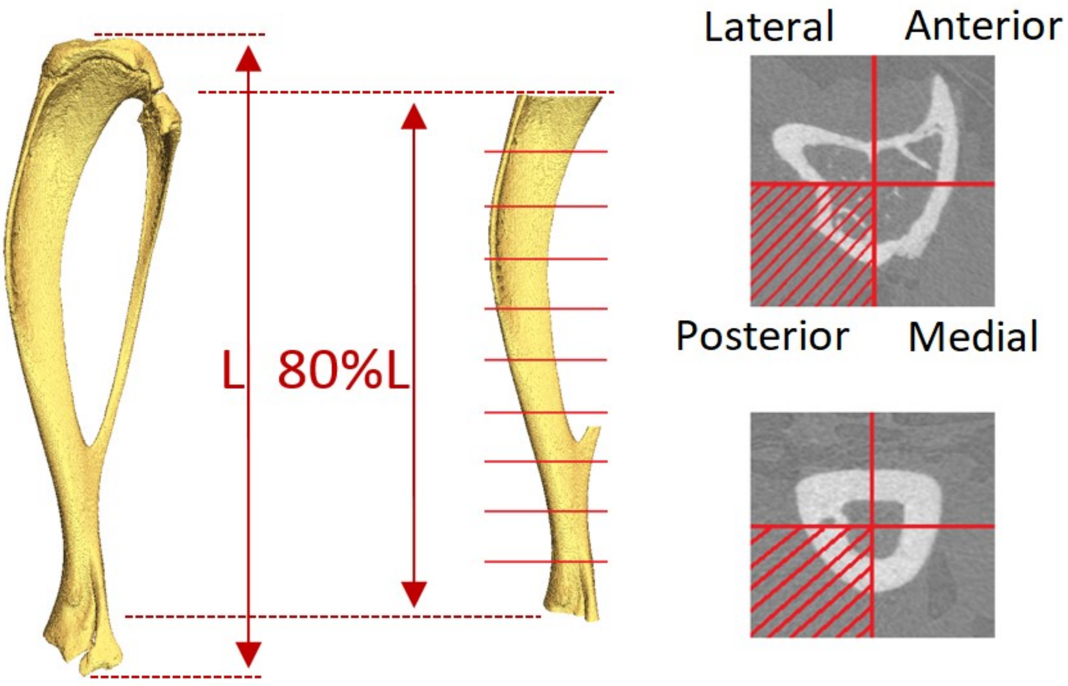

Figure 2.2: *Measurement of bone mineral content (BMC) in 40 partitions of the mouse tibia.*

By using this approach, a suitable compromise can be identified between the spatial resolution of the measurement and its reproducibility. The authors showed that by dividing the tibia into ten longitudinal sections and four quadrants (corresponding to the anterior, posterior, medial and lateral sides of the bone) local BMC measurements were highly repeatable (coefficient of variation smaller than 3.2%) (Lu et al., 2016). Dividing the tibia into smaller partitions would provide higher spatial resolution but lower measurement reproducibility. Compared to standard morphometric parameters, the repeatability of local BMC measurements was of the same order or higher (coefficients of variations in the range of 0.5% for Ct.Th to 3.6% for Tb.BV/TV, (Lu et al., 2016, Nishiyama et al., 2010)).

2.2.3 Applications of microCT imaging to study the properties of the mouse tibia

MicroCT imaging has been used in many different applications, such as the investigation of bone maturation in order to identify the different phases of bone growth (Bortel et al., 2015, Main et al., 2010) and potential differences between male and female mice (Glatt et al., 2007, Willinghamm et al., 2010). Waarsing and colleagues (2004a) proposed for the first time to use *in vivo* micro-CT scans acquired at multiple time points to assess longitudinal changes in the tibia architecture of ovariectomised (OVX) rats. Subsequently, a similar approach has been used on the mouse tibia. In mice, after 6 weeks from OVX surgery reductions of 22 – 40% in Tb.BV/TV, reduction of 12 – 43% in Tb.N and increases of 17 – 84% in Tb.Sp were observed (Klinck et al., 2008). (Buie et al., 2008) used longitudinal imaging to characterise developmental patterns in three different mouse strains, finding that trabecular changes and mineralisation patterns were similar, while structural adaptations at the diaphysis were strain-dependent. Another important application is the investigation of anabolic interventions, which include pharmaceutical treatments and mechanical loading. Parathyroid hormone (PTH) is an anabolic drug for the treatment of osteoporosis (Neer et al., 2001) and its effect has been investigated in mice of different strains (Campbell et al., 2014, Lu et al., 2017). PTH injections provoke significant increases in trabecular bone volume fraction (up to 107% after four weeks of treatment), trabecular thickness (up to 24%) and cortical thickness (13%)

(Campbell et al., 2014), and its anabolic effect is not uniform over space and time, with early changes localised at the medial and posterior regions of the proximal tibia (Lu et al., 2017). The investigation of the effect of mechanical loading on bone constitutes the most relevant application in the framework of this study, since the combination of longitudinal imaging and finite element (FE) modelling can bring significant advantages in this area. The bone response to different physical activities (e.g. running in a revolving wheel or on the treadmill) has been firstly assessed using a cross-sectional approach (Hoshi et al., 1998, Leppänen et al., 2008). Subsequently, the effect of passive loading has been assessed in order to avoid the systemic effects of exercise and to control the load magnitude applied on the bone. Different loading conditions have been applied, including four-point bending (Turner et al., 1995) and cantilever bending (Srinivasan et al., 2003). On the mouse tibia, passive compressive loading is currently the most common configuration to investigate the effect of mechanical loading, which is less invasive and more representative of the physiological scenario (Brodt and Silva, 2010, De Souza et al., 2005). Passive compression of the tibia is performed by applying a load between the flexed knee and ankle by means of a loading machine (Fig. 2.3). The loading protocol involves using a specific peak load, waveform, frequency, number of cycles and rest insertions during loading sessions, which affect the bone adaptation and can be tuned in order to optimise the achieved bone response according to the final application (Holguin et al., 2013, Weatherholt et al., 2013).

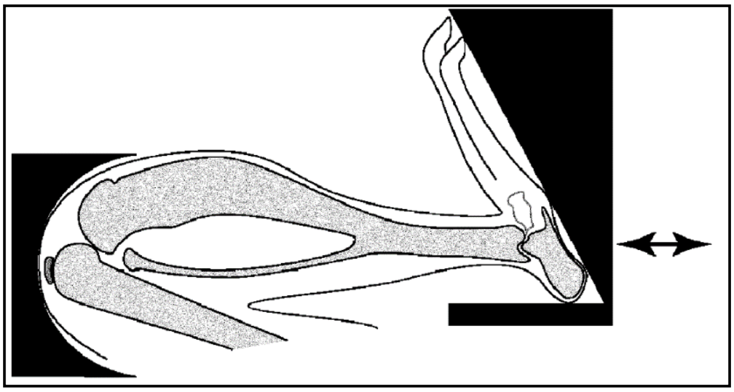

***Figure 2.3**: Schematic of loading apparatus to apply axial compression to the mouse tibia. Arrows indicate the direction of loading. Image reproduced with permission (Fritton et al., 2005).*

The anabolic effect of *in vivo* passive compression on the mouse tibia reported in literature includes increased cortical bone formation and altered trabecular organisation (Birkhold et al., 2015, De Souza et al., 2005, Holguin et al., 2013). It has also been reported that the bone response is influenced by different factors, such as age (De Souza et al., 2005) and genetics (Wallace et al., 2015). The effect of aging is of particular interest, since potential treatments for osteoporosis would target the elderly population. Therefore, it has been the focus of extensive investigation in both C57BL/6 mice (Birkhold et al., 2014a, Birkhold et al., 2014b, Razi et al., 2015, Willie et al., 2013) and in BalbC mice (Brodt and Silva, 2010, Silva et al., 2012). Most studies showed that tibial compression stimulates bone formation at all ages, but the bone response is reduced in elderly mice compared to young mice. Willie et al. (2013) reported that, after two weeks of *in vivo* loading, 10-week-old C57BL/6 mice had increased Tb.BV/TV (+117%), Tb.Th (+51%) and reduced Tb.Sp (-8%). In older mice (26 weeks) the effect of loading was reduced (+50% in Tb.BV/TV, +26% in Tb.Th). (Birkhold et al., 2014b, Holguin et al., 2014, Willie et al., 2013) reported that in 22-month-old C57BL/6 mice the effect of loading was reduced by 45 – 63% compared to 5-month-old mice. In BalbC mice, 6 weeks of *in vivo* loading provoked an increase in cortical bone volume (larger than 6%) at all analysed ages (2, 4, 7, 12 months), with the maximum response observed in 4-months-old mice (+13%).

2.2.4 Effect of radiation exposure

The key advantage of longitudinal studies is the opportunity to track detailed changes in the same bone of the same mouse over time, fundamental to evaluate small early effects of interventions on bone properties. However, the repeated exposure to ionising radiation could potentially have a negative effect on the cell activity and therefore on the tissue. Previous studies have reported different results about the effect of radiation on bone. Some found a significant positive or negative effect on some morphometric parameters measured on trabecular or cortical bone in the mouse, while no effect was observed in other cases. Klinck and colleagues (Klinck et al., 2008) analyzed the effect of repeated scans on the tibia (5 scans at 846 mGy radiation dose; 10.5 μm voxel size) in female C3H/HeJ, C57BL/6J and BALB/cByJ mice (control, ovariectomised, OVX, and sham-operated, SHAM, groups) (Table 2.1). In most mice groups analyzed in that study, a significant reduction in trabecular bone volume fraction (Tb.BV/TV) was found (-20.0% and -14.0% for C57BL/6J mice in OVX and SHAM groups, respectively). Additionally, significant increase in trabecular separation (Tb.Sp) or decrease in trabecular number (Tb.N) was observed for some of the studied groups (+9.6% in Tb.Sp for control C3H/HeJ mice, and -9.2% in Tb.N for control C57BL/6J mice). Smaller effects were found on cortical parameters, although some significant differences were found in cortical area (+5.7% for SHAM C57BL/6J mice) and in marrow area (-4.8% and -3.6% for OVX and sham C57BL/6J mice, respectively). Willie and colleagues (Willie et al., 2013) reported the effect of four scans (10.5 µm voxel size) in control female C57BL/6J mice and in mice which underwent *in vivo* cyclic compressive loading on the tibia, as well as on mice of different ages (Table 2.1). They observed a significant reduction in trabecular BV/TV (-38% and -20% for 10-week-old control and loaded groups respectively) and a significant increase in Tb.Sp (+39% and +29% for 10-week-old control and loaded groups respectively). No effect was observed in skeletally mature mice (26-week-old). On the other hand, Buie and colleagues (Buie et al., 2008) found no differences between low-radiation (6 scans over 42 weeks at 188 mGy) and high-radiation (12 scans over 42 weeks at 188 mGy) groups in female C3H/HeN, C57BL/6 and BALB/c mice, independently of the age (Table 2.1). Lastly, Laperre and colleagues (Laperre et al., 2011) found that three scans at 776 mGy radiation dose induced a reduction of 30% in trabecular BV/TV and 35% in Tb.N in 10-week-old male C57Bl/6 mice (no effect on cortical parameters) (Table 2.1). By using lower-radiation scanning protocols (434 mGy and 166 mGy) they found no significant effect on trabecular or cortical parameters in 4- and 16-week-old male C57Bl/6 mice (Table 2.1). In all cases, radiation had no significant effect on TMD, in both trabecular and cortical compartments (Table 2.1).

Reference	Mouse Strain	Age [weeks]	Gender	Group	Machine	Voxel size [µm]	Radiation dose [mGy]	Nr Scans	Parameters investigated	Comparison with	Significant differences
Buie et al, 2008	C3H/Hen	6	F	WT	VivaCT 40, Scanco Medical	19.0	188	12 (over 42 weeks)	Tb.BV.TV, Tb.Th, Tb.Sp, Tb.N, SMI, DA, Conn.D, Tb.TMD, Tb.BMD, Tt.Ar, Ct.Ar, Ct.Th, Ma.Ar, J	Group which underwent 6 scans at 188 mGy	No differences
	C57BL/6J										
	BALB/c										
Klinck et al, 2008	C57BL/6J	12	F	WT	VivaCT 40, Scanco Medical	10.5	846	5 (every week)	Tb.BV/TV, Tb.Th, Tb.Sp, Tb.N, Ct.Ar, Ct.Th, Ma.Ar	Contralateral non-irradiated leg	Tb.N (-9.2%)
		12	F	OVX							Tb.BV/TV (-20.0%), Ma.Ar (-4.8%)
		12	F	SHAM							Tb.BV/TV (-14.0%), Ct.Ar (+5.7%), Ma.Ar (-3.6%)
	C3H/HeJ	12	F	WT							Tb.BV/TV (-8.0%), Tb.Sp (+9.6%)
		12	F	OVX							Tb.BV/TV (-19.4%), Tb.Sp (+14.4%), Tb.N (-11.3%), Ma.Ar (-3.4%)
		12	F	SHAM							Tb.BV/TV (-10.5%), Tb.Sp (+14.1%), Tb.N (-11.1%)
	BALB/cByJ	12	F	WT							Tb.BV/TV (-19.7%), Tb.Sp (+20.7%), Tb.N (-15.8%)
		12	F	OVX							Tb.BV/TV (-8.9%), Tb.Th (+8.9%), Tb.Sp (+18.3%), Tb.N (-14.2%), Ct.Th (+7.4%), Ma.Ar (-5.7%)

		12	F	SHAM							Tb.Th (+3.9%), Tb.N (-9.5%), Ct.Th (+4.7%)
Laperre et al, 2011	C57Bl/6J	10	M	WT	SkyScan 1076, Bruker	9.0	776	3 (every 2 weeks)	Tb.BV/TV, Tb.Th, Tb.N, Tt.Ar, Ct.Ar, Ct.Th	Contralateral non-irradiated leg	Tb.BV/TV (-30%), Tb.N (-35%)
		4, 16	M	WT		9.0	434			Non-radiated group	No differences
		4, 16	M	WT		18.0	166			Non-radiated group	No differences
Willie et al, 2013	C57BL/6J	10	F	WT	VivaCT 40, Scanco Medical	10.5	Not reported *(55 kVp, 145 uA, 600 ms integration time, no frame averaging)*	4 (every 5 days)	Tb.BV/TV, Tb.Th, Tb.Sp, Tb.N, Tb.TMD, Tt.Ar, Ct.Ar, Ct.Ar/Tt.Ar, Ct.Th, Ct.TMD, Imax, Imin	Single radiated group	Tb.BV/TV (-38%), Tb.Sp (+39%)
		10	F	Loaded							Tb.BV/TV (-20%), Tb.Sp (+29%)
		26	F	WT, Loaded							No differences

Table 2.1. *Summary of the results found in the literature about the effect of radiation exposure on the mouse tibia. Groups: wild type (WT), ovariectomy (OVX), sham-operated (SHAM), in vivo compressive loading (Loaded). Trabecular morphometric parameters: bone volume fraction (Tb.BV/TV), thickness (Tb.Th), separation (Tb.Sp), number (Tb.N), structure model index (SMI), degree of anisotropy (DA), connectivity density (Conn.D), tissue mineral density (Tb.TMD), bone mineral density (Tb.BMD). Cortical morphometric parameters: total cross-sectional area (Tt.Ar), cortical area (Ct.Ar), area fraction (Ct.Ar/Tt.Ar), thickness (Ct.Th), marrow area (Ma.Ar), tissue mineral density (Ct.TMD), polar moment of inertia (J), maximum moment of inertia (Imax), minimum moment of inertia (Imin).*

The reported results suggest that the effect of ionising radiation can be reduced by tuning the scanning protocol and regime. Different parameters, such as radiation dose, number of scans, frequency of the scans and size of the scanned volume (selected regions of interest vs whole tibia) play a role in the overall effect of radiation. These parameters can be adjusted according to the final application in order to find the best compromise between achieving the required image quality and minimising the animal exposure to radiation.

2.3 MECHANICAL PROPERTIES OF THE MOUSE TIBIA

Structural mechanical properties of bone can be assessed through experimental mechanical tests. In particular, evaluating bone stiffness and strength is relevant to assess the potential effects of interventions on the mechanical competence of the bone. Most commonly, mouse tibiae are tested in three-point bending configuration (Brodt et al., 2009, Hiltunen et al., 1993, Jämsä et al., 1998, Schriefer et al., 2005, Silva et al., 2005, Stadelmann et al., 2011), which is performed by positioning the extremities of the tibia on two supports and applying a load at the midshaft. However, this approach is affected by experimental artifacts, mainly due to the fact that the aspect ratio of the tibia is not sufficient and its cross-section in not constant along the longitudinal direction (Wallace et al., 2014). Additionally, three-point bending does not replicate the physiological loading direction, which is instead better reproduced by longitudinal compression (Fig. 2.4) (Holguin et al., 2013). In fact, three-point bending tests on tibiae from C57BL/6 mice (five months of age) underestimated the bone strength (10 - 12 N (Schriefer et al., 2005, Stadelmann et al., 2011)) compared to that measured in compression (24.5 ± 2.8 N in five-month-old mice, (Holguin et al., 2013)).

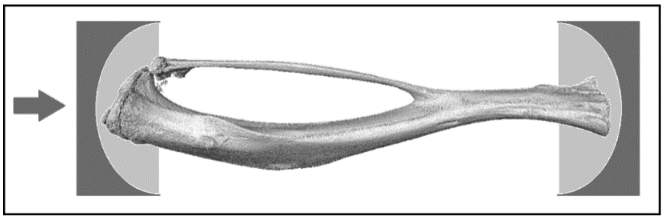

Figure 2.4*: Schematic of compression test of the mouse tibia.*

(Holguin et al., 2013) showed that after 6 weeks of *in vivo* passive compression, the tibia strength measured by mechanical testing was increased by 18% in both C57BL/6 and BalbC mice. The main limitation of mechanical testing for measuring bone strength is that it is a destructive method and can only be performed at the end of the study after sacrificing the animals. In longitudinal studies, mechanical testing could potentially be replaced by microFE predictions based on *in vivo* microCT data. Nevertheless, before application microFE model predictions have to be validated against experimental data acquired through mechanical testing.

2.4 FINITE ELEMENT MODELS OF THE MOUSE TIBIA

Micro-Finite Element (microFE) models based on *in vivo* microCT images can potentially be used for investigating mechanical properties of bone in longitudinal studies. If properly validated, they could provide non-invasive measurements of structural mechanical properties and strain distributions under loading which cannot be measured *in vivo*. In literature, microFE models of the mouse tibia have been mainly used in the framework of investigating the bone response to *in vivo* passive compression (Birkhold et al., 2014a, Moustafa et al., 2012, Patel et al., 2014, Stadelmann et al., 2009, Willie et al., 2013, Yang et al., 2014). Strain distributions under loading have been estimated and compared with the measured local bone apposition and resorption (Birkhold et al., 2016), thus evaluating the mechano-responsiveness of the endocortical and periosteal surfaces. MicroFE models also provided better insight in the effect of aging on bone responsiveness. It has been reported that average strains induced by the same external load in cortical and trabecular bone were lower in elderly mice (26-week-old) compared to young mice (10-week-old) (-18% and -32% respectively), suggesting that reduced responsiveness to mechanical loading could be due to a lack of the mechanical stimulus required for initiating a response (Razi et al., 2015, Willie et al., 2013).

Different approaches have been used to develop FE models from microCT images of the mouse tibia. The simplest and most efficient approach is to use the procedure originally developed for trabecular bone (van Rietbergen et al., 1995), by converting each bony voxel into a hexahedral element with isotropic linear elastic material properties (Moustafa et al., 2012, Patel et al., 2014). More complex approaches aimed at refining either the representation of the bone geometry or the heterogeneity of the tissue. Tetrahedral models have been used to better recover the smooth bone boundaries (Yang et al., 2014). Heterogeneous material properties based on microCT measurements of local density have also been implemented. (Yang et al., 2014) converted the local density (ρ) into Young's modulus (E) by applying the following power law (Easley et al., 2010), which was obtained by fitting experimental data from bones of different species and anatomical locations:

$$E = 1.127 \cdot 10^{-4} \rho^{1.746} \tag{2.1}$$

In (Razi et al., 2015) the tibia was divided into twenty longitudinal sections with different material properties. The region of interest (ROI) with the highest average attenuation coefficient (μ) was assigned the maximum Young's modulus (E), assumed to be equal to 17 GPa. The other sections were assigned E based on their average μ by assuming that:

$$\mathrm{E_{ROIa}/E_{ROIb}} = (\mu_{\mathrm{ROIa}}/\mu_{\mathrm{ROIb}})^{1.5} \tag{2.2}$$

where a and b represent two different ROIs. Lastly, Pereira et al. (2015) implemented poroelastic material properties in order to investigate the role of interstitial fluid velocity as the mechanical stimulus triggering bone adaptation in axial loading.

Other important aspects in the development of FE models of the tibia are the inclusion of the fibula and the implementation of the boundary conditions, since they induce significant variations in the predicted strains (Razi et al., 2014, Yang et al., 2014). The inclusion of the fibula could potentially better represent the physiological loading conditions (Yang et al., 2014). However, modelling the proximal tibio-fibular junction and growth plate is not trivial. The non-mineralised tissue connecting the fibula to the tibia is not visible in the microCT images, therefore its geometry and material properties are based on assumptions. The implementation of the boundary conditions also has great influence on the results. Razi and colleagues (2014) reported that by varying the size of the surfaces where boundary conditions are applied (both at the knee and ankle side), average principal strains at the midshaft varied up to 10%, while local strains varied up to 70%. Additionally, by varying the proximal and distal constraints (e.g. fixing all degrees of freedom vs allowing rotational moments), variations in predicted local strains were up to 150%. Lastly, variations in bone alignment (rotation of the longitudinal axis of the tibia in the range of 20°) provoked variations in local strains up to 60%. These results highlight the importance of performing a comprehensive validation of the microFE predictions at the local level, and in particular of accurately reproducing in the model the realistic boundary conditions applied during the experimental test.

2.4.1 Validation of microFE models of the mouse tibia

As mentioned before, microFE models of the mouse tibia have been mainly used to evaluate the spatial distribution of strains under loading (Birkhold et al., 2014a, Moustafa et al., 2012, Patel et al., 2014, Stadelmann et al., 2009, Willie et al., 2013, Yang et al., 2014). Therefore, it is fundamental to perform an accurate validation of the model predictions at the local level. Validation is performed by comparing the model predictions to adequate experimental measurements (Anderson et al., 2007), which can be structural mechanical properties or local properties, e.g. displacements and strains. Local experimental measurements are normally more challenging to obtain but constitute a more robust validation, since the same apparent mechanical behaviour can be obtained from infinite different configurations of local properties.

In most cases, FE models of the tibia have been validated or calibrated against strain gauge measurements (Fig. 2.5) (Birkhold et al., 2014b, Patel et al., 2014, Stadelmann et al., 2009, Willie et al., 2013, Yang et al., 2014). The reported differences between measured strains and those predicted by FE models at the strain gauge location vary in the range of 1 – 43%.

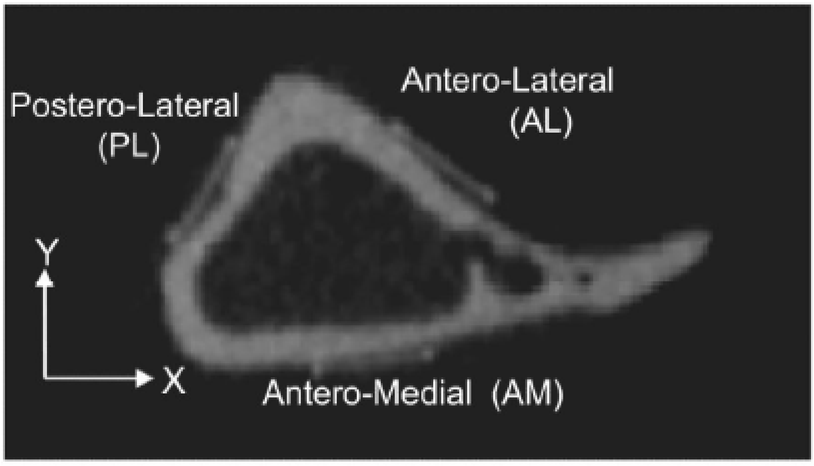

***Figure 2.5**: Grayscale microCT slice showing locations of the three strain gauges in the transverse cross-section of the tibia. Image reproduced with permission from (Patel et al. 2014).*

There are many limitations associated with this approach for a small bone like the mouse tibia. First of all, only one or a few measurements can be obtained for each bone. In Stadelmann et al. (2009) three strain gauges were attached at three different longitudinal locations, while in (Patel et al., 2014) three strain gauges were attached at the same longitudinal level in order to estimate the strain field at the selected cross-section (Fig. 2.5). Still, this method cannot fully capture the heterogeneity of the strain distribution. Additionally, the presence of the sensor itself likely influences the measurement by provoking a local stiffening of the bone. In the mouse forearm, strain gauge measurements were 37 – 56% lower than FE predictions, while Digital Image Correlation (DIC) measurements were in better agreement with numerical results (3 – 14% difference), suggesting that strain gauges tend to underestimate local strains (Begonia et al., 2017). Lastly, strain gauges measure the average strain over a relatively large area (typical size of the active gauge = 0.38 mm x 0.50 mm).

In order to overcome these limitations, the Digital Image Correlation (DIC) technique has been used to measure the displacement field over the tibia surface (Sztefek et al., 2010) and to validate FE models (Fig. 2.6) (Pereira et al., 2015). In DIC, the surface of the sample is speckled and observed by charge-coupled device (CCD) cameras during loading (Grassi and Isaksson, 2015). The speckles position is tracked over time in order to measure local displacements, which can also be differentiated to obtain local strains. Qualitatively, the strain patterns measured with DIC and predicted with FE models were in good agreement, even if local differences were observed (Pereira et al., 2015). A limitation of this technique is that the measured displacements are affected by different factors, e.g. speckle size and density, position of the cameras, lighting of the sample surface. Therefore, accurate sensitivity analyses are required in order to optimise the experimental setup (Carriero et al., 2014). Moreover, DIC can only provide surface measurements, while displacements in the internal bone volume remain unknown.

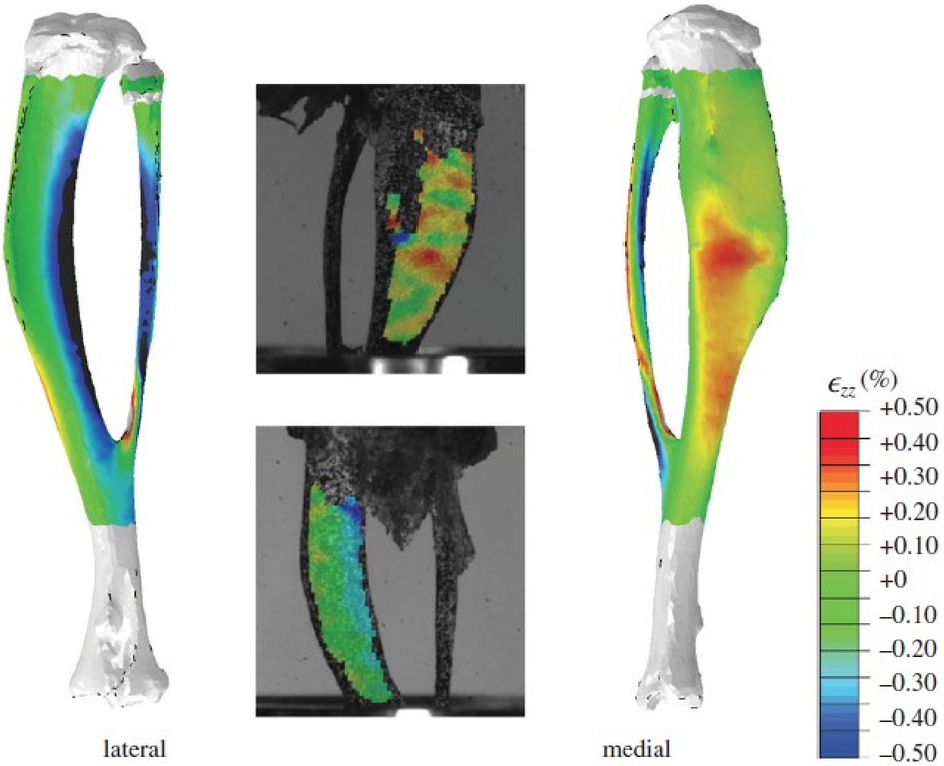

Figure 2.6: *Contour plots of the longitudinal strains e $_{zz}$ calculated in the FE models and DIC measurements in eight-week-old mice of the same strain and gender by Sztefek et al. 2010. FEA used the geometry of a non-adapted tibia under an axial peak load of 12 N. (DIC images adapted from Sztefek et al. 2010 with permission from Elsevier.). Image reproduced from (Pereira et al., 2015).*

A possible approach to overcome these limitation is Digital Volume Correlation (DVC, Paragraph 1.4.5), which can provide volumetric measurements of local displacements (Grassi and Isaksson, 2015). DVC has been applied to bone samples from different species, including human and bovine trabecular bone samples (Chen et al., 2017, Gillard et al., 2014, Zauel et al., 2005), human vertebra (Hussein et al., 2012), porcine vertebra (Costa et al., 2017), but to the author's knowledge has never been applied to the mouse tibia.

CHAPTER 3

OPTIMIZATION OF SCANNING PROCEDURE FOR *IN VIVO* MICRO-CT IMAGING OF THE MOUSE TIBIA

Part of this chapter has been originally published in Oliviero, S., Lu, Y., Viceconti, M. & Dall'Ara, E. 2017. Effect of integration time on the morphometric, densitometric and mechanical properties of the mouse tibia. *Journal of Biomechanics,* 65**,** 203-211.

DOI: http://dx.doi.org/10.1016/j.jbiomech.2017.10.026

SUMMARY

Animal models are important for studying bone remodeling and testing the effect of bone interventions. In longitudinal studies, Micro-Computed Tomography (microCT) images can be used to monitor bone changes over time, by measuring morphometric and densitometric properties of the bone, as well as to develop finite element (FE) models to estimate mechanical properties. However, there are concerns about the effect of the X-ray radiation induced by the repeated scans on the same animal. Therefore, it is crucial to find the best compromise between radiation dose and accuracy in the estimation of bone parameters. In this study, the effect of microCT integration time (IT, time the bone is exposed to radiation at each rotation step during the microCT scan) on measurements performed on the mouse tibia has been investigated. Four mouse tibiae were scanned at 10.4 µm voxel size using four different scanning procedures, characterized by decreasing integration time (from 200 ms to 50 ms) and therefore decreasing nominal radiation dose (from 513 mGy to 128 mGy). From each image the following measurements were obtained: trabecular and cortical morphometric parameters, spatial distribution of bone mineral content (BMC) in the whole tibia, FE-based estimations of stiffness and strength. A high-resolution scan (4.3 µm voxel size) was used to quantify the measurement's accuracy obtained for each scanning procedure. Integration time had the largest effect on trabecular morphometric parameters (7-28%) while lower effect was observed on cortical parameters (1-3%), BMC in 40 sub-regions of the tibia (1-10%) and mechanical properties estimated from microFE models (1-3%). In conclusion, the effect of integration time on image-based measurements has been quantified. This data has been used to define the *in vivo* scanning protocol for the subsequent analyses (IT100, IT = 100 ms).

3.1 INTRODUCTION

Animal testing on small rodents has been used to investigate bone remodeling and to study the effect of bone interventions. Micro-Computed Tomography (microCT) imaging is considered the gold standard for bone imaging and guidelines have been published regarding the image acquisition and data analysis of bone parameters *ex vivo* or *in vivo* (Bouxsein et al., 2010). *In vivo* microCT imaging can be used in longitudinal studies to observe bone changes on the same animal with respect of baseline, thus reducing the inter-subject variability (Campbell and Sophocleous, 2014). Standard analyses of bone changes in the tibia are performed in two volumes of interest (VOIs): a VOI located below the proximal growth plate for trabecular bone analyses and a VOI centered at the midshaft for cortical bone analyses (Bouxsein et al., 2010). While it is known that local tissue mineral density (TMD) (Tassani et al., 2011) measurements at the voxel level are affected by microCT artifacts (Kazakia et al., 2008), TMD can be measured over a larger VOI in order to measure potential changes in the tissue mineralization (Bouxsein et al., 2010). Lu and colleagues (Lu et al., 2017) recently proposed a method based on *in vivo* microCT imaging, image registration and automatic image processing to analyze the spatio-temporal distribution of densitometric properties, e.g. bone mineral content (BMC), in the whole tibia. This method is associated with a better repeatability than standard morphometric parameters (Lu et al 2016) and provides comprehensive measurements over the whole bone, which has been used to evaluate early effects of parathyroid hormone (PTH) (Lu et al., 2017). Furthermore, *in vivo* microCT images can be converted into micro-Finite Element (microFE) models (Patel et al., 2014, van Rietbergen et al., 1995) for the non-invasive estimation of mechanical properties over time.

While longitudinal microCT imaging can be combined with other *in vivo* imaging modalities to study co-morbidities (Dall'Ara et al., 2016), there are concerns about its invasiveness due to the X-rays ionising radiation induced by the repeated scans on the same animal. Therefore, for the different applications, an acceptable compromise between radiation dose and image quality should be found. In general, image quality improves by decreasing the voxel size (Christiansen, 2016), increasing the number of projection and/or the frame averaging and/or the integration time (Campbell and Sophocleous, 2014). However, in all cases the increase in the image signal-to-noise ratio is achieved by a longer scanning time and consequently an increased radiation exposure.

The effect of *in vivo* imaging has been reported in previous studies (Paragraph 2.2.4), which are summarized here. (Klinck et al., 2008) reported the effect of five weekly scans at 846 mGy radiation dose in mice of three different strains and three different groups (wild type WT, OVX and sham-operated, N = 6-8/group). They found that radiation induced reductions in Tb.BV/TV (8-20%), which were significant for most analysed groups (although not significant for C57BL/6J-WT mice, Table 2.1). Tb.Sp significantly increased in the BalbC groups (14-20%) and showed a non-significant increase in the C57BL/6J groups. In some cases, cortical parameters also showed small but significant variations (Table 2.1). Similar effects were reported by (Willie et al., 2013), who observed significant decreases in Tb.BV/TV (20-38%) and significant increases in Tb.Sp (29-39%, Table 2.1) in young mice (10 weeks old) of two different groups (WT and mice which underwent *in vivo* compressive loading, N = 4/group) after five scans (every five days; 55 kVp, 145 µA, 600 ms integration time, no frame averaging, radiation dose not reported). No significant effect was found in older mice (26 weeks old). Lastly, (Laperre et al., 2011) found that three scans (every two weeks) at 776 mGy induced significant reductions in Tb.BV/TV and Tb.N, while the effects were not significant at 434 mGy radiation dose (N = 4/group).

An effective strategy for obtaining low-radiation protocols could be to reduce the integration time (time the bone is exposed to radiation at each rotation step), since it is proportional to the nominal radiation dose. It has been shown that variations in integration time do not affect the calibration curve for converting the X-ray attenuation coefficients into equivalent bone mineral density for different calibration phantoms (Nazarian et al., 2008). However, little is known about how the change in image quality due to the integration time would affect the microCT-based measurements performed on the mouse tibia.

The goal of this study was to investigate the effect of integration time on the measurement of mouse tibia morphometric, densitometric and mechanical properties estimated with protocols that can be applied *in vivo*. Quantifying measurements errors is an essential step for selecting a suitable scanning protocol providing the best compromise between radiation dose and measurement accuracy.

3.2 MATERIALS AND METHODS

3.2.1 Sample Preparation

Four tibiae (two right and two left) were explanted from 22-weeks-old C57BL/6J female mice used in a previous study (Lu et al., 2015). One of the mice underwent ovariectomy (OVX) and the other one was sham-operated (SHAM) at week 14 of age. Right tibiae underwent seven *in vivo* scans (Lu et al., 2017), while left tibiae were not irradiated. After carefully removing the soft tissues with a scalpel, the specimens were dehydrated in air at room temperature for 24 hours and embedded in acrylic resin (Epofix, Struers, Denmark) (Fig. 3.1), which has a water equivalent attenuation coefficient. The specimens are referred to as OLT (OVX, left tibia), ORT (OVX, right tibia), SLT (SHAM, left tibia) and SRT (SHAM, right tibia).

***Figure 3.1**. Mouse tibia embedded in acrylic resin.*

3.2.2 Scanning Procedures and Reconstructions

Each specimen was scanned using four different scanning procedures (IT200, IT150, IT100 and IT50), suitable for *in vivo* application (VivaCT 80, Scanco Medical, Bruettisellen, Switzerland; energy 55 kVp, current 145 µA, voxel size 10.4 µm, field of view 32 mm, 750 projections/180°, no frame averaging, 0.5 mm Al filter). Integration time was adapted for each protocol from 200 ms for IT200 to 50 ms for IT50. The IT200 protocol has been previously used for scanning the mouse tibia *in vivo* (Lu et al., 2016, Lu et al., 2017) and is associated with 513 mGy nominal radiation dose, which is comparable to that reported previously (Laperre et al., 2011) as acceptable for three *in vivo* scans. The other three scanning protocols (IT150, IT100 and IT50) were associated to a reduced nominal radiation dose (384 mGy, 256 mGy and 128 mGy, respectively), as computed from the data provided by the manufacturer. The total time to scan the whole tibia using each procedure was 38, 31, 25 and 19 minutes, respectively. All images were reconstructed using the software provided by the manufacturer (Scanco Medical AG) and applying a beam hardening correction based on a phantom of 1200 mg HA/cc density, which has been shown to improve the local tissue mineralization measurement (Kazakia et al. 2008). Additionally, each specimen was scanned at higher resolution by using an *ex vivo* microCT scanner and a previously optimized scanning protocol (SkyScan 1172, Bruker, Belgium; 4.3 μm voxel size, voltage 49 kV, current 179 μA, exposure time 1180 ms, 180° rotation, 0.7° rotation step, frame averaging x2, 0.5 mm Al filer) (Dudek et al., 2016, Mohanty et al., 2010). These images were used as gold standard to quantify the measurements errors obtained from the other scanning procedures. Reconstruction was performed by using the software provided by the manufacturer (NRecon, Bruker; ring artefacts reduction factor 10, dynamic range 0 – 0.13) (Dudek et al., 2016, Mohanty et al., 2010). The same scanning and reconstruction protocols were used for imaging a four-insertion solid densitometric calibration phantom for microCT (MicroCT-HA, QRM, Germany).

3.2.3 Image preprocessing

From each image three analyses were carried out (Fig. 3.2): standard morphometric analysis, spatial distribution of BMC and estimation of the mechanical properties with microFE models.

In order to align all images in the same reference system, a rigid registration procedure was applied. One of the images was rotated in Amira (Amira 6.0.0, FEI Visualization Sciences Group, France) in order to approximately align its longitudinal axis to the *Z*-axis of a global reference system. Then, the other images were rigidly registered to the aligned one. Normalized Mutual Information was used as optimization criterion, which was used in similar studies (Birkhold et al., 2014a). Right tibiae were horizontally flipped to perform the registration to the reference (left) tibia. After alignment, images were resampled using Lanczos interpolator, which is associated to low interpolation errors (Meijering, 2000) and has been used in similar studies (Birkhold et al., 2014a). Afterwards, a Gaussian filter (kernel 3x3x3, standard deviation 0.65) was applied to reduce the high frequency noise (Bouxsein et al., 2010).

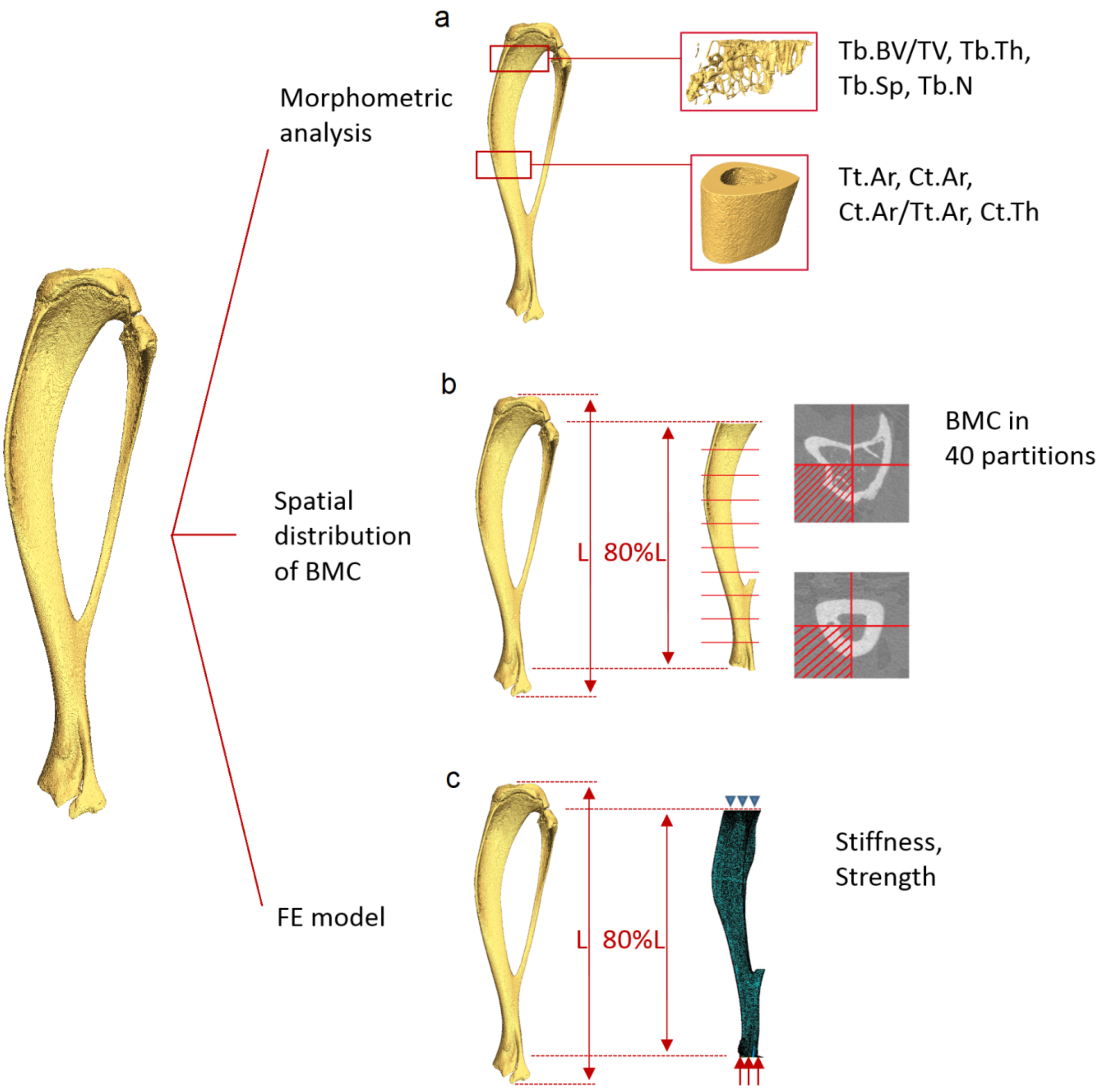

***Figure 3.2**. Analyses performed on each microCT image of the mouse tibia. (a) Standard morphometric analysis of trabecular and cortical volumes of interest (VOIs) following the guidelines reported in (Bouxsein et al., 2010). Trabecular parameters: bone volume fraction (Tb.BV/TV), thickness (Tb.Th), separation (Tb.Sp) and number (Tb.N). Cortical parameters: total cross-sectional area (Tt.Ar), cortical area (Ct.Ar), area fraction (Ct.Ar/Tt.Ar), thickness (Ct.Th). (b) Spatial distribution of Bone Mineral Content (BMC). VOI consisted in the middle 80% of the tibia length (L) after removal of the fibula (Lu et al., 2016). The VOI was then divided in 10 equally spaced sections, which were further divided into four quadrants. (c) Finite Element (FE) models for estimation of stiffness and strength in uniaxial compression (Lu et al., 2017).*

3.2.4 Standard Morphometric Analysis

Morphometric analyses were performed using CTAn (Bruker, Belgium). For trabecular measurements, a reference slice was selected in the proximal growth plate, identified as the slice where the medial and lateral sides of the growth plate merged. An offset of 0.2 mm was used to identify the starting point of the VOI in the longitudinal direction. The height of the VOI was 1 mm (Lu et al., 2016). Trabecular bone was contoured by manually drawing 2D regions of interest (ROIs) every 5 slices (Fig. 3.3) and the contours merged with the dynamic interpolation algorithm included in the software package. Segmentation was performed using a single level threshold (Fig. 3.3), calculated for each image as the average of the grey levels corresponding to the bone and background peaks in the image histogram (Chen et al., 2017, Christiansen, 2016). A despeckling filter was applied to remove 3D white (bone) regions less than 10 voxels in volume, which are likely to be non-filtered noise in the image. Trabecular bone volume fraction (Tb.BV/TV), thickness (Tb.Th), separation (Tb.Sp) and number (Tb.N) were computed for each VOI (Bouxsein et al., 2010).

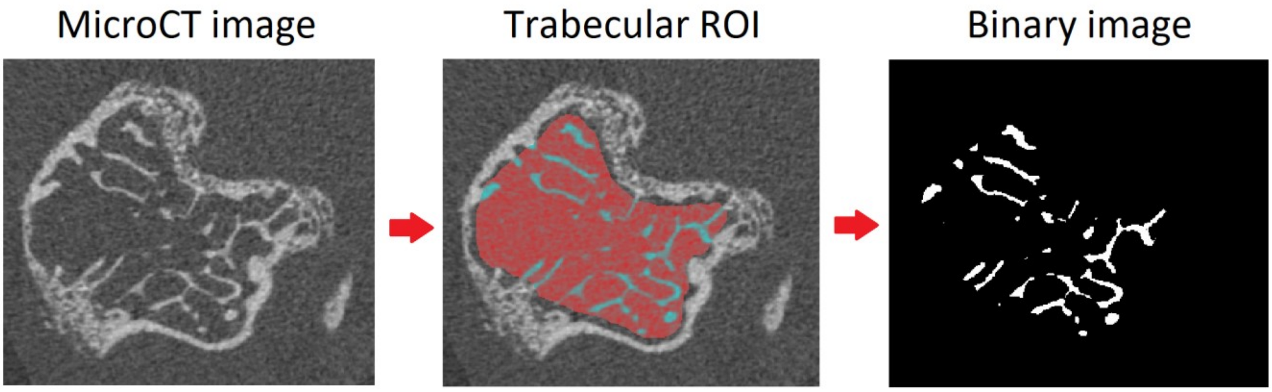

Figure 3.3. *Example of a microCT cross-section of trabecular bone. 2D regions of interest (ROIs) were drawn manually in order to contour trabecular bone. Segmentation was performed using a global threshold.*

For cortical analysis, a VOI of 1 mm was selected, centered at the tibial midshaft. After segmentation, pores within the cortex were removed by applying a closing function (2D round kernel, radius equal to 10 pixels). Total cross-sectional area (Tt.Ar), cortical bone area (Ct.Ar), cortical area fraction (Ct.Ar/Tt.Ar) and cortical thickness (Ct.Th) were computed for each VOI (Bouxsein et al., 2010).

3.2.5 Sensitivity analysis on the threshold value

The effect of the threshold value on the measurement of trabecular morphometric parameters was evaluated, since they were more influenced by the segmentation procedure compared to the other measurements, as reported later. Trabecular analysis was performed on the same VOIs as reported above by applying a similar procedure (single level threshold followed by despeckling filter). Four threshold values were tested from 400 mgHA/cc to 700 mgHA/cc in steps of 100 mgHA/cc, which were in the range of those reported in the literature (from approximately 420 mg HA/cc (Klinck et al., 2008) to 813 mg HA/cc (Birkhold et al., 2014a)). Trabecular bone volume fraction (Tb.BV/TV), thickness (Tb.Th), separation (Tb.Sp) and number (Tb.N) were computed for each VOI (Bouxsein et al., 2010).

3.2.6 Spatial Distribution of BMC and TMD

The co-registered grey-values (GV) images (after the image processing described in 3.2.3) were converted into tissue mineral density (TMD) images by using the procedure suggested by the manufacturer of the *in vivo* scanner, which is based on weekly quality checks performed on a densitometric phantom with five insertions of known equivalent density (800, 400, 200, 100 and 0 mg HA/cc).

The GV of the reference high-resolution images obtained with the *ex vivo* scanner were converted into TMD scale by using the grey levels associated with the five insertions of the scanned densitometric phantom (1200, 800, 200, 50 and 0 mgHA/cc). The following linear regression (coefficient of determination $R^2 = 0.998$) equation was found by using the mean grey-values within each region (160 ± 24; 118 ± 29; 47 ± 28; 26 ± 18; 19 ± 12) and the physical known densities of the insertions:

$$\text{TMD [mg HA/cc]} = 8.471\ \text{GV} - 175.611 \tag{3.1}$$

BMC in each voxel was then calculated as its TMD multiplied by the volume of the voxel. The spatial distribution of BMC within the tibia was calculated by applying a similar procedure to that reported in (Lu et al., 2016), which is briefly explained here. The length of the tibia was measured and a VOI was defined by excluding the proximal and distal extremities (by 10% of the total length). The fibula was also removed from the VOI (Fig. 3.2b). To make sure that the fibula was cut at the same level in each image, a connectivity filter (connectivity rule = 6, bwlabeln function in Matlab) was applied on the 2D cross-sections in the proximity of the tibio-fibular junction. The VOI was divided into ten longitudinal sections with same thickness and each section was divided into four quadrants. Quadrants were defined by two perpendicular lines passing through the center of mass of each slice (Fig. 3.2b). Therefore, each tibia was divided into 40 partitions. For each partition, BMC was calculated as the sum of BMC in each bony voxel. TMD was calculated as TMD = BMC/BV (Tassani et al., 2011) for each partition.

3.2.7 Micro-Finite Element Models

Micro-Finite Element (microFE) models were generated for the same VOI used for BMC analysis (middle 80% of total length, excluding the fibula, Fig. 3.2c). Segmentation was performed using a single level threshold (average of the grey levels corresponding to the bone and background peaks in the image histogram), as described previously. A connectivity filter was applied to the segmented images in order to remove unconnected voxels from the VOI (connectivity rule = 6, bwlabeln function in Matlab). A Cartesian mesh was obtained by converting each bone voxel into an 8-noded hexahedral element (Chen et al., 2017, Patel et al., 2014) with isotropic linear elastic material properties. Young’s Modulus of 14.8 GPa and Poisson’s ratio of 0.3 were assigned (Webster et al., 2008).

In order to evaluate the stiffness of the bone, uniaxial compression simulations were run in displacement control (ANSYS Academic Research, Release 15.0). The proximal end of the tibia was fully constrained, while a displacement equal to 1 mm was applied on each node of the distal surface along the longitudinal direction. The apparent stiffness was calculated as the sum of reaction forces at the proximal surface, divided by the applied displacement.

For strength estimation, uniaxial compression simulations were run in force control (ANSYS Academic Research, Release 15.0). The nodes belonging to the proximal surface of the tibia were fully constrained, while 1 N load was applied on the distal surface, equally distributed on each node. It was assumed that tibia fails when 2% of the nodes reach a critical strain level (adapted from (Pistoia et al., 2002)), which was asymmetric for compression (-10300 με) or tension (8000 με) (Bayraktar et al., 2004).

3.2.8 Influence of trabecular bone on the structural mechanical properties

The influence of trabecular bone on the structural mechanical properties of the tibia was evaluated by generating microFE models including or excluding the trabecular region. The images acquired with IT200 scanning procedure (integration time equal to 200 ms) were used for this analysis. In order to exclude the trabecular bone from the image, the same mask created for trabecular morphometric analysis (CTAn, Bruker, Belgium) was applied. Segmentation was performed by using the same threshold applied for the model including the trabecular bone. Stiffness and strength were estimated in the two conditions by using the same procedure described in Paragraph 3.2.7.

3.3 RESULTS

3.3.1 Images and frequency plots

In Fig. 3.4, examples of microCT cross-sections are reported for each scanning procedure.

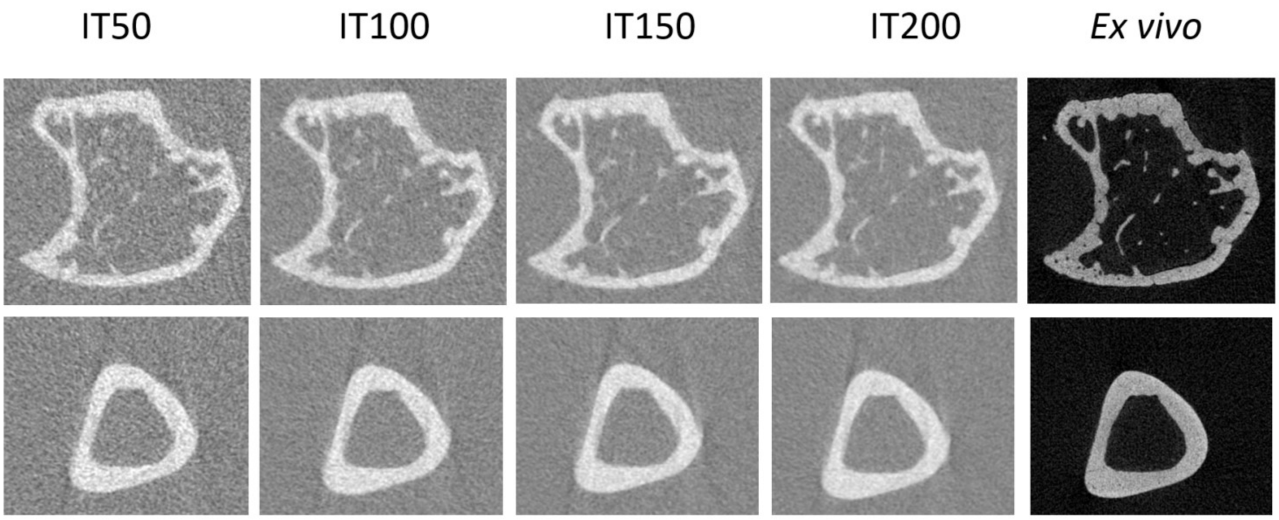

***Figure 3.4**. MicroCT cross-sections of the trabecular (top row) and cortical (bottom row) regions of the tibia (SLT sample) scanned using the four in vivo (IT50 = 50 ms, IT100 = 100 ms, IT150 = 150 ms, IT200 = 200 ms integration time) and the ex vivo scanning procedures.*

In Fig. 3.5 examples of histograms (frequency plot) are shown for the *in vivo* (Fig. 3.5a) and *ex vivo* (Fig. 3.5b) scanning procedures. When integration time was maximum (equal to 200 ms, IT200 procedure) the bone and background peaks were sharper, while with decreased integration time, higher variability was found in the grey values, indicating that the image was affected by higher noise.

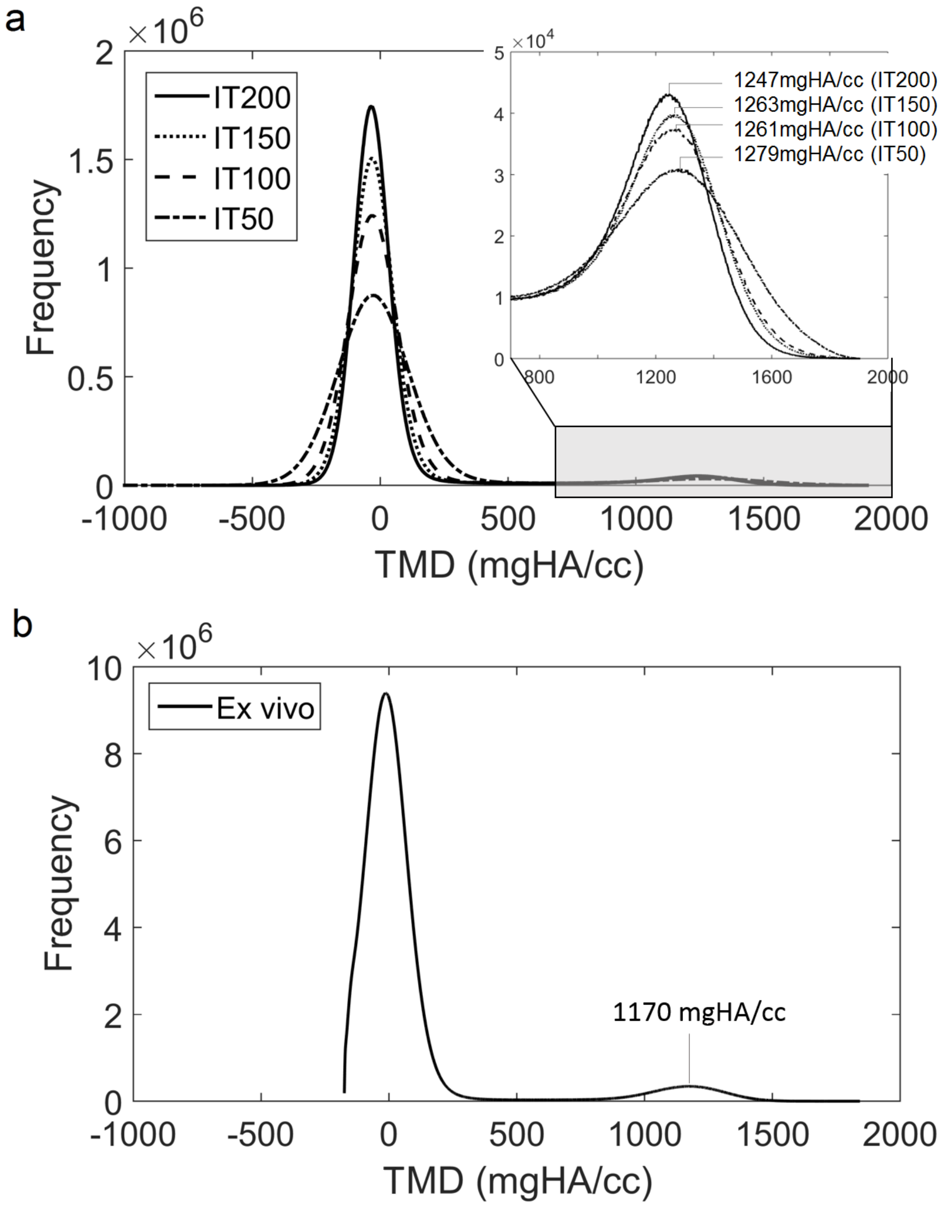

Figure 3.5. *Histograms (frequency plots) from microCT images obtained using the four in vivo (a) and the ex vivo (b) scanning procedures (OLT sample). IT200, IT150, IT100 and IT50 refer to scanning protocols with 200, 150, 100 and 50 ms integration time, respectively.*

3.3.2 Morphometric Analysis

The absolute percentage errors (median ± SD) of the trabecular morphometric parameters measured with the *in vivo* scanning protocols compared to those obtained from high-resolution images are reported in Fig. 3.6a. For all parameters a converging trend was observed, meaning that the errors tend to stabilize with increasing integration time. However, errors tended to increase with increasing integration time, while the opposite trend was expected. This was probably attributed to the presence of a systematic error, as discussed later. For Tb.BV/TV errors were 2-11% for the IT50 scanning procedure, 2-12% for IT100, 1-11% for IT150 and 1-15% for IT200. For Tb.Th errors of 10-21% were found for IT50, 19-33% for IT100, 21-36% for IT150, 22-32% for IT200. For Tb.Sp errors ranged from 19-28% for IT50, 13-27% for IT100, 18-37% for IT150, to 19-31% for IT200. Lastly, the greatest effect of integration time for found for Tb.N, for which errors of 1-13% for IT50, 15-29% for IT100, 20-30% for IT150, 20-32% for IT200 were found.

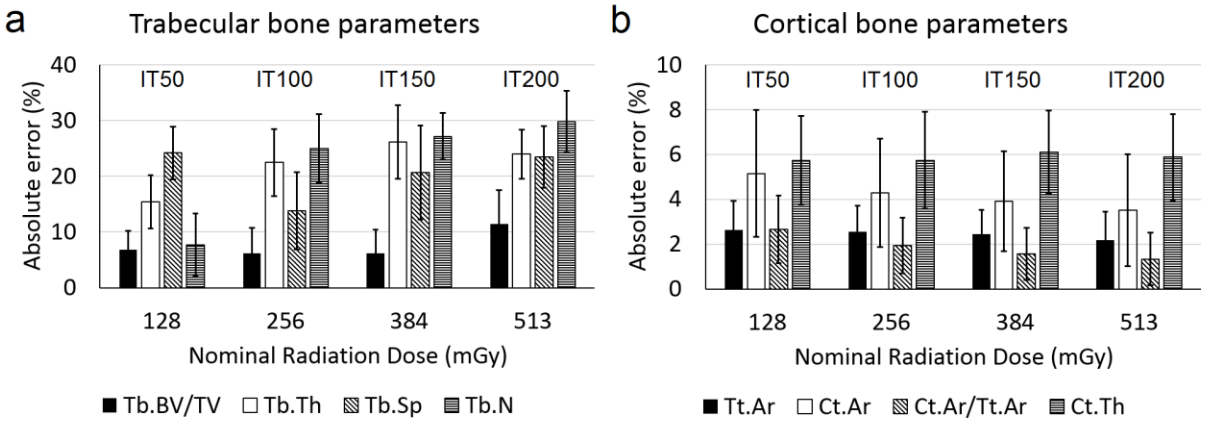

Figure 3.6. *Effect of scanning procedure on trabecular (a) and cortical (b) morphometric parameters. Absolute errors are reported as median ± SD. IT50, IT100, IT150 and IT200 refer to scanning protocols with 50, 100, 150 and 200 ms integration time respectively, associated with a nominal radiation dose of 128, 256, 384 and 513 mGy respectively. Trabecular parameters: bone volume fraction (Tb.BV/TV), thickness (Tb.Th), separation (Tb.Sp) and number (Tb.N). Cortical parameters: total cross-sectional area (Tt.Ar), cortical area (Ct.Ar), area fraction (Ct.Ar/Tt.Ar), thickness (Ct.Th).*

Errors associated to cortical parameters tended to decrease or be similar with increasing integration time (Fig. 3.6b). The largest effect of integration time was on Ct.Ar (from 5-11% for IT50, to 3-8% for IT200), while minor effects were observed on Tt.Ar (from 2-5% for IT50, to 1-4% for IT200), Ct.Ar/Tt.Ar (from 2-6% for IT50, to 1-4% for IT200) and Ct.Th (4-9% for all procedures).

3.3.3 Sensitivity analysis on threshold value

The errors in trabecular parameters obtained for each threshold value with respect to the values obtained from the high-resolution images are reported in Fig. 3.7.

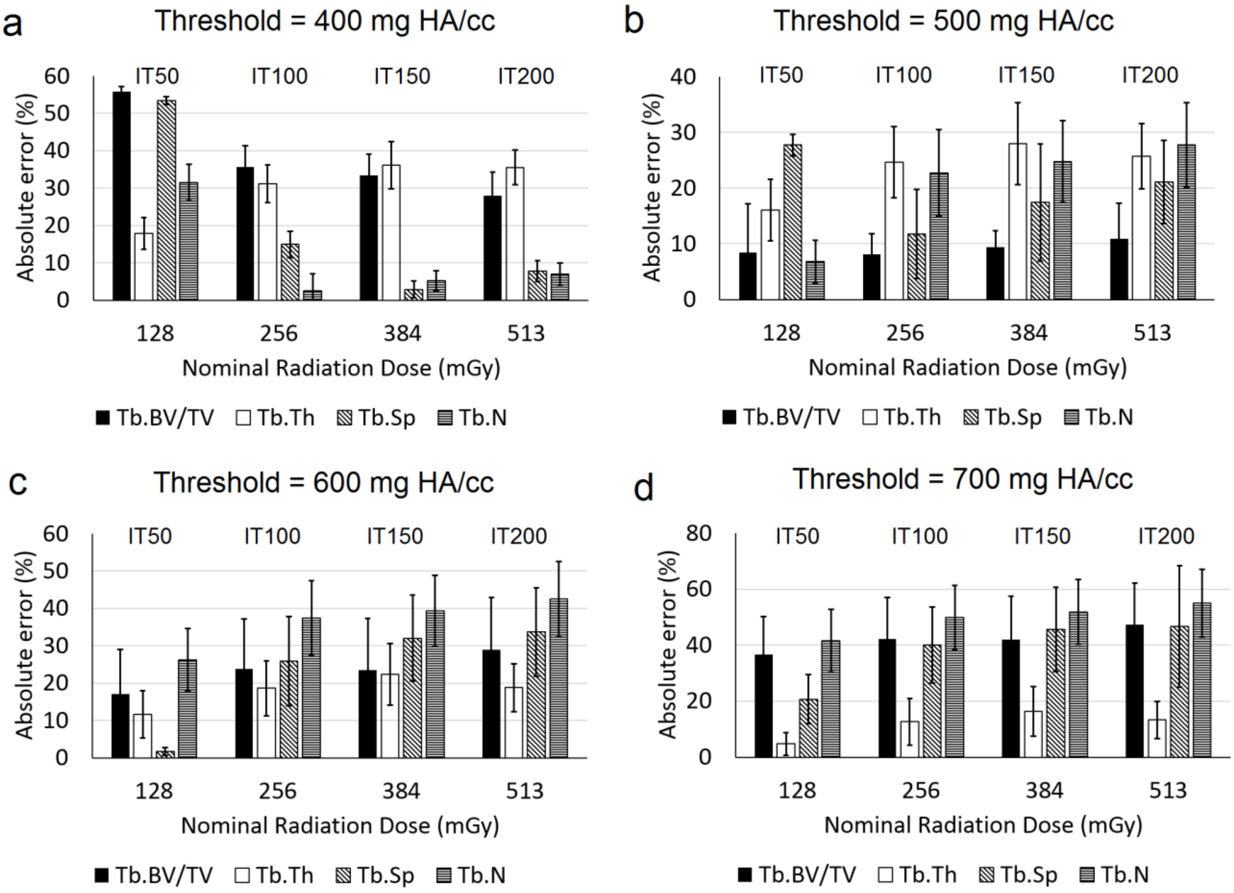

Figure 3.7.Absolute errors (median ± SD) in trabecular bone parameters measurements obtained using four different threshold values for segmentation: 400 mgHA/cc (a), 500 mgHA/cc (b), 600 mgHA/cc (c) and 700 mgHA/cc (d). Trabecular bone volume fraction (Tb.BV/TV), trabecular thickness (Tb.Th), trabecular separation (Tb.Sp) and trabecular number (Tb.N) are reported. IT50, IT100, IT150 and IT200 refer to the scanning procedure (50 ms, 100 ms, 150 ms and 200 ms integration time respectively), associated with a nominal radiation dose of 128, 256, 384 and 513 mGy respectively.

Similarly to what observed previously, errors tended to converge with integration time, but absolute values increased, while the opposite trend was expected. Exceptions were Tb.BV/TV, Tb.Sp and Tb.N for threshold = 400 mg HA/cc, which showed a decreasing trend (Fig. 3.7a). In particular, errors lower than 12% were found for IT150 and IT200 in Tb.Sp and Tb.N, which however resulted in higher errors in Tb.BV/TV and Tb.Th (up to 45%).

Among the above values, the best compromise for accurately measuring all trabecular parameters was achieved for threshold equal to 500 mg HA/cc (Fig. 3.7b). As discussed later, the selected automatic segmentation method (average of the grey levels corresponding to the bone and background peaks in the image histogram) led to threshold values in the range of 499 to 568 mg HA/cc depending on the sample, which confirmed it was a suitable method for image segmentation.

3.3.4 Spatial Distribution of BMC and TMD

In Fig. 3.8, absolute errors (median ± SD) for BMC and TMD measurements are reported for three of the ten longitudinal sections. For each section, errors associated to the four sectors are reported (anterior, lateral, posterior and medial). Partition 1 was the most proximal portion of the VOI, partition 5 was the middle one and partition 10 was at the distal end of the VOI. Similar trends were found for all sub-regions. In all cases, errors decreased with increasing integration time. Errors in BMC were in the ranges of 1-28% for IT50, 1-24% for IT100, 1-24% for IT150, 0-20% for IT200. The highest errors and variability were found in the proximal partitions (Fig. 3.8a), probably due to the presence of the trabecular region, while lower errors were found for the partitions located in the medial region (Fig. 3.8c). Errors in TMD were in the ranges of 2-18% for IT50, 0-14% for IT100, 0-14% for IT150, 2-11% for IT200.

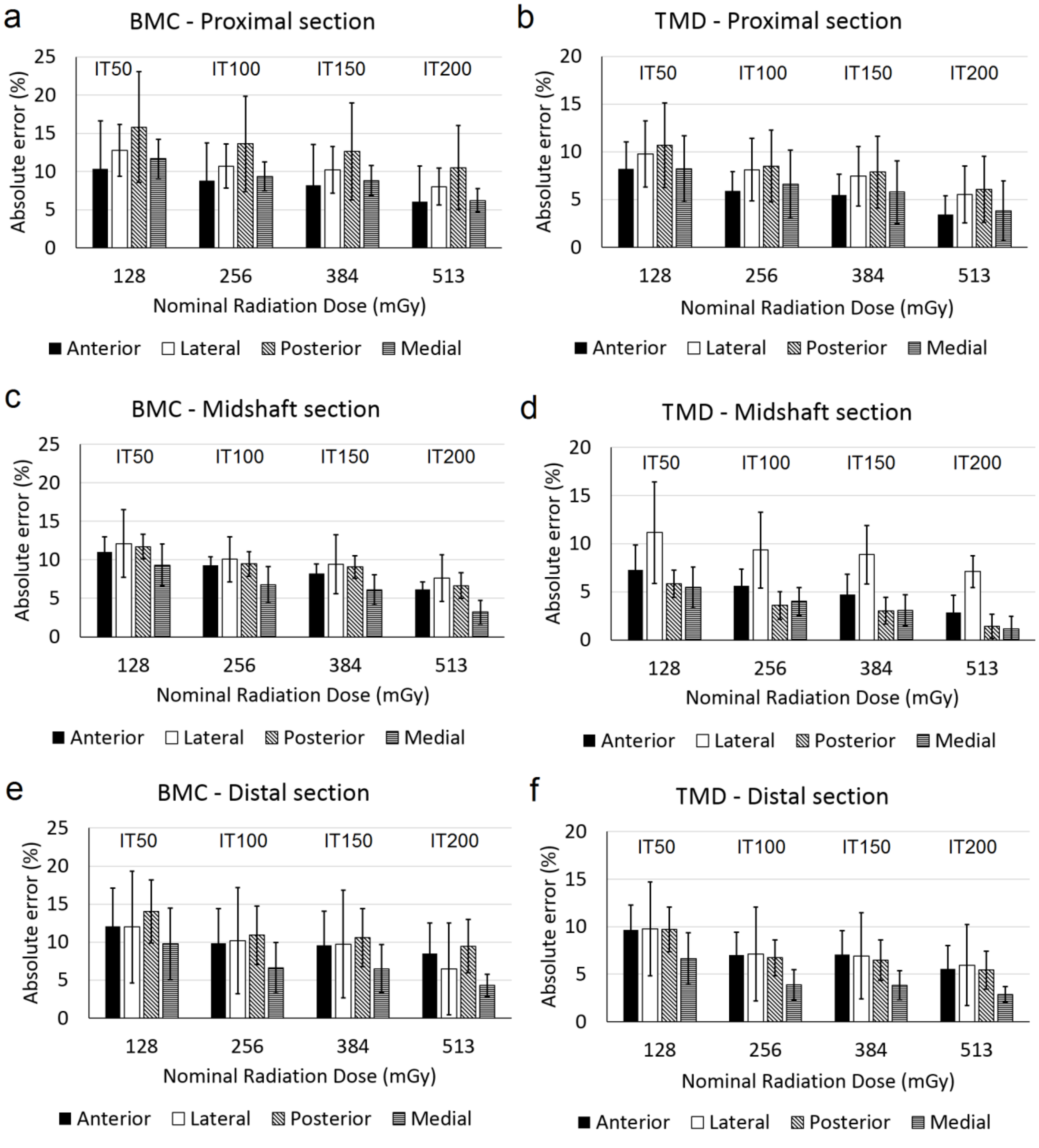

***Figure 3.8**. Effect of scanning procedure on bone mineral content (BMC) and tissue mineral density (TMD) in the proximal (a-b), medial (c-d) and distal (e-f) partitions. Absolute errors are reported as median ± SD. IT50, IT100, IT150 and IT200 refer to scanning protocols with 50, 100, 150 and 200 ms integration time respectively, associated with a nominal radiation dose of 128, 256, 384 and 513 mGy respectively.*

3.3.5 Micro-Finite Element Models

MicroFE models generated from high resolution images contained about 120 million elements and required about three hours CPU time for meshing and about 270 hours CPU time for each simulation (HPC Beagle, INSIGNEO, University of Sheffield; 64 cores, maximum memory = 738 GB). MicroFE models developed for the other procedures contained approximately 10 million elements and required about 30 minutes CPU time for meshing and 23 hours CPU time for each simulation (64 cores, maximum memory = 75 GB).

The effect of integration time on estimated mechanical properties was minor and errors were low for all procedures (0-4% for stiffness and 1-7% for strength considering all scanning procedures and specimens, Fig. 3.9).

In Fig. 3.10, the distributions of first and third principal strains are reported. Comparable strain distributions were found for all scanning procedures. In uniaxial compression, the maximum compressive strains were located at the postero-lateral apex, corresponding to the curvature of the tibia (Fig. 3.10b).

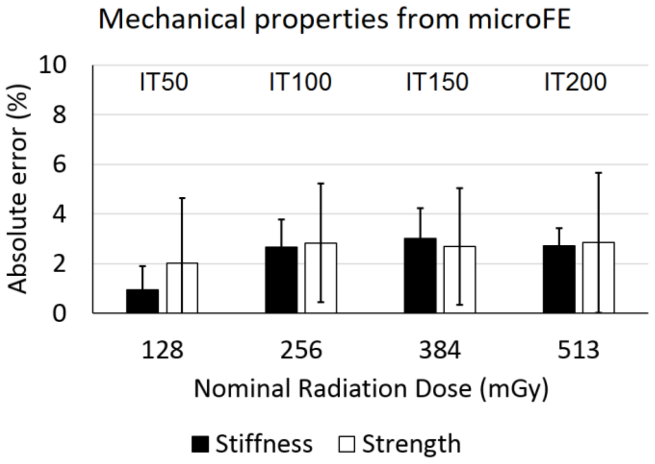

***Figure 3.9**. Effect of scanning procedure on the estimations of stiffness and strength from micro-finite element (microFE) models. Absolute errors are reported as median ± SD. IT50, IT100, IT150 and IT200 refer to scanning protocols with 50, 100, 150 and 200 ms integration time respectively, associated with a nominal radiation dose of 128, 256, 384 and 513 mGy respectively.*

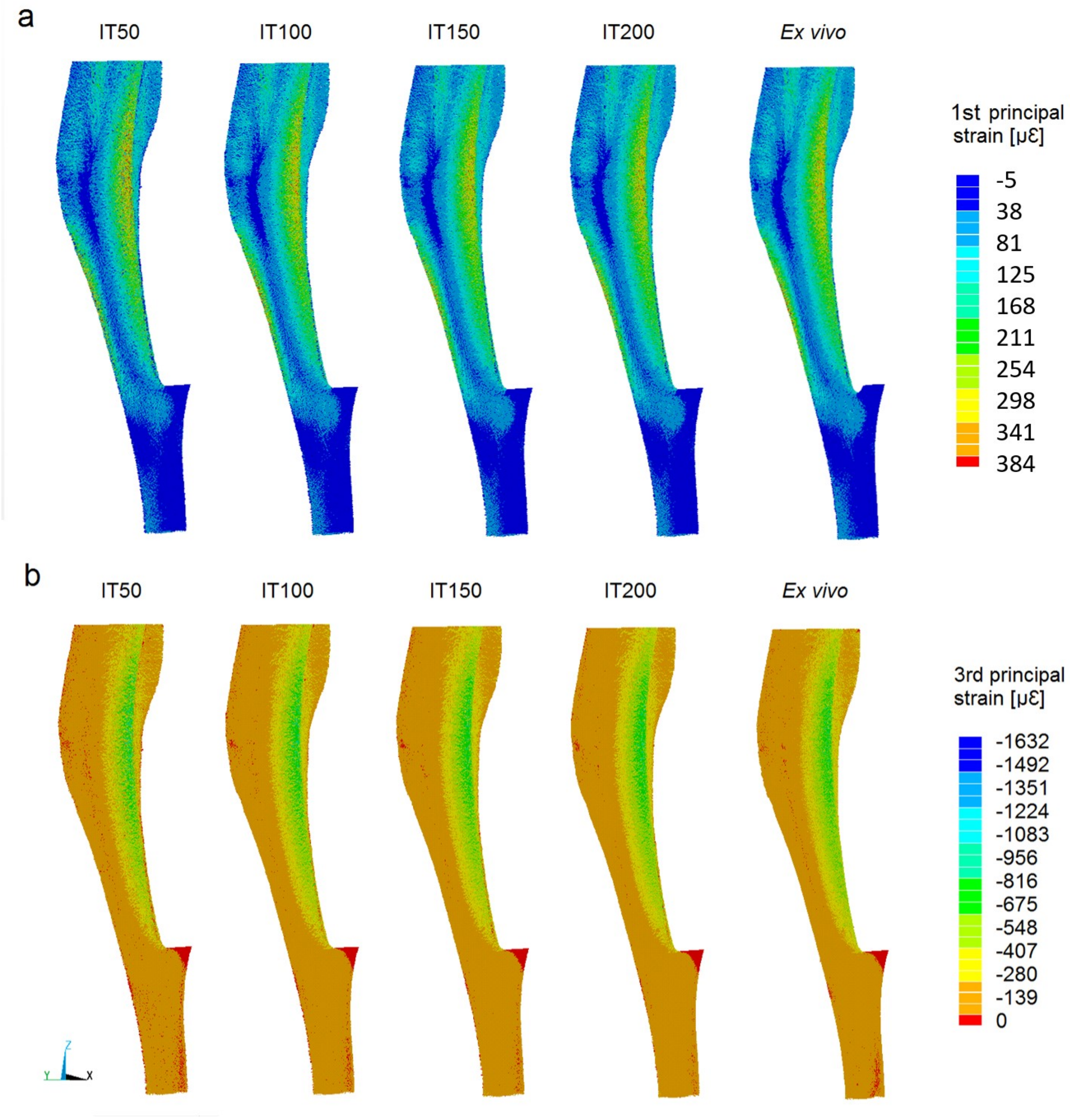

Figure 3.10*.Distribution of first (a) and third (b) principal strains over the tibia for the four in vivo scanning procedures (IT50, IT100, IT150 and IT200 correspond to 50, 100, 150 and 200 ms integration time, respectively) and the ex vivo scanning procedure (SRT sample).*

3.3.6 Influence of trabecular bone on the apparent mechanical properties

Results from the FE analysis of tibiae including and excluding the trabecular bone are reported in Table 3.2.

		Including trabecular bone	Excluding trabecular bone	Difference (%)
Stiffness (N/mm)	OLT	249	248	-0.395
	ORT	248	247	-0.434
	SLT	237	235	-0.520
	SRT	235	234	-0.310
Strength (N)	OLT	19.11	19.11	-0.002
	ORT	18.46	18.46	-0.003
	SLT	18.58	18.58	-0.004
	SRT	17.21	17.21	-0.008

Table 3.2*.Stiffness and strength estimated for four tibiae (OLT, ORT, SLT and SRT). For each sample, microFE models were generated by including or excluding the trabecular region.*

The presence of trabecular bone had minor effect on the overall mechanical properties of the bone. Stiffness seemed to be slightly reduced when trabecular bone was excluded, however the percentage reduction was lower than 1% in all cases. Percentage reduction in strength was lower than 0.01% for all tibiae.

3.4 DISCUSSION

In this study the effect of image quality, tuned by changing the integration time in microCT scanning procedure, on morphometric, densitometric and mechanical properties measurements of the mouse tibia was evaluated. The goal of the study was to quantify the measurement errors associated with each scanning procedure in order to find an acceptable compromise between nominal radiation dose and measurement accuracy. The results showed a large dependency of the trabecular parameters on the integration time, weaker dependency for cortical areas and BMC distribution, and minor effect on cortical thickness and mechanical properties estimated by microFE models.

For trabecular morphometric parameters, integration time led to large differences in measurements errors, up to 10% for Tb.BV/TV, 14% for Tb.Th, 16% for Tb.Sp and 28% for Tb.N, which was the most affected parameter. Errors showed a converging trend for increasing integration time, however they tended to increase with increasing integration time while the opposite trend was expected. This is probably due to the different partial volume effect in the *in vivo* (voxel size 10.4 µm, best achievable with our *in vivo* microCT) and *ex vivo* (voxel size 4.3 µm) scanning protocols. In a previous study, it has been shown that increasing the voxel size leads to overestimations in trabecular bone volume fraction and trabecular thickness (Christiansen, 2016). The segmentation method can also affect the measurements accuracy significantly (Christiansen, 2016). However, there is no consensus among different studies about what is the best method to segment microCT images (Bouxsein et al., 2010). In some studies, threshold has been selected manually based on visual comparison between the greyscale and segmented images (Christiansen, 2016, Holguin et al., 2014, Patel et al., 2014). In other studies, it has been calculated based on the histogram, e.g. mean of the grey values corresponding to the peaks (Christiansen, 2016), one-third of the bone peak (Main et al., 2014), 25.5% of maximum greyscale value (Klinck et al., 2008). Each method leads to a different threshold value (from approximately 420 mg HA/cc in (Klinck et al., 2008) to 813 mg HA/cc in (Birkhold et al., 2014a)) and may induce measurement errors. The approach selected in this study (i.e. midpoint between the bone and background peaks in the histogram) tried to minimize the effect of thresholding by using a repeatable and user-independent method, which allowed for consistent segmentation among different samples, scanning procedures and operators. Segmented images have also been inspected by comparison to the greyscale ones as suggested by the guidelines (Bouxsein et al., 2010). The resulting thresholds ranged from 499 to 568 mg HA/cm^3 equivalent BMD among the samples, which led to low absolute errors for all trabecular parameters as shown by the sensitivity analysis (Paragraph 3.3.3).

Cortical parameters were characterized by smaller errors and smaller effect of integration time (maximum variations due to integration time of 1-3%). As expected, lower errors for higher integration time were found for most cortical parameters, with the exception of Ct.Th, which seemed not affected by integration time. The weak dependency of the cortical parameters on integration time can be linked to the simplified structures to be analyzed compared to the complex tortuous trabecular structure with thinner features and larger bone surface.

Errors in BMC estimations showed a decreasing trend and a smaller influence of integration time (1-10%) compared to trabecular morphometric parameters. This is probably due to the fact that BMC measurements are less affected by the segmentation procedure and are more reproducible than morphometric measurements (Lu et al., 2016). Similarly, integration time had a small effect on local TMD measurements (differences of 1-7%).

Stiffness and strength estimated by microFE models were almost independent from integration time (differences of 1-3%). This is linked to the fact that the errors for cortical parameters were smaller, since the overall mechanical properties of the mouse tibia under uniaxial compression are mainly determined by cortical bone (Paragraph 3.3.6). In fact, the maximum strains were localized in the cortical compartment at the postero-lateral apex (Fig. 3.10). Similar findings were reported by (Patel et al., 2014) and by (Yang et al., 2014), who found the maximum compressive and tensile strains in the trabecular bone to be 10% and 34% lower than those at the midshaft, by simulating uniaxial compression of the whole tibio-fibular structure.

The main limitation of this study is the low sample size (four). Nevertheless, a comprehensive analysis has been performed for each sample, including the analysis of bone microstructure in the trabecular and cortical regions, the spatial distribution of BMC and TMD in the whole tibia, and mechanical properties estimated with specimen-specific microFE models. Additionally, tibiae which underwent different interventions were used (WT and OVX, irradiated and non-irradiated), thus taking into account the potential variability among different bones in longitudinal studies. Although the absolute errors for most parameters varied among the specimens, their trends with integration time were similar, suggesting that the reduction of this scanning parameter is a good strategy for limiting the radiation dose.

Possible improvements in the measurement of trabecular morphometric parameters could be achieved by applying more advanced segmentation techniques (Buie et al., 2007, Waarsing et al., 2004b), which have not been investigated in this study.

Finally, the microFE models used in this study were based on a simplified Cartesian mesh with homogeneous isotropic linear elastic material properties. Since the main goal of this study was to evaluate the effect of integration time on predicted mechanical properties, in first approximation the effect of local mineralization was assumed to be negligible, which was confirmed by the small differences found in local TMD measurements (Paragraph 3.3.4). Nevertheless, in the future the models could be improved by using a tetrahedral mesh and heterogeneous material properties based on the local mineralization. In this perspective, the main issue is related to the constitutive law to convert TMD into Young's modulus. Different laws have been reported in the literature (Currey, 1988, Easley et al., 2010, Gross et al., 2012, van Ruijven et al., 2007) and in order to choose the best approach a comprehensive validation study and characterization of the bone material in the mouse tibia would be required.

3.5 CONCLUSION

In conclusion, in this study the effect of decreasing the integration time for microCT scans of the mouse tibia has been investigated by quantifying the measurement errors associated with different scanning procedures. Considering the obtained results, the IT100 scanning procedure (energy 55 kVp, current 145 µA, voxel size 10.4 µm, integration time 100 ms, field of view 32 mm, 750 projections/180°, no frame averaging, 0.5 mm Al filter) has been selected as the best compromise between nominal radiation exposure and accuracy in the estimation of bone parameters. Using this protocol, a 50% reduction in nominal radiation exposure can be achieved compared to the IT200 scanning protocol (used in a previous study in our group (Lu et al., 2017)). Maximum differences in measurement errors between the two procedures were 7% for morphometric parameters, 4% for local BMC and 1% for microFE estimations of stiffness and strength, meaning that a comparable accuracy in the image-based measurements can be achieved. Therefore, the IT100 scanning protocol has been applied for microCT imaging of the tibia in the subsequent analyses.

CHAPTER 4

VALIDATION OF FINITE ELEMENT MODELS OF THE MOUSE TIBIA USING DIGITAL VOLUME CORRELATION

Part of this chapter has been originally published in Oliviero, S., Giorgi, M., Dall'Ara, E. 2018. Validation of finite element models of the mouse tibia using digital volume correlation. *Journal of the Mechanical Behavior of Biomedical Materials,* 86, 172-184.

DOI: https://doi.org/10.1016/j.jmbbm.2018.06.022

SUMMARY

Micro-Finite Element (microFE) models based on micro-Computed Tomography (microCT) images can estimate the mechanical properties of the mouse tibia non-invasively but their outputs need to be validated with experiments. Digital Volume Correlation (DVC) can provide experimental measurements of displacements over the whole bone volume under loading. In this study, DVC was applied to validate the local predictions of microFE models of the mouse tibia loaded in compression.

Six mouse tibiae were stepwise compressed within a microCT system. MicroCT images were acquired in four configurations with applied compression of 0.5 N (preload), 6.5 N, 13.0 N and 19.5 N. Failure load was measured after the last scan. A global DVC algorithm was applied to the microCT images in order to obtain the displacement field over the bone volume. Homogeneous isotropic linear elastic hexahedral microFE models were generated from the images collected in the preload configuration with boundary conditions interpolated from the DVC displacements at the extremities of the tibia. Experimental displacements from DVC and numerical predictions were compared at corresponding locations in the middle of the bone. Stiffness and strength were also estimated from each model and compared with the experimental measurements.

The magnitude of the displacement vectors predicted by microFE models was highly correlated with experimental measurements ($R^2 > 0.82$). Higher but still reasonable errors were found for the Cartesian components. The models tended to overestimate local displacements in the longitudinal direction ($R^2 = 0.69 - 0.92$, slope of the regression line = 0.50 – 0.97). Errors in the prediction of structural mechanical properties were 14 ± 11% for stiffness and 9 ± 9% for strength. In conclusion, the DVC approach has been applied to the validation of microFE models of the mouse tibia. The predictions of the models for both structural and local properties have been found acceptable for most preclinical applications.

4.1 INTRODUCTION

The mouse tibia is a common anatomical site where to investigate bone remodeling and the effect of bone treatments, e.g. it has been used to study the bone response to *in vivo* mechanical stimulation (Birkhold et al., 2015, Holguin et al., 2014), to ovariectomy (Klinck et al., 2008, Waarsing et al., 2004a), to ageing (Buie et al., 2008, Main et al., 2010) and to pharmacological treatments (Campbell et al., 2014, Lu et al., 2017). In longitudinal studies, micro-Finite Element (microFE) models based on *in vivo* micro-Computed Tomography (microCT) images (van Rietbergen et al., 1995) can potentially be used to predict the bone mechanical behavior under loading non-invasively. Nevertheless, before their application in preclinical assessments, such models should be validated against accurate experiments. The prediction of bone stiffness by microFE models has been extensively validated for trabecular bone specimens (Schwiedrzik et al., 2016, Wolfram et al., 2010) and human vertebral bodies (Dall'Ara et al., 2012). However, quantifying the local strains over the whole volume in a spatially resolved fashion is relevant to investigate bone adaptation. It has been shown that remodeling seems mechano-regulated by the local strains, both in the mouse tibia (Birkhold et al., 2016) and in the caudal vertebra (Schulte et al., 2013a). Therefore, validating the microFE predictions at the local level is fundamental in order to obtain reliable information about the local mechanical environment engendered in the bone under loading.

Strain gauges, Digital Image Correlation (DIC) and Digital Volume Correlation (DVC) can be used to measure local displacements and strains of loaded bone specimens (Grassi and Isaksson, 2015). On the mouse tibia, strain gauge measurements have been performed for determining the local strains caused by an external load and for validating the local predictions of strain by microFE models (Patel et al., 2014, Razi et al., 2015, Stadelmann et al., 2009, Yang et al., 2014). The main limitation of this method is that only a few strain gauges can be attached on a single tibia due to its small size (maximum of three strain gauges in (Patel et al., 2014) and in (Stadelmann et al., 2009)), and the measurement obtained represents the average strain over a relatively large surface (typical size of the active gauge = 0.38 mm x 0.50 mm). Additionally, strain gauges should be ideally applied on flat surfaces, hard to find in the mouse tibia, and the attachment of the sensor itself may cause a local stiffening of the specimen, as shown on the mouse forearm (Begonia et al., 2017). Digital Image Correlation (DIC) is a contactless method based on the acquisition with digital cameras of several images of the external surface of the sample during the mechanical test, which are then used to retrieve the displacement field. The surface of the sample is conveniently speckled in order to create a random pattern, which is subsequently used to identify corresponding points in the two images based on an image correlation approach. DIC has been applied on the mouse tibia in order to quantify the distribution of strains on the surface during loading (Sztefek et al., 2010) and the sensitivity of the technique to different parameters (e.g. speckle size and density) has been analyzed (Carriero et al., 2014). DIC measurements have also been compared to microFE predictions of strains on the mouse tibia surface (Pereira et al., 2015) and on the mouse ulna and radius (Begonia et al., 2017). However, DIC can only provide measurements on a portion of the external surface of the sample. In order to overcome this limitation, DVC can be applied to two (or more) three-dimensional microCT images of the sample acquired during stepwise loading (Bay et al., 1999). A deformable registration approach calculates the local displacements over the whole volume of the specimen that can be differentiated into a strain field. DVC has been applied to trabecular bone samples (Chen et al., 2017, Gillard et al., 2014, Roberts et al., 2014, Zauel et al., 2005), human vertebra (Hussein et al., 2012), porcine vertebra (Costa et al., 2017), but it has never been applied on the mouse tibia. The main limitations of DVC are: 1) the requirement of performing stepwise loading to allow the acquisition of microCT scans between each load-step; and 2) the need of finding a compromise between measurement accuracy and spatial resolution of the method (Dall'Ara et al., 2014, Dall'Ara et al., 2017). While for displacement measurements a good compromise can be found (accuracy in the order of a fraction of the voxel at spatial resolution of 5 voxels, Palanca et al. 2015), acceptable uncertainties in strain measurements can only be obtained at very coarse resolutions (Grassi and Isaksson, 2015, Palanca et al., 2015).

The aim of this study was to use the DVC technique to validate local displacements predicted by microFE models in the mouse tibia under compression. Global stiffness and strength were also estimated from microFE models and compared to the experimental measurements.

4.2 MATERIALS AND METHODS

For the validation of microFE models of the mouse tibia a similar workflow previously applied for trabecular bone (Chen et al., 2017) and porcine vertebral bodies (Costa et al., 2017) was used. Mouse tibiae were stepwise compressed within a microCT scanner, in order to acquire images in different loading configurations. Afterwards, a deformable registration algorithm was applied to the microCT images to compute the displacement field. In order to adapt the DVC approach for the mouse tibia, the following preliminary analyses were performed: 1) selection of the rigid registration procedure to align the microCT images (paragraph 4.2.3); 2) quantification of the precision of DVC measurements (paragraph 4.2.5); 3) repeatability of DVC measurements (paragraph 4.2.6); 4) spatial distribution of the error for the strains measured with DVC (paragraph 4.2.7). MicroFE models were generated from the microCT images acquired in the preloaded configuration. In order to validate the microFE models, experimental and numerically predicted displacements were compared at corresponding locations. Details of each step are reported below.

4.2.1 Sample preparation

Six right mouse tibiae were obtained from C57BL/6J female mice used for previous studies (Lu et al., 2015, Lu et al., 2017) (Table 4.1). Tibiae were dissected from 22-weeks-old mice which underwent ovariectomy at week 14 of age (Lu et al., 2015) (N=2), from 24-weeks-old wild type mice (N=2), and from 16-weeks-old wild type mice (N=2). After carefully removing soft tissues with a scalpel, the tibiae were kept frozen at -20°C until testing. Total bone mineral content (BMC) and tissue mineral density (TMD) were computed from the microCT scans of the specimens as described below.

	Group	Age [weeks]	Length [mm]	BMC [mg]	TMD [mgHA/cc] Mean±SD
Sample1	Ovariectomy	22	18.57	16.77	1078 ± 222
Sample2	Ovariectomy	22	18.70	16.66	1058 ± 216
Sample3	Wild type	24	17.95	16.74	1119 ± 228
Sample4	Wild type	24	17.09	14.26	1094 ± 221
Sample5	Wild type	16	17.76	14.51	1051 ± 225
Sample6	Wild type	16	17.63	14.23	1034 ± 219

Table 4.1*. Overview of the properties of the tested right mouse tibiae dissected from female C57BL/6J mice. For each specimen group, age, length, total bone mineral content (BMC) and tissue mineral density (TMD) are reported.*

In order to align and grip the samples to the loading device, the extremities of the tibiae were embedded in resin (Technovit 4071, Kulzer, Germany) (Fig. 4.1A). Dissected tibiae were defrosted at room temperature in saline solution for 2 hours and subsequently dehydrated in air for 1 hour for the embedding. The total length was measured using a caliper. The fibula was removed with a scalpel with a cut above the tibio-fibular joint. The longitudinal axis of the tibia was visually aligned to a vertical reference and the distal end was embedded in resin until the 10% of the total length. The same procedure was applied to embed the proximal end. After embedding both ends in resin, the tibia was frozen again until testing.

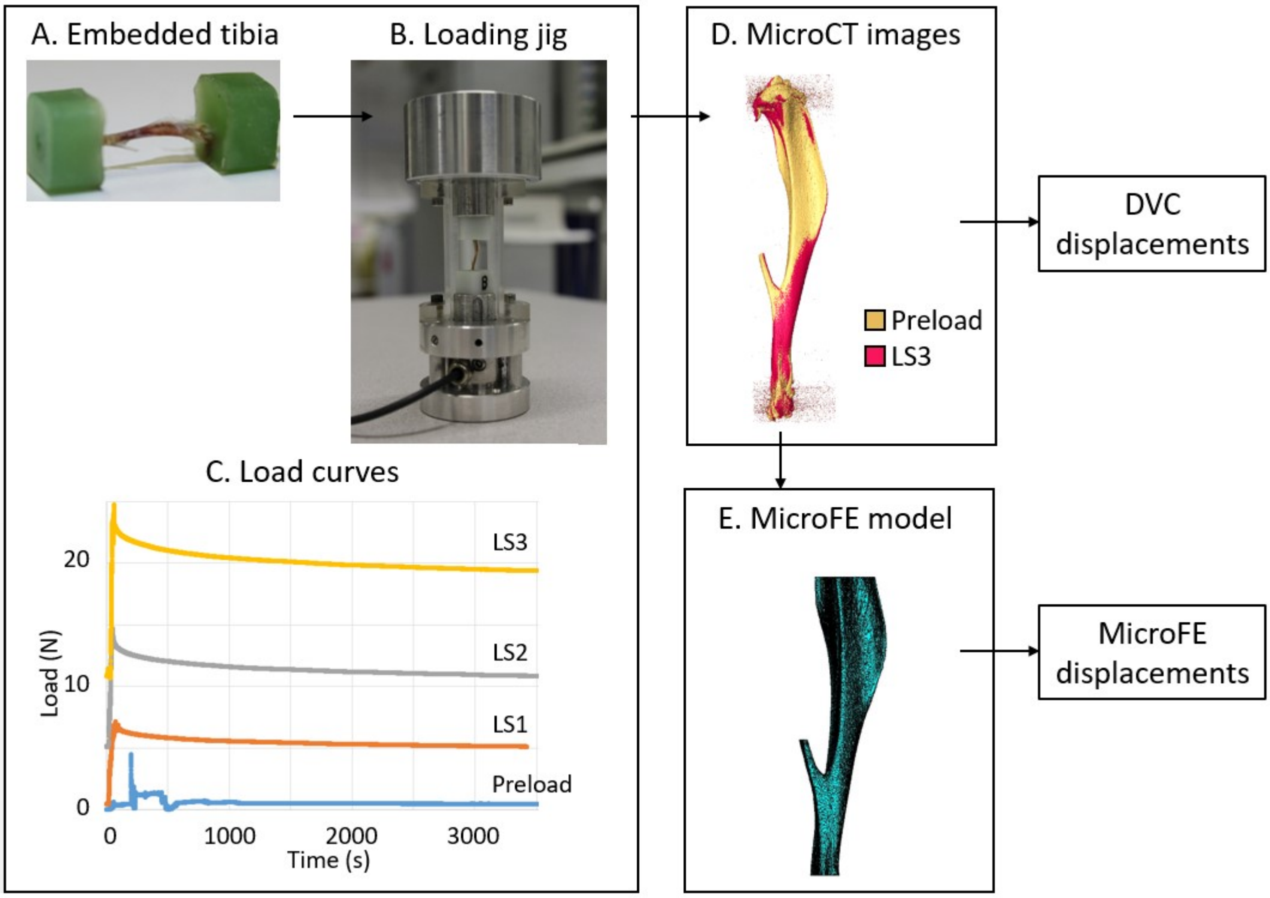

Figure 4.1*. Overview of the methods. Extremities of the tibiae were embedded in resin (A). After rehydration, the sample was placed into the loading device (B). A gauze soaked in saline solution was placed around the bone to keep it hydrated during the test. Tibiae were stepwise compressed at four load levels (C): 0.5N (preload), 6.5N (LS1), 13.0N (LS2) and 19.5N (LS3). At each load level, after relaxation a microCT image was acquired and registered to the preload one (D). MicroFE models (E) were developed from the images in the preload configuration.*

4.2.2 Stepwise compression tests and microCT imaging

Each embedded tibia was defrosted, rehydrated in saline solution for 3 hours and then placed in the loading device (Fig. 4.1B) designed in a previous study (Giorgi and Dall'Ara, 2018) wrapped in a saline solution-soaked gauze, in order to avoid dehydration during the test. The loading device was placed into a microCT system (VivaCT 80, Scanco Medical, Bruettisellen, Switzerland). Stepwise compression tests were performed by means of a screw-ball joint and the axial load was measured with a 100 N load cell (C9C, HBM, United

Kingdom). In order to reduce the effect of relaxation, at each load step the microCT image acquisition was started after 25 minutes. The procedure was repeated for four different target load levels (Fig. 4.1C): axial load of 0.5N to avoid moving artifacts during the scan (hereafter referred to “Preload”); axial load of 6.5N in the elastic range, defined as half of the typical one applied during *in vivo* loading of the mouse tibia (De Souza et al., 2005) (hereafter referred to “LoadStep1” or “LS1”); axial load of 13.0N, representative of a typical load applied in *in vivo* tibia loading experiments (De Souza et al., 2005) (hereafter referred to “LoadStep2” or “LS2”); axial load of 19.5N to study the inelastic range (hereafter referred to “LoadStep3” or “LS3”). In total, four microCT images were acquired for each sample. After the stepwise compression test, the tibia was loaded until failure and failure load was measured. The scanning protocol (55 kVp voltage, 145 μA intensity, 10.4 μm voxel size, 100 ms integration time, 32 mm field of view, 750 projections/180°, 0.5 mm Al beam hardening filter, no frame averaging) was suitable for *in vivo* application and was previously defined as an acceptable compromise between nominal radiation dose and the accuracy in measuring the bone properties (Oliviero et al., 2017). MicroCT images were reconstructed using the software provided by the manufacturer (Scanco Medical AG) and applying a beam hardening correction based on a phantom of 1200 mg HA/cc density, which has been shown to improve the local tissue mineralization measurement (Kazakia et al. 2008).

The grey values of the microCT images of the samples in the preload configuration were converted into tissue mineral density (TMD) equivalent values by using the calibration procedure suggested by the manufacturer of the microCT scanner, based on weekly quality checks performed on a densitometric phantom with five insertions (800, 400, 200, 100 and 0 mgHA/cc equivalent density, respectively). Bone mineral content (BMC) in each voxel was obtained as its TMD multiplied by the volume of the voxel. Total BMC (Table 4.1) was the sum of BMC in each bony voxel of the whole tibia. Additionally, mean and standard deviation of TMD over the bony voxels are reported (Table 4.1).

4.2.3 Selection of rigid registration method

MicroCT images were aligned using a rigid registration procedure by using as reference the image of each sample in the preload configuration (Fig. 4.1D).

A preliminary test was carried out on repeated scans of Sample4 in the preloaded configuration in order to define the rigid registration method. The second scan of the tibia was virtually deformed by applying a scaling factor of 0.995 in the longitudinal direction (Transform Editor, Amira 6.0.0, FEI Visualization Sciences Group, France), which caused a global displacement of 94 µm (similarly to what observed for LoadStep3). The obtained image was registered to the first scan using three different methods. The first method aimed at maximizing the alignment of the distal extremity between the deformed and preloaded images. The distal portions of the tibiae from both images until the tibio-fibular junction were segmented and rigidly registered in Amira (Amira 6.0.0, FEI Visualization Sciences Group, France) using Normalized Mutual Information as optimization criterion (Birkhold et al., 2014a). The transformation matrix obtained was applied to the original greyscale image, which was subsequently resampled using the Lanczos interpolator (Birkhold et al., 2014a). The second method was based on the greyscale values of the whole tibia. Normalized Mutual Information (Amira 6.0.0, FEI Visualization Sciences Group, France) was used as optimization criterion for aligning the greyscale virtually deformed image to the first scan. The third method aimed at minimizing the distance between the surfaces of the two tibiae. The surfaces of the tibiae were obtained in Amira (isosurface function) and imported in Matlab as point clouds. The transformation matrix was obtained in Matlab based on the Iterative Closest Point (ICP) algorithm (pcregrigid function), which was subsequently applied to align the greyscale image. In order to compare the three methods, for each couple of registered images cross-correlation (CC) and root mean square differences (RMSD) between the grey levels associated to corresponding voxels were computed. Percentage CC was calculated as percentage of the value obtained for two equal images. Percentage RMSE was calculated as percentage of the maximum greyscale value in the image. Based on the results (Paragraph 4.3.1), the first method was selected and used for the validation study.

4.2.4 DVC analyses

After the rigid registration, a deformable registration toolkit (Sheffield Image Registration Toolkit, ShIRT) (Barber and Hose, 2005, Barber et al., 2007, Khodabakhshi et al., 2013) was applied to compute the displacement field over the whole volume of the tibia for each load step. Briefly, in ShIRT a grid, with distance between the nodes of each cell equal to a selectable nodal spacing (NS), is overlapped to both the preload and deformed images. The registration equation is solved at the nodes of the grid by assuming trilinear interpolation within each cell. In order to select a suitable nodal spacing value, the precision of the displacements and strains computed by DVC was evaluated (Paragraph 4.2.5). Additionally, the results obtained with three different NS values (10, 25 and 50 voxels, Fig. 4.2) were compared for a subgroup of samples (N=4, Paragraph 4.3.2).

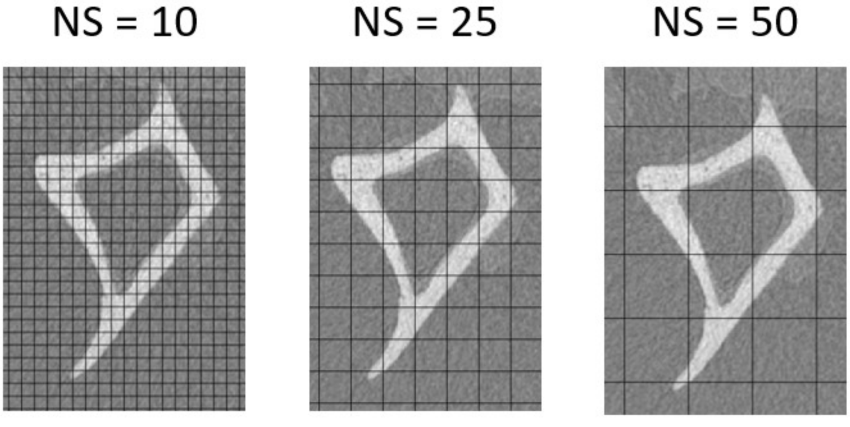

***Figure 4.2**. DVC grid superimposed to microCT images for nodal spacing (NS) equal to 10, 25 and 50 voxels.*

Following these analyses, a NS of 50 voxels (520 μm) was chosen and used for the validation study. For NS equal to 50 voxels, the precision error was smaller than 2.5 μm for displacement measurements and smaller than 300 με for strains (Paragraph 4.3.2). A mask was used in order to exclude the background from the DVC analysis, which was defined from the binary images of the samples by applying dilation (imdilate function, square structuring element of 50x50 pixels, Matlab) and filling (imfill function, Matlab) algorithms.

4.2.5 Precision of DVC displacements and strains

The uncertainties of the DVC measurement of displacements and strains were evaluated in order to define a suitable nodal spacing (NS) for the validation study on the mouse tibia (Dall'Ara et al., 2014). Two pairs of repeated scans were used (Sample2 scanned twice in the preload configuration, Sample4 scanned twice in the loaded configuration LS2 with 13.0N axial load). Repeated images were rigidly registered using the selected method previously described (alignment of the distal extremities, Paragraph 4.2.3). The DVC algorithm was applied using 11 different NS values ranging from 5 to 100 voxels. Precision error was calculated as the standard deviation of the Cartesian components of the displacements along each direction (Liu and Morgan, 2007, Palanca et al., 2015). Precision of the strain measurements was estimated as the standard deviation of the average of the absolute values of the six strain components (Liu and Morgan, 2007, Palanca et al., 2015). The analysis was performed in the middle 75% of the total length in order to reduce the possible boundary effects.

4.2.6 Repeatability of DVC measurements

The aim of this analysis was to evaluate the repeatability of DVC measurements of local displacements, by evaluating how the image processing steps influence the measured displacements. In particular, uncertainties are due to the initial alignment of the two microCT images (preload and deformed configurations), to the rigid registration procedure and to the deformable registration. Three repetitions of the image processing procedure were performed for one sample (Sample3, LoadStep2) and the correlation, root mean square differences (RMSD) and maximum differences (D.max) between displacements obtained from different repetitions were evaluated.

4.2.7 Spatial distribution of the errors for the strains measured with DVC

The gold standard method to assess the reliability of DVC measurements is based on quantifying the uncertainties in displacements and strains calculated in a zero-strain test, in which repeated scans are performed with no deformation of the sample (Paragraph 4.2.5). From this test, accuracy and precision error are evaluated over the whole region of analysis (Liu and Morgan, 2007, Palanca et al, 2015). However, there could be areas of the sample characterized by larger local errors. The aim of this analysis was to evaluate the accuracy of local strains obtained from DVC, which is linked to the accuracy of the measured displacement field. Repeated scans of Sample2 were used. The second scan of the tibia was virtually deformed by applying a scaling factor of 0.995 in the longitudinal direction (Transform Editor, Amira 6.0.0, FEI Visualization Sciences Group, France), which caused a global displacement of 94 μm (similarly to what observed for LoadStep3). In this condition, the nominal strain is known, equal to 5042 με homogeneously distributed over the tibia. The obtained image was rigidly registered to the first scan and the DVC algorithm was applied using a nodal spacing of 50 voxels. A finite element (FE) package (ANSYS Academic Research, Release 15.0) was used to calculate strains from the DVC displacements.

4.2.8 MicroFE models

MicroFE models were created from the microCT images in the preloaded configuration as described in Chapter 3 (Fig, 4.1E). The embedded extremities of the tibia were identified from the images and excluded from the model (resulting in the exclusion of the growth plates). The cropped images were segmented using a global threshold, which was defined as the average of the grey levels corresponding to the bone and background peaks in the image frequency plot (histogram, (Chen et al., 2017, Christiansen, 2016)). Each bone voxel was converted into an 8-noded hexahedral element with isotropic linear elastic material properties. Young's Modulus of 14.8 GPa and Poisson's ratio of 0.3 were assigned (Webster et al., 2008). Boundary conditions were assigned by interpolating the DVC displacements at the proximal and distal ends of the microFE model (Chen et al., 2017), using a trilinear interpolation (CBDOF function, ANSYS Academic Research, Release 15.0). MicroFE models contained approximately 7 million elements and required about 2 hours CPU time for each simulation (HPC Iceberg, INSIGNEO, University of Sheffield; 8 cores, maximum memory = 48GB).

4.2.9 Comparison between experimental and computed displacements

Displacements obtained from DVC measurements and microFE predictions were compared over the whole volume of the tibia at corresponding locations, identified as the nodes of the DVC grid located inside the microFE mesh (which by construction were the centroids of the finite elements). In order to exclude the effect of boundary conditions, the comparison was performed in the middle 75% of the total length of the microFE model in the longitudinal direction. Linear regression analysis was used to estimate the relationship between measured and computed displacements (magnitude and Cartesian components). Outliers were defined using the Cook's distance method (Fox and Long, 1990): for each specimen, load step and direction, data points having Cook's distance higher than five times the mean Cook's distance were excluded from the analysis (Chen et al., 2017, Costa et al., 2017). For each sample, load step and direction, the following parameters of the regression have been computed: slope, intercept, coefficient of determination (R^2), root mean square error (RMSE), percentage root mean square error (RMSE%, calculated as percentage of the maximum absolute experimental value), maximum error (E.max) and maximum percentage error (E.max%, calculated as percentage of the maximum absolute experimental value).

4.2.10 Structural mechanical properties

Apparent stiffness and strength were measured and estimated from each model. Experimental stiffness was calculated by dividing the peak force measured during the mechanical test by the average displacement in the longitudinal direction obtained from the DVC in LoadStep2. Similarly, the microFE global stiffness was estimated from LoadStep2 by dividing the sum of the reaction forces along the longitudinal direction at the boundary surface by the average displacement along the longitudinal direction.

Experimental strength was measured during the mechanical test as the maximum load before failure of the tibia. From the linear microFE models, strength was estimated by assuming that the tibia fails when 2% of the nodes reach a critical strain (adapted from (Pistoia et al., 2002)) of either -10300 με in compression or 8000 με in tension (Bayraktar et al., 2004), and rescaling the predicted reaction force accordingly.

4.3 RESULTS

4.3.1 Selection of rigid registration method

In Table 4.2, cross-correlation (CC) and root mean square errors (RMSE) obtained for the three registration methods are reported. Results were comparable for all methods. The highest CC and lowest RMSE were obtained for the first method, which aimed at maximizing the alignment of the distal extremities between the virtually deformed image and the first scan. Additionally, this method better mimics the experimental conditions, since during the mechanical test the embedded distal portion of the tibia was fixed and the load was applied from the proximal end. Therefore, for the subsequent analyses the rigid registration was performed by using “Method 1”: aligning the distal end of the tibia segmented from the images in the loaded and preloaded configurations.

	Method 1	Method 2	Method 3
CC	7.91 * 10^{16}	7.88 * 10^{16}	7.89 * 10^{16}
CC (%)	99.00 %	98.55 %	98.71 %
RMSE	6576	7557	7178
RMSE (%)	10.03 %	11.53 %	10.95 %

***Table 4.2**. Cross-correlation (CC) and root mean square error (RMSE) obtained using three different methods for the rigid registration of the virtually deformed image on the reference one.*

4.3.2 Precision of DVC displacements and strains

In Fig. 4.3, the precision error is reported for displacements in the three directions and for strains in function of NS.

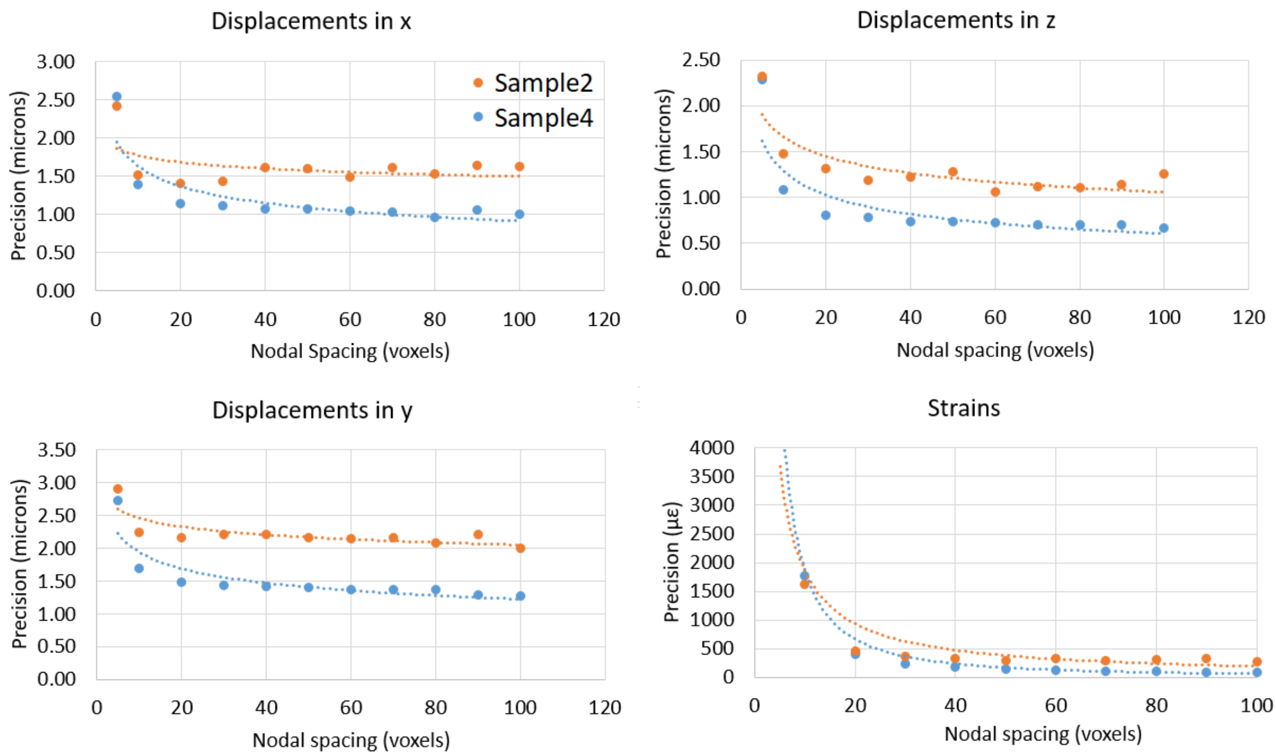

***Figure 4.3**. Precision error associated to the displacement measurements from the DVC (x, y and z directions). The precision of the method for strain measurements is also reported in function of nodal spacing. All results were obtained using repeated scans of Sample2 in preloaded configuration (orange) and Sample4 in loaded configuration (blue).*

Precision errors decreased with NS following power laws. For NS larger than 10 voxels (104 µm), the random errors associated to the displacement measurements along the three directions were lower than 2.5 µm, corresponding to one fourth of voxel size approximately. Based on this result, a further comparison among three different NS values (10, 25 and 50 voxels) is reported for the spatial distribution of DVC displacements over the tibia (Fig. 4.4) and for the parameters of the regression analyses between predicted and measured displacements (Table 4.3). Results are reported for Sample1 (best slope in Z direction, equal to 0.96) and Sample4 (worst slope, equal to 0.53) for LoadStep2.

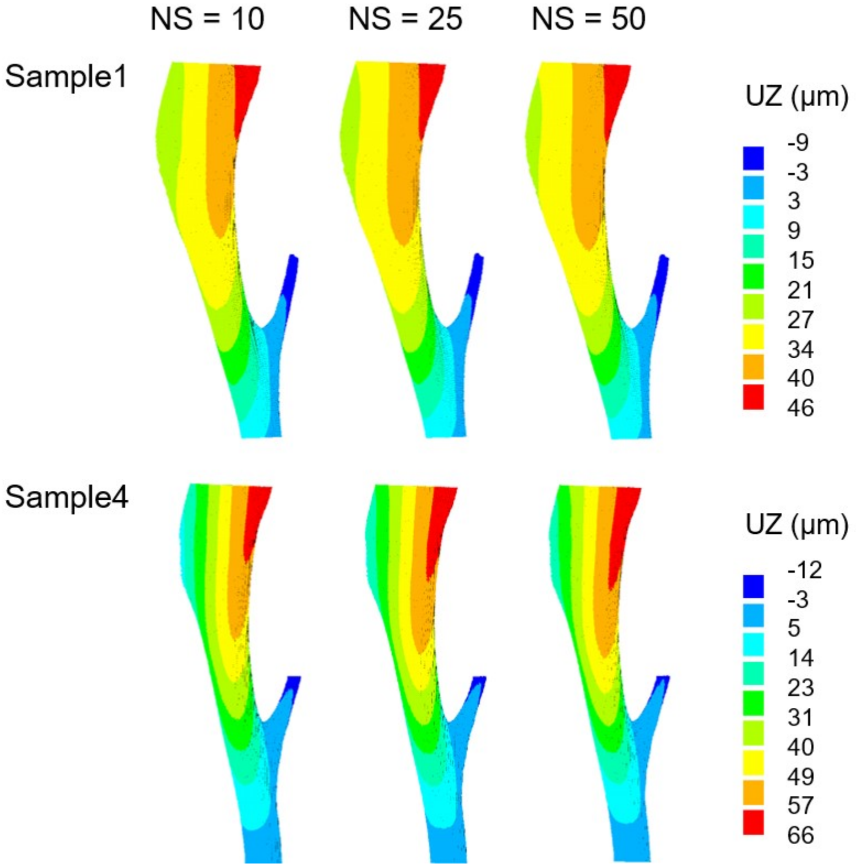

Figure 4.4. *Spatial distribution of longitudinal displacements (UZ) obtained with different nodal spacing (NS) values for Sample1 and Sample4 (LoadStep2).*

	NS = 10				NS = 25				NS = 50			
	X	Y	Z	||U||	X	Y	Z	||U||	X	Y	Z	||U||
Sample1												
Slope	0.95	1.27	0.90	**1.01**	0.93	1.29	0.87	**0.93**	0.91	1.14	0.96	**0.86**
Int[μm]	0	3	1	**5**	-4	7	1	**9**	-11	29	-1	**13**
R^2	0.98	0.98	0.93	**0.99**	0.97	0.98	0.91	**0.99**	0.95	0.97	0.80	**0.97**
RMSE[μm]	4	12	3	**6**	8	15	4	**6**	18	32	8	**6**
RMSE[%]	5	19	9	**6**	10	25	10	**6**	21	42	11	**5**
E.max[μm]	11	20	10	**14**	17	23	9	**11**	34	38	17	**13**
E.max[%]	14	31	25	**13**	24	37	25	**12**	40	49	24	**11**
Sample4												
Slope	0.87	1.05	0.70	**0.84**	0.82	1.03	0.60	**0.79**	0.84	1.42	0.53	**0.75**
Int[μm]	-8	22	1	**-3**	-10	30	0	**-5**	-24	50	7	**3**
R^2	0.99	0.88	0.89	**0.99**	0.98	0.75	0.81	**0.98**	0.97	0.80	0.77	**0.97**
RMSE[μm]	22	22	9	**22**	31	32	13	**32**	51	50	23	**44**
RMSE[%]	11	37	17	**11**	16	60	30	**16**	20	63	34	**17**
E.max[μm]	44	36	23	**44**	56	48	29	**59**	70	68	44	**67**
E.max[%]	22	59	45	**21**	29	90	70	**30**	28	85	65	**26**

***Table 4.3**. Parameters of the regression analysis for Sample1 and Sample4 obtained with different NS values. Slope, intercept (Int), coefficient of determination (R^2), root mean square error (RMSE), percentage RMSE, maximum error (E.max) and percentage E.max are reported.*

The spatial distribution of displacements over the tibia and the regression parameters were consistent for all NS values. Therefore, for the validation study a NS of 50 voxels was selected, based on the fact that the precision error of strains was lowest. For NS = 50 voxels, precision error of strain measurements was smaller than 300 με (Fig. 4.3), which is one order of magnitude lower compared to the typical peak strains engendered in the mouse tibia under *in vivo* compressive loading (in the range of -2300 to -3000 με (Patel et al., 2014)).

4.3.3 Repeatability of DVC measurements

DVC measurements of local displacements obtained from different repetitions were highly correlated ($R^2 > 0.99$, Table 4.4). Root mean square differences were in the range of 1-9% of the measured value, while maximum differences were in the range of 2-14% (Table 4.4).

Repetition 1 vs repetition 2			
	X	Y	Z
Slope	0.99	1.10	0.97
Intercept [µm]	2	7	2
R^2	1.000	0.999	0.999
RMSD [µm]	2	12	2
RMSD %	1	8	3
D.max [µm]	3	19	2
D.max %	2	13	4
Repetition 1 vs repetition 3			
	X	Y	Z
Slope	1.05	0.98	1.04
Intercept [µm]	-4	2	0
R^2	0.999	0.999	0.997
RMSD [µm]	9	2	1
RMSD %	5	2	3
D.max [µm]	20	5	4
D.max %	10	4	7
Repetition 2 vs repetition 3			
	X	Y	Z
Slope	1.06	0.89	1.07
Intercept [µm]	-6	-5	-2
R^2	0.999	0.997	0.996
RMSD [µm]	11	11	1
RMSD %	6	9	2
D.max [µm]	22	17	3
D.max %	11	14	5

***Table 4.4**. Parameters of the regression analysis comparing DVC measurements of local displacements obtained from three different repetitions of the image processing procedure. For each regression slope, intercept, coefficient of determination (R^2), root mean square difference (RMSD), percentage RMSD, maximum difference (D.max) and percentage D.max are reported.*

4.3.4 Validation of local displacements

After the analysis of outliers, less than 8% of the comparison points were excluded and the final number of points was in the range of 24 to 53 depending on the specimen. The linear regressions between the Cartesian components (UX, UY, UZ) and magnitude (||U||) of the displacements predicted by microFE models and experimentally measured by the DVC are reported in Fig. 4.5 for each specimen. Statistical parameters computed for each regression analysis are reported in Table 4.5.

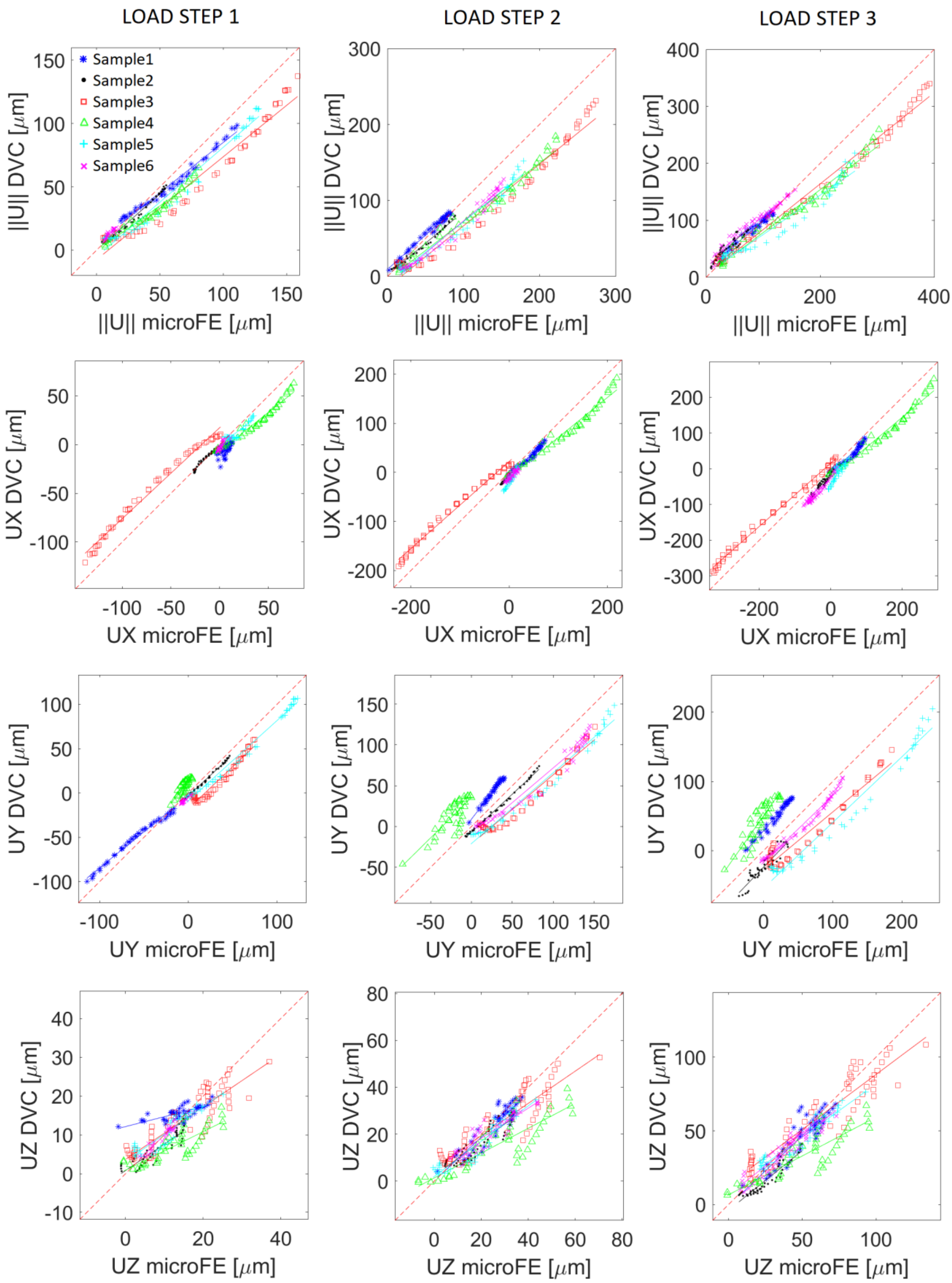

Figure 4.5. *Magnitude and Cartesian components of the displacements measured from the DVC analysis and predicted by the microFE models. Regression lines are reported for each sample (colours reported in the legend). The 1:1 relationship is plotted in red dashed line.*

	Load Step 1				Load Step 2				Load Step 3			
	X	Y	Z	||U||	X	Y	Z	||U||	X	Y	Z	||U||
Sample1												
Slope	0.76	0.81	0.26	**0.79**	0.89	1.30	0.92	**0.90**	0.91	1.14	0.96	**0.86**
Int[µm]	-10	-3	12	**6**	-5	9	0	**9**	-11	29	-1	**13**
R^2	0.37	0.99	0.53	**0.98**	0.97	0.98	0.84	**0.99**	0.95	0.97	0.80	**0.97**
RMSE[µm]	12	10	4	**9**	11	17	4	**5**	18	32	8	**6**
RMSE[%]	52	10	22	**9**	16	29	11	**6**	21	42	11	**5**
E.max[µm]	24	15	14	**14**	20	23	8	**9**	34	38	17	**13**
E.max[%]	103	15	70	**14**	31	39	22	**10**	40	49	24	**11**
Sample2												
Slope	1.00	0.93	0.68	**0.89**	1.14	0.93	0.73	**0.84**	1.13	1.04	0.81	**0.95**
Int[µm]	0	-3	1	**0**	-6	-7	2	**2**	-14	-24	-4	**16**
R^2	0.96	1.00	0.81	**0.99**	0.98	1.00	0.83	**0.99**	0.89	0.85	0.86	**0.85**
RMSE[µm]	2	5	3	**4**	7	10	5	**7**	18	25	10	**16**
RMSE[%]	6	11	21	**8**	27	13	15	**9**	23	38	24	**19**
E.max[µm]	4	7	7	**8**	9	14	12	**12**	28	38	17	**27**
E.max[%]	13	17	49	**15**	38	18	37	**15**	36	57	40	**32**
Sample3												
Slope	0.93	0.95	0.68	**0.81**	0.89	0.85	0.69	**0.81**	0.88	0.83	0.75	**0.80**
Int[µm]	17	-18	4	**-7**	22	-21	6	**-15**	16	-27	14	**4**
R^2	0.99	0.94	0.80	**0.96**	0.99	0.94	0.80	**0.97**	0.99	0.93	0.86	**0.99**
RMSE[µm]	23	20	5	**26**	36	34	9	**46**	38	42	14	**46**
RMSE[%]	19	34	16	**19**	19	28	17	**20**	13	29	13	**13**
E.max[µm]	30	27	12	**36**	52	45	20	**64**	64	57	34	**75**
E.max[%]	25	45	43	**27**	27	37	39	**27**	22	39	31	**22**
Sample4												
Slope	0.80	1.23	0.50	**0.71**	0.81	0.99	0.53	**0.77**	0.84	1.42	0.53	**0.75**
Int[µm]	-7	12	1	**0**	-10	35	1	**-4**	-24	50	7	**3**
R^2	0.96	0.68	0.69	**0.96**	0.97	0.67	0.75	**0.97**	0.97	0.80	0.77	**0.97**
RMSE[µm]	16	12	7	**14**	36	37	15	**36**	51	50	23	**44**
RMSE[%]	25	70	41	**22**	19	81	39	**20**	20	63	34	**17**
E.max[µm]	21	18	13	**22**	51	50	30	**55**	70	68	44	**67**
E.max[%]	32	102	78	**33**	27	109	77	**30**	28	85	65	**26**
Sample5												
Slope	0.77	0.90	0.70	**0.87**	1.70	0.87	0.75	**0.80**	1.48	0.95	0.72	**0.69**
Int[µm]	-1	-9	3	**-5**	-19	-21	2	**-8**	-40	-54	10	**6**
R^2	0.86	0.99	0.83	**0.97**	0.90	0.98	0.89	**0.97**	0.79	0.97	0.92	**0.94**
RMSE[µm]	6	16	3	**17**	17	34	5	**29**	35	62	8	**45**
RMSE[%]	20	15	13	**15**	45	23	15	**19**	60	30	10	**21**
E.max[µm]	12	25	5	**27**	27	50	9	**49**	51	86	17	**78**
E.max[%]	40	24	26	**24**	70	34	27	**32**	89	42	22	**36**
Sample6												
Slope	1.32	0.80	0.97	**0.93**	0.92	0.85	0.64	**0.85**	1.07	0.97	0.79	**0.81**
Int[µm]	-3	-5	0	**3**	-11	-13	5	**-12**	-25	-17	7	**26**
R^2	0.78	0.83	0.91	**0.82**	0.80	0.96	0.83	**0.97**	0.94	0.98	0.91	**0.95**
RMSE[µm]	4	4	1	**3**	12	28	6	**27**	29	20	6	**14**
RMSE[%]	50	32	6	**16**	60	23	17	**21**	28	19	10	**9**
E.max[µm]	6	5	2	**5**	18	48	11	**44**	38	29	14	**32**
E.max[%]	79	43	14	**31**	89	39	34	**34**	37	28	23	**21**

***Table 4.5**. Parameters of the regression analysis between measured and predicted displacements along the three directions and in magnitude, for each sample and each load step. For each regression the following parameters are reported: slope, intercept (Int), coefficient of determination (R^2), root mean square error (RMSE), percentage RMSE, maximum error (E.max) and percentage E.max.*

The magnitudes of predicted displacements were highly correlated with the corresponding experimental measurements ($R^2 > 0.82$ in all cases). Slopes of the regression lines were in the range of 0.69–0.95, indicating that microFE models tended to overestimate local predictions for increasing absolute displacements. Root mean square error varied according to the sample from 5% to 22% and no apparent effect of load level was observed. Higher variability and generally lower correlations were found for the Cartesian components. Displacements in the longitudinal direction Z showed fair to optimal correlations with the experimental ones, with R^2 in the range of 0.69–0.92 (with the exception of Sample1 in LoadStep1, for which $R^2=0.53$ was found, as discussed later). Slopes of the regression lines were in the range of 0.50–0.97 (with the exception of Sample1 in LoadStep1, for which slope=0.26, as discussed later), indicating an overestimation of local displacements in the loading direction, similarly to what observed for the displacement magnitude. Slopes for the transverse directions were in the range of 0.76–1.70 and 0.80–1.42 respectively, and errors were higher (RMSE of 6–60% for displacements along X and 10–81% along Y) compared to those computed along the longitudinal direction (RMSE of 6–41%). Absolute errors tended to increase with the load level: for LoadStep1 RMSE in the longitudinal direction was lower than 7μm for all samples, while for LoadStep3 RMSE up to 23μm was observed. However, percentage errors were comparable for all load steps.

The spatial distribution of the longitudinal displacement values over the tibia is reported in Fig. 4.6 for Sample1 (best slope, equal to 0.96) and Sample4 (worst slope, equal to 0.53) in LoadStep3. For Sample1, displacements were more homogeneously distributed over the tibia and the microFE model provided good predictions (slope=0.96, $R^2=0.80$). For Sample4, the distribution of displacements was more heterogeneous over the tibia, with higher gradients at the proximal end compared to the distal end, and microFE models tended to overestimate the local displacements (slope=0.53), even though correlation was good (R^2=0.77). The mode of deformation tended to differ between DVC measurements and microFE predictions, showing more accentuated bending in the second case, in the sagittal plane. Therefore, the comparison points characterized by the highest errors were located either in the anterior region of the tibia (corresponding to the tibial ridge) or in the posterior one (Fig. 4.6).

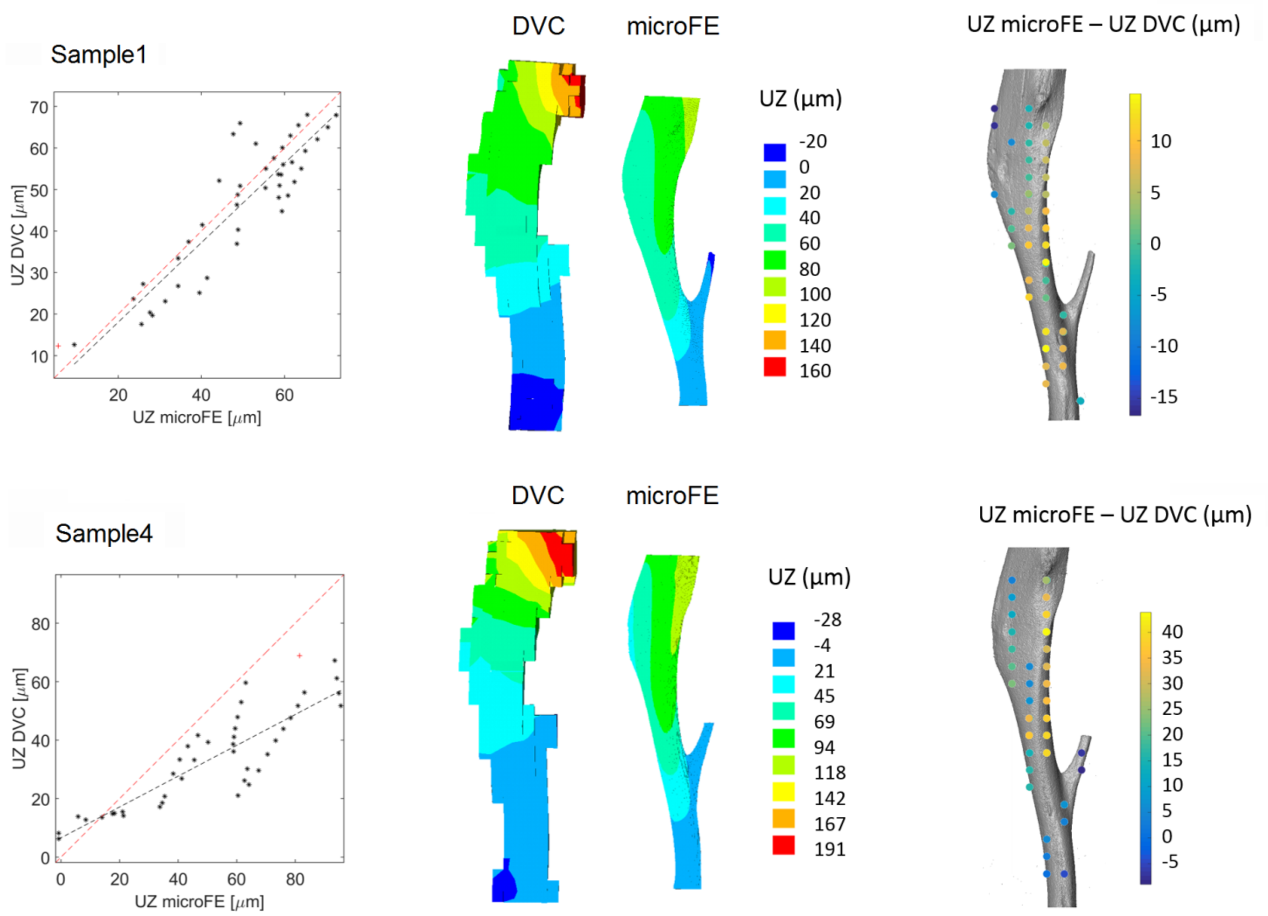

***Figure 4.6**. Spatial distribution of the displacements along the axial direction (UZ) and corresponding errors (UZ microFE – UZ DVC) for Sample1 and Sample4 in LoadStep3.*

4.3.5 Spatial distribution of the errors for the strains measured with DVC

In Fig. 4.7, the spatial distribution of DVC strains over the tibia, obtained by applying a virtual deformation to repeated scans, is reported. In this condition, the nominal strain is known, equal to 5042 με homogeneously distributed over the tibia. However, strains measured with DVC were not homogeneously distributed on the tibia, indicating that the accuracy of the DVC method may vary depending on the spatial location on the tibia, even if the global accuracy and precision are good. Peaks of error were located at the tibial ridge. This result suggests that the accuracy of local displacements may vary depending on the spatial location over the tibia, following a similar pattern found for strains. Therefore, measurements of local displacements at the tibial ridge are likely affected by higher errors.

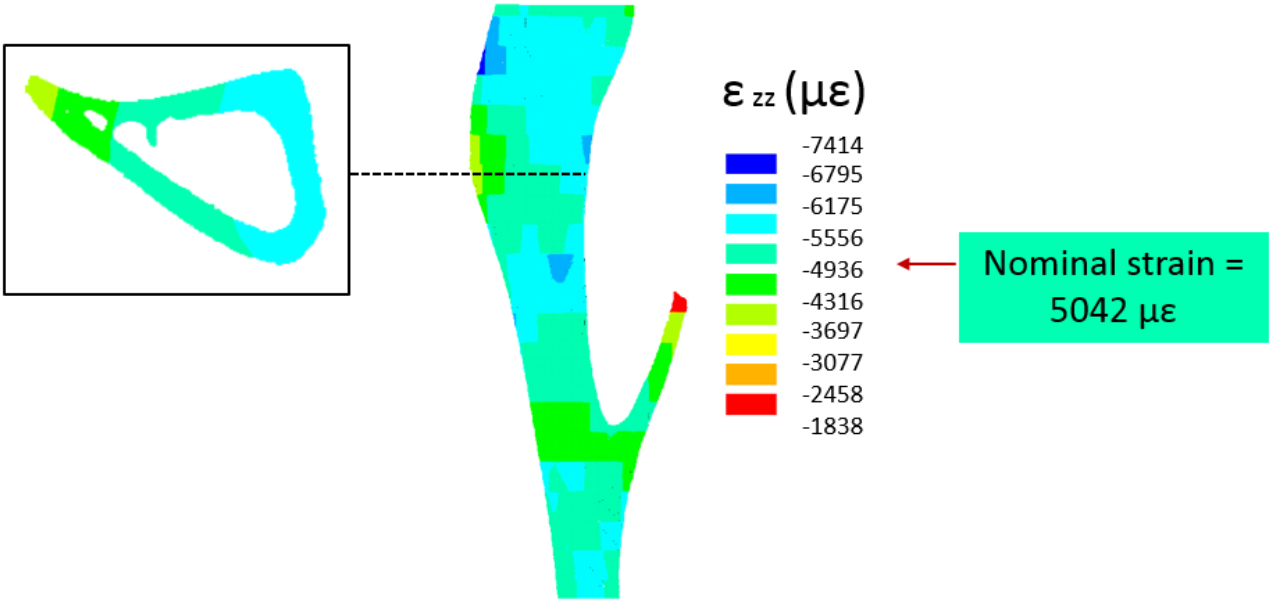

Figure 4.7. Spatial distribution of strains in the longitudinal direction (ε_{zz}) obtained by applying a virtual deformation on repeated scans of Sample2.

4.3.6 Validation of structural mechanical properties

Structural mechanical properties experimentally measured and predicted by microFE models are reported in Fig. 4.8. Every sample was predicted to fail in compression. The absolute errors were 14±11% for stiffness predictions and 9±9% for strength predictions.

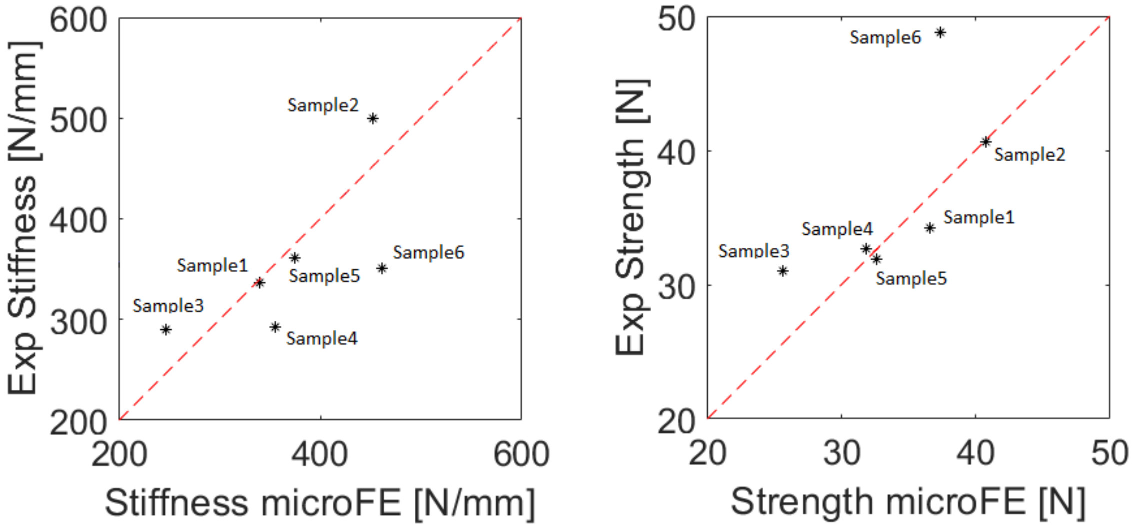

Figure 4.8. *Comparison between stiffness (left) and strength (right) measured experimentally and predicted by the microFE models in LoadStep2. The 1:1 relationship is plotted in red dashed line.*

4.3.7 Strain distribution

Histograms (frequency plots) and spatial distributions of strains obtained from microFE models for each load step are reported in Fig. 4.9 and Fig. 4.10 (for Sample2 and Sample3, for which the lowest and highest local strains were found respectively).

Strains were higher in compression compared to tension in all load steps (Fig. 4.9). The spatial distribution of strains over the tibia was similar for all samples, with peaks of compressive strains located at the distal extremity on the antero-medial surface and around the mid-diaphysis at the postero-lateral apex (Fig. 4.9). However, strain values varied among the samples. In LoadStep2 (representative of the typical load applied during *in vivo* loading of the mouse tibia (De Souza et al., 2005)), the peak corresponding to the high strains in the histograms (Fig. 4.9) varied from -2330 με to -4825 με among samples. In LoadStep3, some nodes exhibited strain values above the considered yield strain (-10300 με in compression (Bayraktar et al., 2004)). In Sample1, 4, 5 and 6 the portion of nodes overcoming the yield strain was less than 1%, while for Sample3 (Fig. 4.9) it was 2.6% of the total. No strains above the yield value were observed in Sample2 (Fig. 4.9).

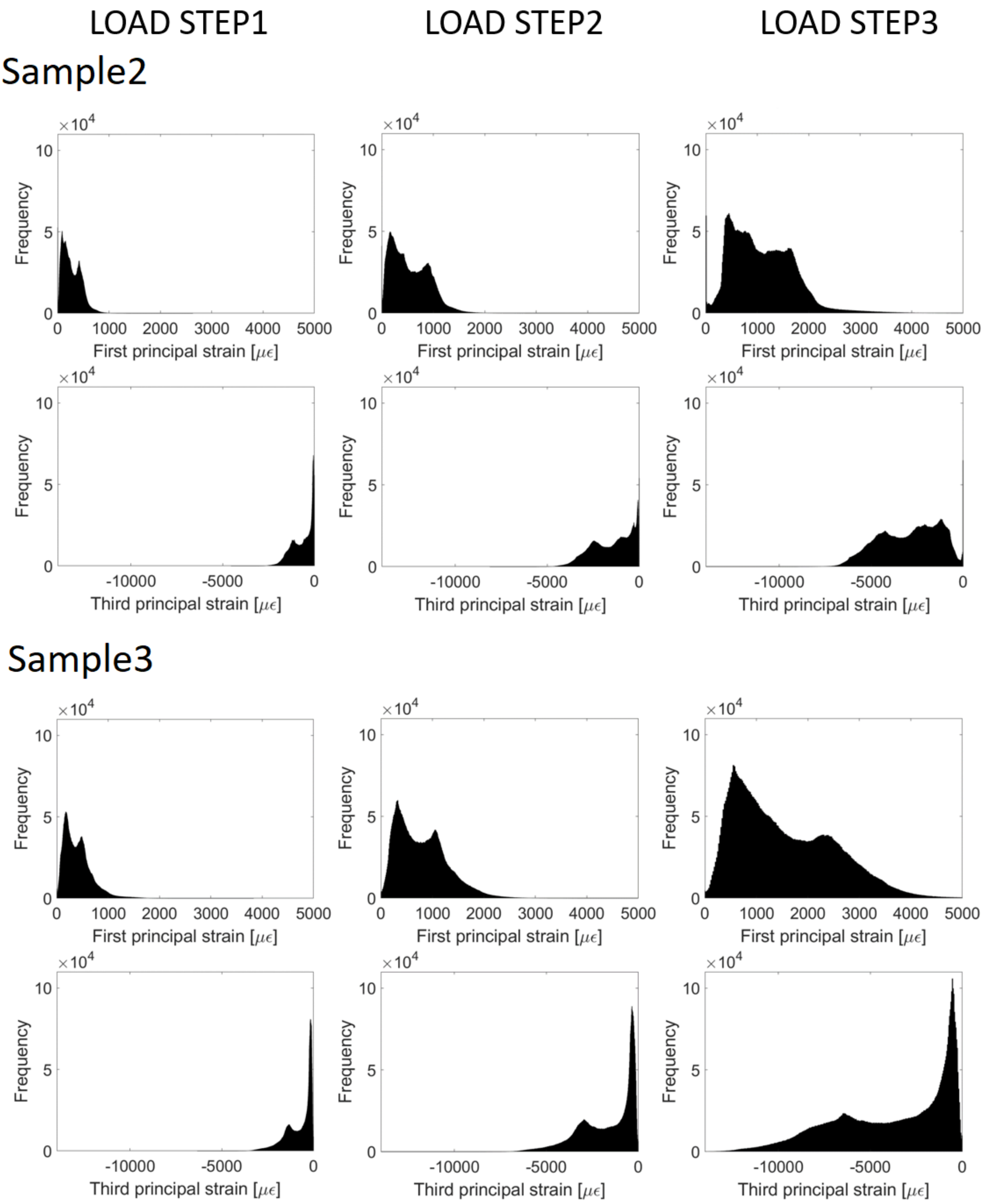

Figure 4.9. *Histograms of first and third principal strains obtained from microFE models of Sample2 and Sample3, which exhibited the lowest and highest local strains respectively.*

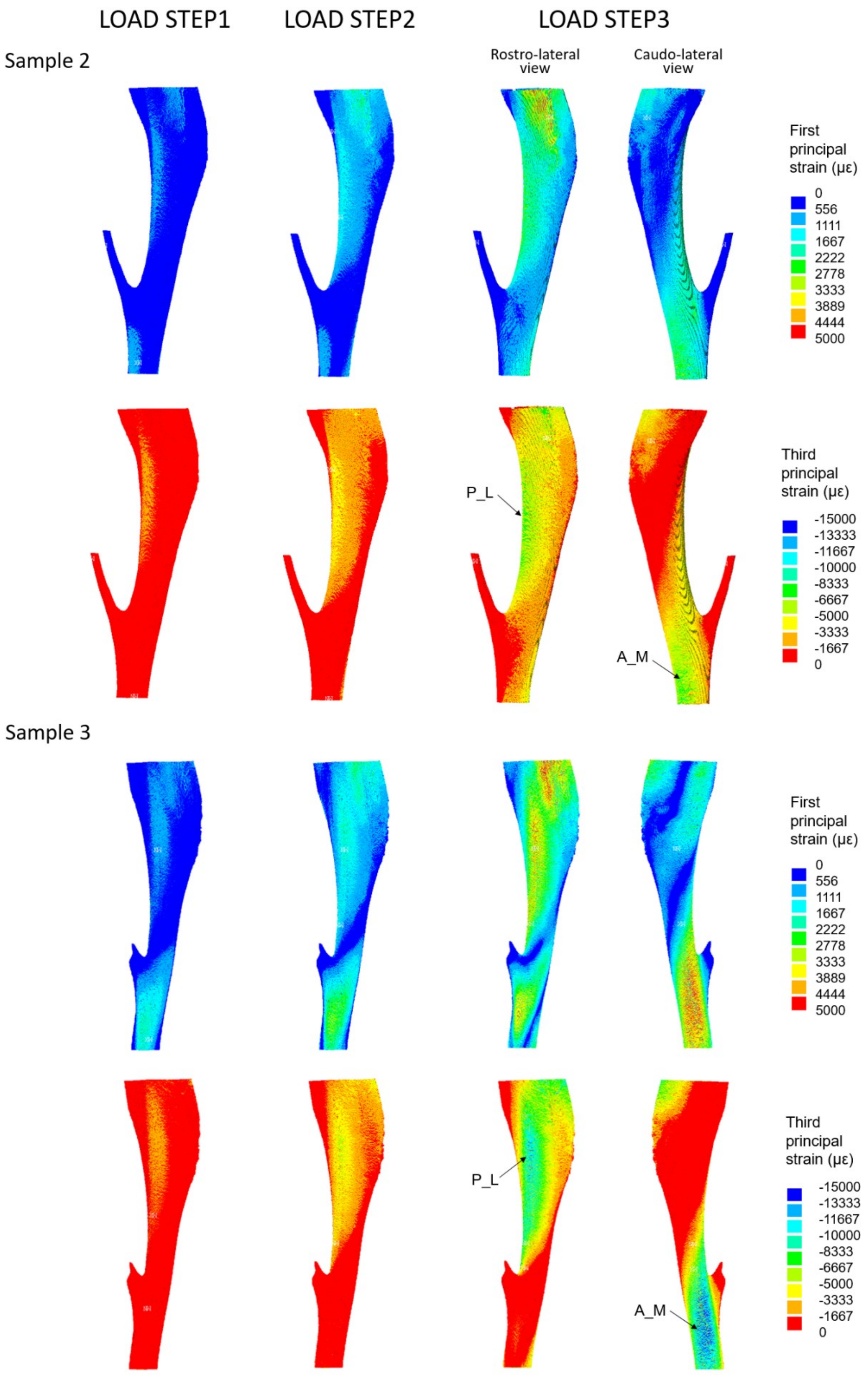

Figure 4.10. *Spatial distribution of first and third principal strains for Sample2 and Sample3. Peaks of compressive strains were located at the distal extremity on the antero-medial (A_M) surface and around the midshaft at the postero-lateral (P_L) apex.*

4.4 DISCUSSION

The goal of this study was to compare the local and structural mechanical properties predicted by microFE models in the mouse tibia under compression with experimental datasets, obtained using a combination of *in situ* mechanical testing, microCT imaging and the Digital Volume Correlation (DVC).

Apparent mechanical properties of the tibia estimated from microFE models were in good agreement with experimental measurements for stiffness (differences of 14±11%) and strength (9±9%), indicating that the failure criterion chosen in this study was adequate. This good agreement between experimental and predicted properties is fundamental for the credibility of the models that are used for estimating the effect of diseases and interventions *in vivo* (Lu et al., 2017).

The microFE predictions of displacements were found to be highly correlated with the experimental measurements in magnitude ($R^2 > 0.82$), while higher variability and errors were found in the Cartesian components. Correlations between the predicted and measured displacements in the longitudinal direction were fair to optimal ($R^2 = 0.69\text{-}0.92$). Nevertheless, the microFE models tended to overestimate local displacements in the loading direction, especially for larger absolute displacements. Similarly to previous studies (Chen et al., 2017, Costa et al., 2017, Zauel et al., 2005), errors were smaller in the loading direction compared to the transverse ones. No apparent effect of load levels was observed, with correlation parameters, slopes and percentage errors similar for all of them. By analyzing the spatial distribution of longitudinal displacements and errors, we observed that the microFE models predicted a more accentuated bending in the antero-posterior direction compared to the DVC measurements. The discrepancy in the mechanism of deformation was larger when displacements were not homogeneously distributed over the tibia (Fig. 4.6) and was probably the cause of the systematic errors found in the transverse direction Y (Fig. 4.5). This difference could potentially be due to residual errors in the registration of the microCT images, which can be affected by the geometry and features of the specimens. Since the mouse tibia is a slender bone and is characterized by a natural curvature, even a small mismatch between the experimental and microFE conditions could have an impact on the local predictions. The simplified models used in this study could also play a role. In particular, the assumptions about the material properties (homogeneous, isotropic and linear) affect the predictions of the local displacements under loading and the structural mechanical properties. The same microFE modelling approach has been previously validated for trabecular bone samples (Chen et al., 2017) and porcine vertebrae (Costa et al., 2017), showing that microFE models could predict more than 87% of the variation of the local displacements in both the longitudinal and transverse directions. The higher errors found for the mouse tibia are probably due to the different geometry and structure of the bone: the mouse tibia is mainly made of cortical bone, therefore the local material properties could be more relevant, compared to the previous cases (trabecular bone and porcine vertebrae), where the geometry and orientation of the trabeculae would probably play a major role. In particular, the higher errors found in the transverse directions compared to the longitudinal one suggest that local predictions could be improved by implementing anisotropic material properties in the models.

For Sample1 very low slope of the regression line and low correlation were found (slope=0.26, R^2=0.53) in LoadStep1, due to large differences between measured and predicted displacements in a subgroup of the investigated points (Fig. 4.11). The high errors were located at the anterior tibial ridge (Fig. 4.11), which may be related to the lower local accuracy of the DVC measurement (Paragraph 4.3.5). Additionally, the smaller deformations the tibia undergoes in LoadStep1 could potentially be harder to detect with the DVC algorithm. In fact, in LoadStep3 errors at the same comparison points were lower (24% in

LS3 compared to 70% in LS1).

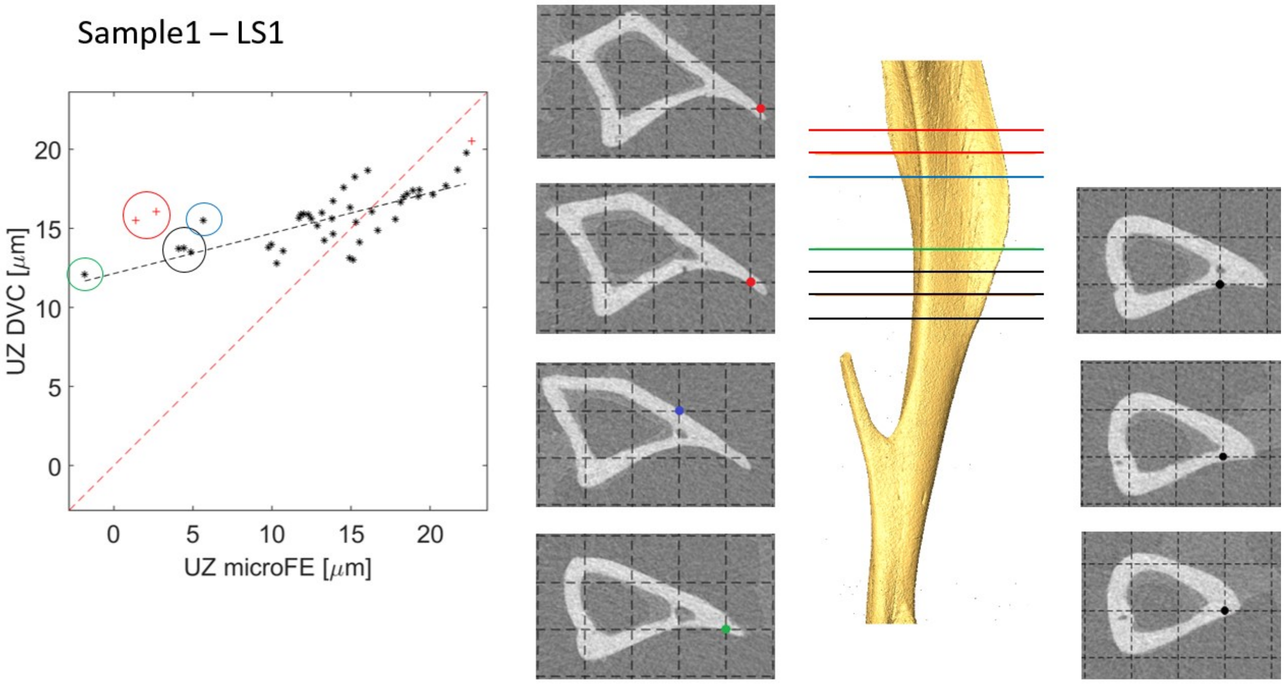

Figure 4.11. *Spatial location of the comparison points characterized by highest errors in the longitudinal displacement prediction (Sample1, LoadStep1, Z direction). Outliers are reported as red crosses.*

Overall, considering the good agreement between the predictions of the models and the experimental measurements of displacements, the application of this approach to estimate local strains to predict bone remodeling (Birkhold et al., 2016, Schulte et al., 2013a) seems adequate. However, more complex modeling techniques could be explored in order to see if local peak errors could be removed.

Strain distributions obtained with microFE models showed high variability among samples, with peak strains ranging from -2330με to -4825με in LoadStep2, although the same nominal loading conditions were applied. Additionally, the peak compressive strains were not consistently located in the same region for all tibiae, but were either around the mid-diaphysis at the postero-lateral apex or at the distal extremity on the antero-medial surface (Fig. 4.10). This variation highlights the importance of taking into account the realistic loading conditions applied on the sample experimentally.

The load applied during *in vivo* loading of the mouse tibia is normally selected by targeting a peak tensile strain of 1200–1500 με at the midshaft on antero-medial surface, which results in peak strains of -2300 με to -3000 με in compression (Birkhold et al., 2016, Patel et al., 2014). For studies performed on mice of the same strain (age range of 10–78 weeks) axial loads applied to the tibia to induce such local strain levels were 9–13 N in compression (Birkhold et al., 2016, De Souza et al., 2005, Patel et al., 2014). Even if similar axial loads were used in these studies, it should be noticed that the loading condition applied to the tibia is different in the two cases: axial load on the dissected tibia versus more complex loading scenario for *in vivo* loading, where fibula and soft tissues are intact. Also, a dehydration and rehydration procedure was performed on the tibiae in this study, in order to embed the extremities in resin and align the sample to the loading device. This could affect the material properties of the bone. Therefore, the strain distributions obtained in this study may be different from those experienced by the bone *in vivo*. Nevertheless, our results highlight the importance of taking into account the realistic loading conditions applied on the tibia during loading, which would probably differ from the nominal ones.

The main limitation of this work is that the complex validation method limited its applicability to a small sample size (N=6). However, bones from mice of different ages and interventions were included in order to test the model in different conditions. It should be noticed that all samples were from mice considered skeletally mature (age of 16–24 weeks), therefore potential differences are not expected to have a major impact on the validation study. Another limitation is that in this study simple (but efficient) homogeneous isotropic linear elastic voxel-based microFE models were used. Further improvements of the models are currently under exploration: implementing heterogeneous material properties based on local mineralisation could improve the predictions of structural properties and anisotropic material properties could improve local predictions in the transverse directions. Also, the boundary recovery can be improved by using tetrahedral meshes, while the failure criterion can be improved by adding material non-linearities. While these improvements may lead to a reduction of the peak errors, the application of the simple microFE models tested in this study showed acceptable errors for most applications. Lastly, the validation of the microFE predictions was limited to displacements and not strains, due to the current limitations of microCT-based DVC measurements. In a recent work (Palanca et al., 2017) it has been shown that the precision of DVC strain measurements becomes acceptable for a spatial resolution of 120 μm (within the mouse cortical bone) if the method is based on Synchrotron Radiation microCT images. However, the combination of DVC and Synchrotron Radiation tomograms is intrinsically limited, since the high radiation would potentially damage the organic phase of the bone.

In conclusion, a procedure to validate microFE predictions of local internal displacements and structural mechanical properties of the mouse tibia under compression has been developed and applied by combining *in situ* mechanical testing, microCT imaging and DVC analyses. An overall good agreement was found between the numerical predictions and experimental measurements, highlighting the potential of the method to provide non-invasive estimation of mechanical properties for preclinical assessment of bone health.

CHAPTER 5

EFFECT OF REPEATED *IN VIVO* MICRO-CT SCANNING ON THE MORPHOMETRIC, DENSITOMETRIC AND MECHANICAL PROPERTIES OF THE MOUSE TIBIA

This study was performed in collaboration with Dr Mario Giorgi who provided the images obtained from the *in vivo* experiments.

SUMMARY

In longitudinal studies, micro-Computed Tomography (microCT) imaging can be used to investigate bone changes over time due to interventions or treatments. However, ionising radiation exposure can provoke significant variations in bone morphometric parameters. In Chapter 3, the effect of reducing the integration time has been evaluated on the image-based measurements of morphometric, densitometric and mechanical properties of the tibia, in order to find the best compromise between image quality and radiation dose induced on the subject. In this work, the effect of repeated *in vivo* scans has been evaluated on the mouse tibia using the procedure defined previously. The right tibia of 12 female C57BL/6 (six wild type, WT, and six which underwent ovariectomy, OVX) and 12 BalbC (six WT and six OVX) mice was scanned *in vivo* using the microCT scanning procedure defined in Chapter 3. Each right tibia was scanned every two weeks starting at week 14 of age while the left tibia was used as non-irradiated control. At week 24, mice were sacrificed and both tibiae were scanned. Standard trabecular and cortical morphometric parameters were calculated from each image. The spatial distribution of bone mineral content (BMC) was obtained by dividing the tibia in 40 partitions. Structural mechanical properties in compression (stiffness and strength) were estimated by converting microCT images into voxel-based homogeneous linear elastic microFE models. Differences between left and right tibiae were evaluated for each parameter. In C57BL/6 wild type mice, radiation had a statistically significant but small effect on trabecular thickness (difference of 2±5%, equivalent to 1±3 μm and 0.1±0.3 voxels), while no effect was observed on the other parameters. In the other groups, no significant differences were found. No interaction between radiation and OVX surgery was observed. In conclusion, the repeated microCT scans have no significant or minimal influence on the properties of the mouse tibia. Therefore, the selected scanning protocol is acceptable for *in vivo* application for measuring the effect of bone interventions.

5.1 INTRODUCTION

Micro-Computed Tomography (microCT) imaging is considered the gold standard for *in vivo* bone imaging (Bouxsein et al., 2010) and has been used in many studies to evaluate the effect of aging (Buie et al., 2008, Main et al., 2010), drug treatments (Campbell et al., 2014, Lu et al., 2017) and mechanical loading (Birkhold et al., 2015, Holguin et al., 2014). However, in previous studies a significant effect of radiation on trabecular or cortical morphometric parameters has been observed (Klinck et al., 2008, Willie et al., 2013). In particular, the largest differences between irradiated and non-irradiated bones have been observed for trabecular bone volume fraction (up to -38%) and trabecular separation (up to +39%, Klinck et al., 2008, Willie et al., 2013). As these differences may affect the analyses of the effect of interventions on bone through *in vivo* microCT imaging, there is a need to define a scanning procedure which minimises the radiation effects for accurately estimating the parameters of interest. In Chapter 3, the accuracy of image-based measurements has been analysed on the mouse tibia using four different scanning procedures, characterized by decreasing integration time and, therefore, by decreasing nominal radiation dose. The results suggested that the IT100 scanning procedure (integration time equal to 100 ms, nominal radiation dose of 256 mGy) could be used for the subsequent analyses instead of the IT200 scanning procedure (integration time equal to 200 ms, nominal radiation dose of 513 mGy), that was previously used in our laboratory (Lu et al., 2017). Using the IT200 scanning procedure, the following significant effects of radiation were found: reduced trabecular bone volume fraction (-29%) in C57BL/6 mice which underwent ovariectomy (OVX) and in sham-operated mice (-33%), increased cortical thickness (+5%) in wild type mice (Lu et al., 2017, unpublished data). Additionally, microCT-based microFE models obtained using the same scanning procedure can predict accurately the structural properties and the local displacements in the tibia under loading (Chapter 4). This is important to estimate the local mechanical stimuli induced on the bone by an external load, which are linked to the local bone apposition and resorption (Birkhold et al., 2016, Schulte et al., 2013b). Nevertheless, it is still unknown if the new scanning procedure applied every two weeks *in vivo* would affect significantly the cell activity and induce variations in the bone structure, density or mechanical properties of the mouse tibia.

The goal of this study was to evaluate the effect of repeated *in vivo* microCT scanning of the mouse tibia on its morphometric, densitometric and mechanical properties, using the procedure at reduced nominal radiation dose defined in the previous chapters.

5.2 MATERIALS AND METHODS

The microCT images used in this chapter to evaluate the effect of radiation exposure were collected by Dr Mario Giorgi, who performed the longitudinal study on mice in the framework of the MultiSim project (EPSRC, Grant number: EP/K03877X/1). Dr Mario Giorgi performed all microCT scans and the rigid registration of the images, as described in Paragraphs 5.2.1 and 5.2.2. The aligned images were subsequently post-processed in order to obtain the parameters of interest (Paragraphs 5.2.3 – 5.2.5). Lastly, the irradiated tibia was compared to the non-irradiated one to evaluate potential radiation effects (Paragraph 5.2.6).

5.2.1 Animal study

Twelve female C57BL/6 (B6) and twelve Balb/C (BAL) female mice were purchased from Envigo and housed at the Biological Services Unit of the University of Sheffield with a twelve-hour light/dark cycle at 22°C and *ad libitum* access to food and water. Six mice per strain underwent the ovariectomy (OVX) surgery at the age of 14 weeks. The right tibia of each mouse was scanned *in vivo* every two weeks from week 14 to 24 of age (Fig. 5.1) using the protocol defined in Chapter 3 (VivaCT 80, Scanco Medical, Bruettisellen, Switzerland; 55 kVp, 145 μA, 10.4 μm voxel size, 100 ms integration time, 32 mm field of view, 750 projections/180°, no frame averaging, 0.5 mm Al filter). At week 24 of age, mice were sacrificed and both tibiae were scanned (Fig. 5.1). The left tibia was used as non-irradiated control. All procedures were approved by the local Research Ethics Committee of the University of Sheffield (Sheffield, UK). All images were reconstructed using the software provided by the manufacturer (Scanco Medical AG) and applying a beam hardening correction based on a phantom of 1200 mg HA/cc density, which has been shown to improve the local tissue mineralization measurement (Kazakia et al. 2008).

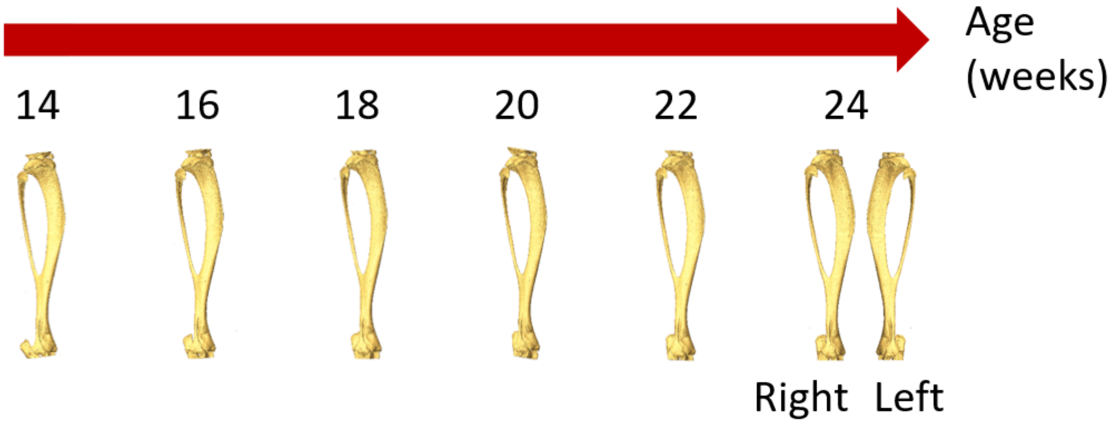

***Figure 5.1**. Schematic representation of the longitudinal scans of the mouse tibia. The right tibia was scanned in vivo every two weeks starting from the age of 14 until the age of 24 weeks. The left tibia was used as non-irradiated control. At the last time point, both right and left tibiae were scanned with the same protocol.*

5.2.2 Image processing

MicroCT images were used to estimate the following parameters of interest, as described in Chapter 3: standard trabecular and cortical morphometric parameters, spatial distribution of bone mineral content (BMC) and mechanical properties in compression estimated using microFE models (Fig. 3.2). The image processing methods are briefly summarized here.

In order to align all images in the same reference system, a rigid registration procedure was applied. One tibia from the C57BL/6 group and one from the BalbC group, scanned at week14, were rotated in Amira (Amira 6.0.0, FEI Visualization Sciences Group, France) in order to align their longitudinal axes to the *Z*-axis of a global reference system (Lu et al., 2017). Afterwards, the images acquired at subsequent time points and from different mice were rigidly registered to the aligned ones. Left tibiae were horizontally flipped to perform the registration to the right ones. Normalized Mutual Information was used as optimization criterion and Lanczos interpolator was used for resampling the images (Birkhold et al., 2014, Meijering, 2000). A Gaussian filter (kernel 3x3x3, standard deviation 0.65) was applied to reduce the high frequency noise (Bouxsein et al., 2010).

5.2.3 Standard Morphometric Analysis

Morphometric analyses (Paragraph 3.2.4) were performed using CTAn (Bruker, Belgium). For trabecular measurements, a VOI of 1 mm was selected below the growth plate with an offset of 0.2 mm from a reference slice, identified as the point where the medial and lateral sides of the growth plate merged. Trabecular bone was contoured by manually drawing 2D regions of interest (ROIs) every five slices and segmented by using a single level threshold (average of the grey levels corresponding to the bone and background peaks in the image histogram (Chen et al., 2017, Christiansen, 2016)). A despeckling filter was applied to remove 3D white (bone) regions less than 10 voxels in volume. Trabecular bone volume fraction (Tb.BV/TV), thickness (Tb.Th), separation (Tb.Sp) and number (Tb.N) were computed for each VOI (Bouxsein et al., 2010).

For cortical analysis, a VOI of 1 mm was selected, centred at the tibial midshaft. After segmentation, pores within the cortex were removed by applying a closing function (2D round kernel, radius equal to 10 pixels). Total cross-sectional area (Tt.Ar), cortical bone area (Ct.Ar), cortical area fraction (Ct.Ar/Tt.Ar) and cortical thickness (Ct.Th) were computed for each VOI (Bouxsein et al., 2010).

5.2.4 Spatial Distribution of bone mineral content (BMC)

The procedure for evaluating the spatial distribution of BMC over the tibia has been described in Paragraph 3.2.6. Briefly, the registered greyscale images were converted into tissue mineral density (TMD) images by using the calibration curve provided by the manufacturer of the *in vivo* scanner. BMC in each voxel was then calculated as its TMD multiplied by the volume of the voxel. A VOI was defined below the growth plate, starting from the slice where the growth plate tissue was not visible anymore. The VOI included the 80% of the total length and excluded the fibula (Figure 3.2b). Afterwards, the VOI was divided into ten longitudinal sections and in four quadrants (anterior, posterior, lateral and medial). For each partition, BMC was calculated as the sum of BMC in each voxel classified as bone.

5.2.5 Micro-Finite Element (microFE) Models

Hexahedral homogeneous linear elastic microFE models were generated for each tibia (Paragraph 3.2.7). Young's Modulus of 14.8 GPa and Poisson's ratio of 0.3 were assigned (Webster et al., 2008).

In order to evaluate the stiffness of the bone, the proximal end of the tibia was fully constrained, while a displacement equal to 1 mm was applied on each node of the distal surface in the longitudinal direction. The apparent stiffness was calculated as the sum of reaction forces at the proximal surface, divided by the applied displacement.

For strength estimation, the proximal surface of the tibia was fully constrained, while 1 N load was applied on the distal surface, equally distributed on each node. Strength was calculated by assuming that tibia fails when 2% of the nodes reach a critical strain level (adapted from (Pistoia et al., 2002)) of either -10300 $\mu\varepsilon$ in compression or 8000 $\mu\varepsilon$ in tension (Bayraktar et al., 2004).

5.2.6 Statistical analysis

In Fig. 5.2-5.5, the boxplots (boxplot function, Matlab) represent the distributions of each parameter values for each of the analysed groups. The median of the distribution is reported in a red line, while the edges of the box represent the 25th and 75th percentiles. Black lines extend to the most extreme values not considered as outliers, while outliers are reported in red crosses. Lastly, numbers indicate individual mice in each group.

The effect of radiation exposure was evaluated by comparing each of the bone parameters obtained for the right irradiated limb to those obtained for the left non-irradiated one. In all following paragraphs and tables, percentage differences between left and right tibiae are reported as median ± standard deviation (SD). Significant differences were investigated using Wilcoxon signed-rank tests (ranksum function, Matlab, 5% significance level), since the distributions for each group did not meet the assumption of normality (Kolmogorov-Smirnov test, kstest function, Matlab, $p < 0.05$).

Potential interactions between factors (radiation, mouse strain and OVX surgery) were investigated by pooling data from different groups and using two-way ANOVA tests (SPSS). The assumption of normality was met for all variables (Kolmogorov-Smirnov test, SPSS, $p > 0.05$) except cortical area fraction and cortical thickness, therefore the results for these two variables should be interpreted with care. The assumption of homoscedasticity was met for all variables (Levene's test, SPSS, $p > 0.05$).

5.3 RESULTS

In Fig. 5.2-5.5, comparisons between the irradiated and non-irradiated tibiae are reported for the four groups analysed. In C57BL/6 wild type (B6-WT) mice, the exposure to ionising radiation provoked a small significant increase in trabecular thickness (difference of 2%±5%, Fig. 5.2), while no significant differences were observed for the other parameters. In the other groups, no significant differences were found for any of the parameters analysed. Some similar patterns were observed among the analysed groups, even if the effect of radiation was not significant. Trabecular bone volume fraction (Tb.BV/TV) tended to decrease in the irradiated limb. Variations observed were larger for the B6-WT (6.6±0.7% for irradiated vs

7.9±1.3% for non-irradiated) and the B6-OVX group (4.2±0.5% for irradiated vs 5.8±0.9% for non-irradiated) compared to the BAL-WT (10.1±1.3% for irradiated vs 10.4±2.4% for non-irradiated) and the BAL-OVX (7.5±0.6% for irradiated vs 7.8±1.6% for non-irradiated) groups. Similarly, trabecular separation (Tb.Sp) tended to increase in all groups (+11%±14% for B6-WT, +6%±8% for BAL-WT, +9%±11% for B6-OVX and +10%±14% for BAL-OVX), which corresponded to median variations of 21-35 μm. Trabecular number (Tb.N) tended to decrease (-15%±12% for B6-WT, -17%±15% for BAL-WT, -24%±10% for B6-OVX and -6%±7% for BAL-OVX) in all groups. Small variations were observed in cortical parameters for the B6-WT and BAL-WT groups (less than 5% for all parameters). Total cortical area (Tt.Ar) showed a small decrease for some groups (-6%±5% for the B6-OVX and -5%±5% for the BAL-OVX) in the irradiated limb compared to the non-irradiated one, as well as cortical area (Ct.Ar) (-4%±6% for B6-OVX and -3%±4% for BAL-OVX).

No significant differences between the right and left tibiae were found for total BMC (including both cortical and trabecular bone) and for local BMC in the 40 partitions analysed. Variations in total BMC were +1%±4% for B6-WT mice, -1%±7% for B6-OVX, +2%±3% for BAL-WT and -2%±2% for BAL-OVX mice. Percentage variations in local BMC in the 40 partitions are reported in Table 5.1. The BMC of the lateral partitions tended to be lower in the irradiated tibiae compared to non-irradiated ones, with larger differences in the proximal part. No systematic patterns were observed among the different groups for the other partitions.

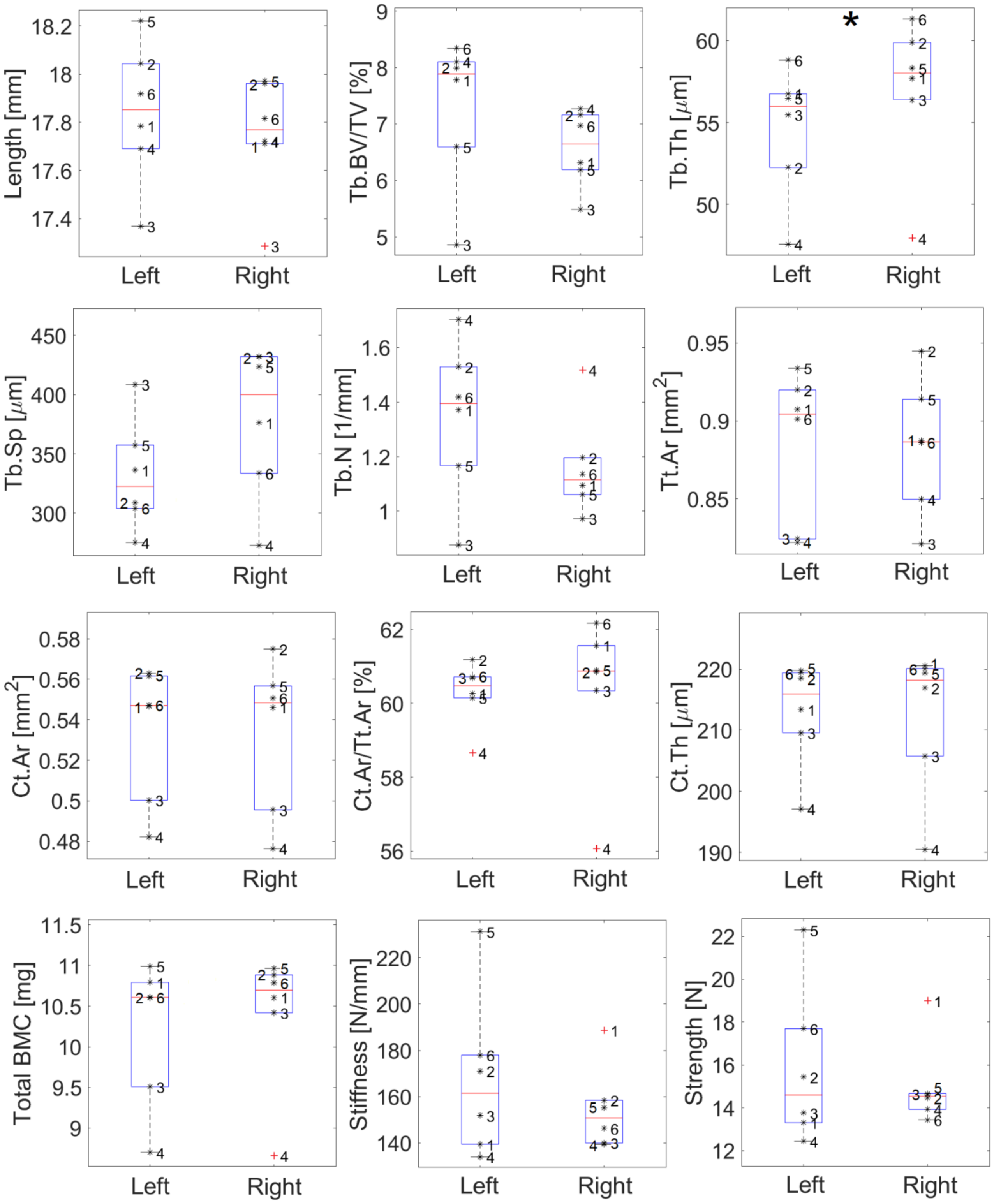

Figure 5.2. *Effect of radiation in C57BL/6 wild type mice (left = non-radiated, right = radiated). Parameters reported: length, trabecular parameters: bone volume fraction (Tb.BV/TV), thickness (Tb.Th), separation (Tb.Sp), number (Tb.N), cortical parameters: total area (Tt.Ar), cortical area (Ct.Ar), area fraction (Ct.Ar/Tt.Ar), thickness (Ct.Th), total bone mineral content (BMC), stiffness and strength estimated from microFE models. Red crosses represent outliers. Numbers refer to the mouse numbers. "*" indicates statistically significant difference.*

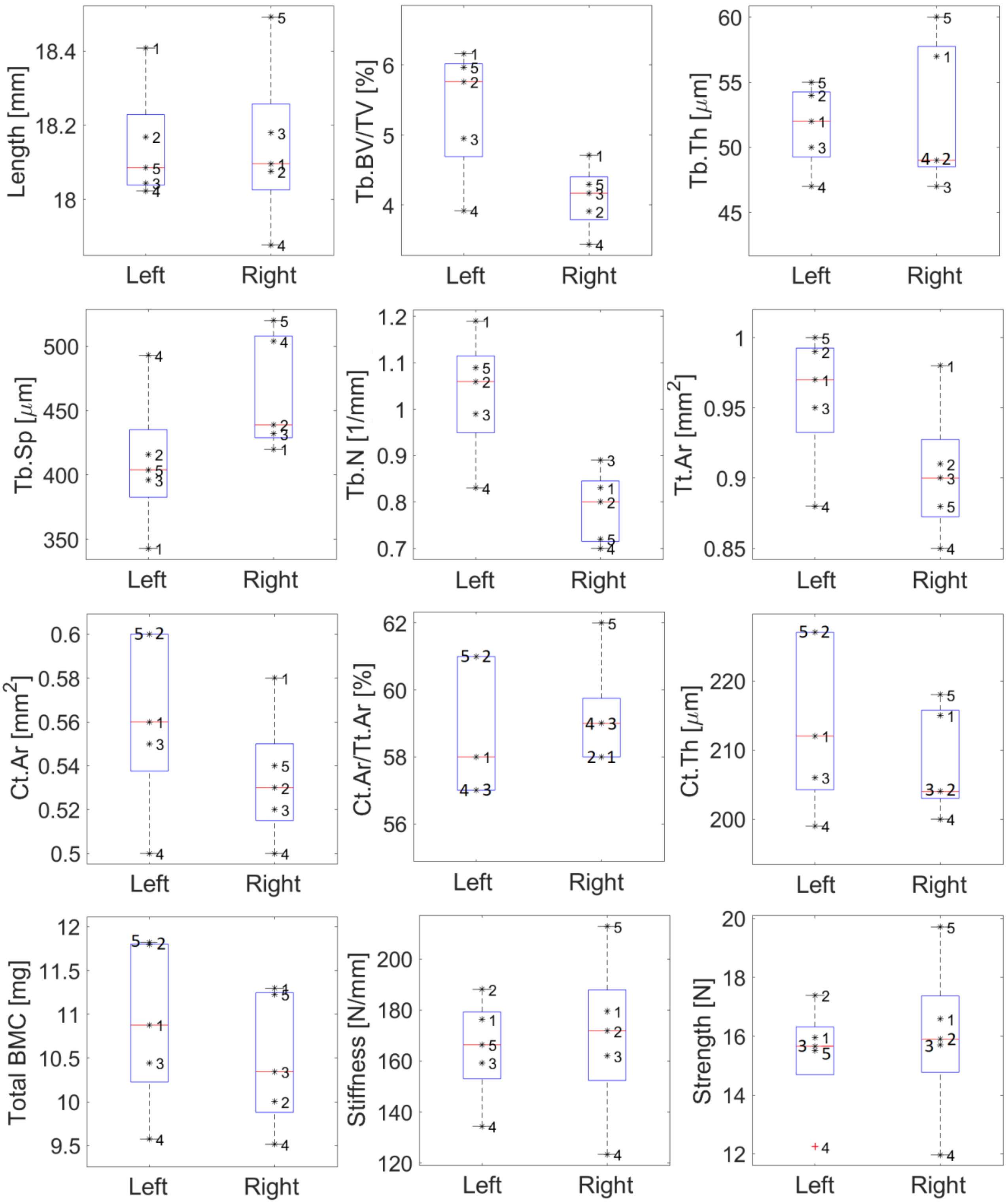

***Figure 5.3**. Effect of radiation in C57BL/6 OVX mice (left = non-radiated, right = radiated). Parameters reported: length, trabecular parameters: bone volume fraction (Tb.BV/TV), thickness (Tb.Th), separation (Tb.Sp), number (Tb.N), cortical parameters: total area (Tt.Ar), cortical area (Ct.Ar), area fraction (Ct.Ar/Tt.Ar), thickness (Ct.Th), total bone mineral content (BMC), stiffness and strength estimated from microFE models. Red crosses represent outliers. Numbers refer to the mouse numbers.*

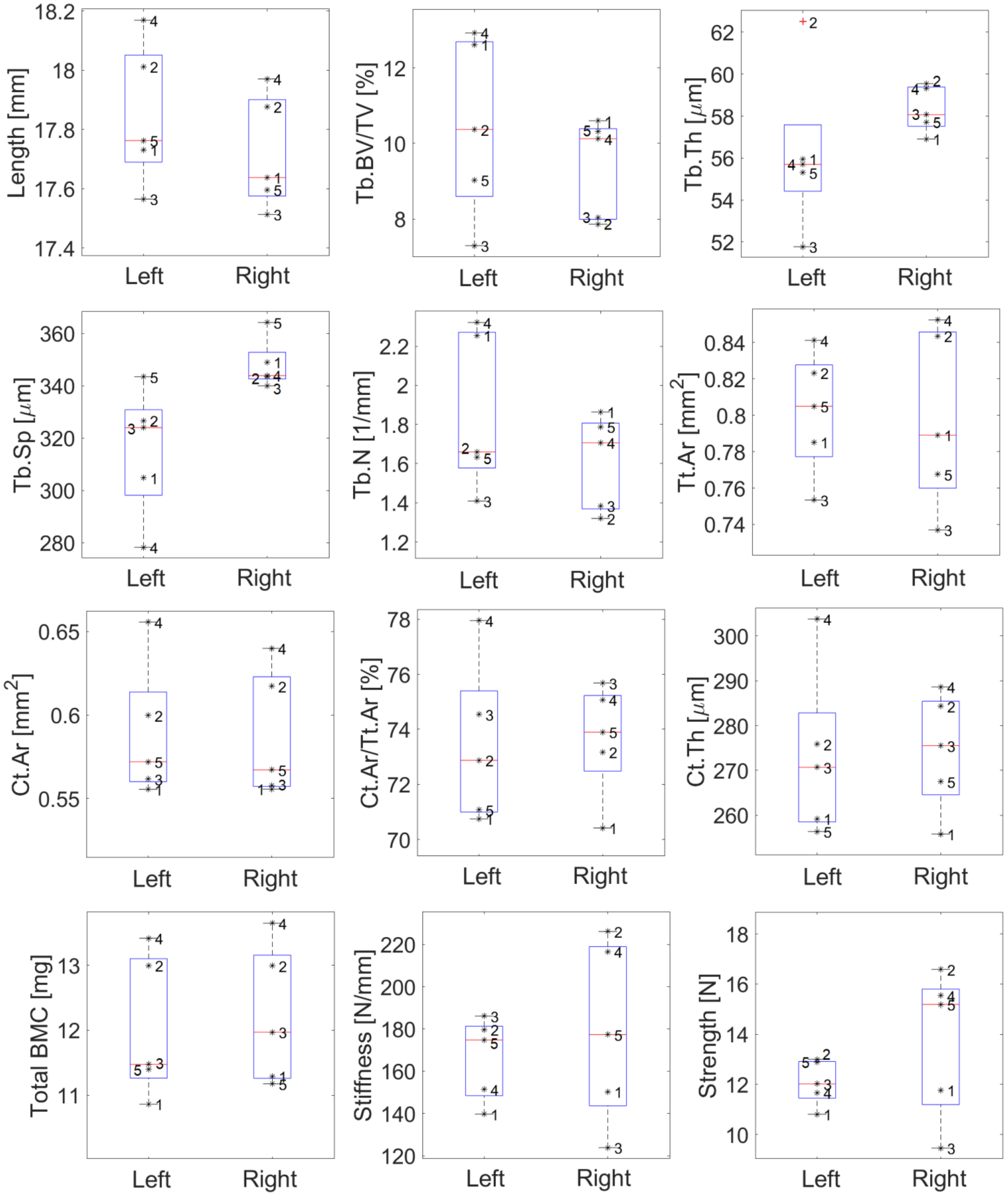

Figure 5.4. *Effect of radiation in BalbC wild type mice (left = non-radiated, right = radiated). Parameters reported: length, trabecular parameters: bone volume fraction (Tb.BV/TV), thickness (Tb.Th), separation (Tb.Sp), number (Tb.N), cortical parameters: total area (Tt.Ar), cortical area (Ct.Ar), area fraction (Ct.Ar/Tt.Ar), thickness (Ct.Th), total bone mineral content (BMC), stiffness and strength estimated from microFE models. Red crosses represent outliers. Numbers refer to the mouse numbers.*

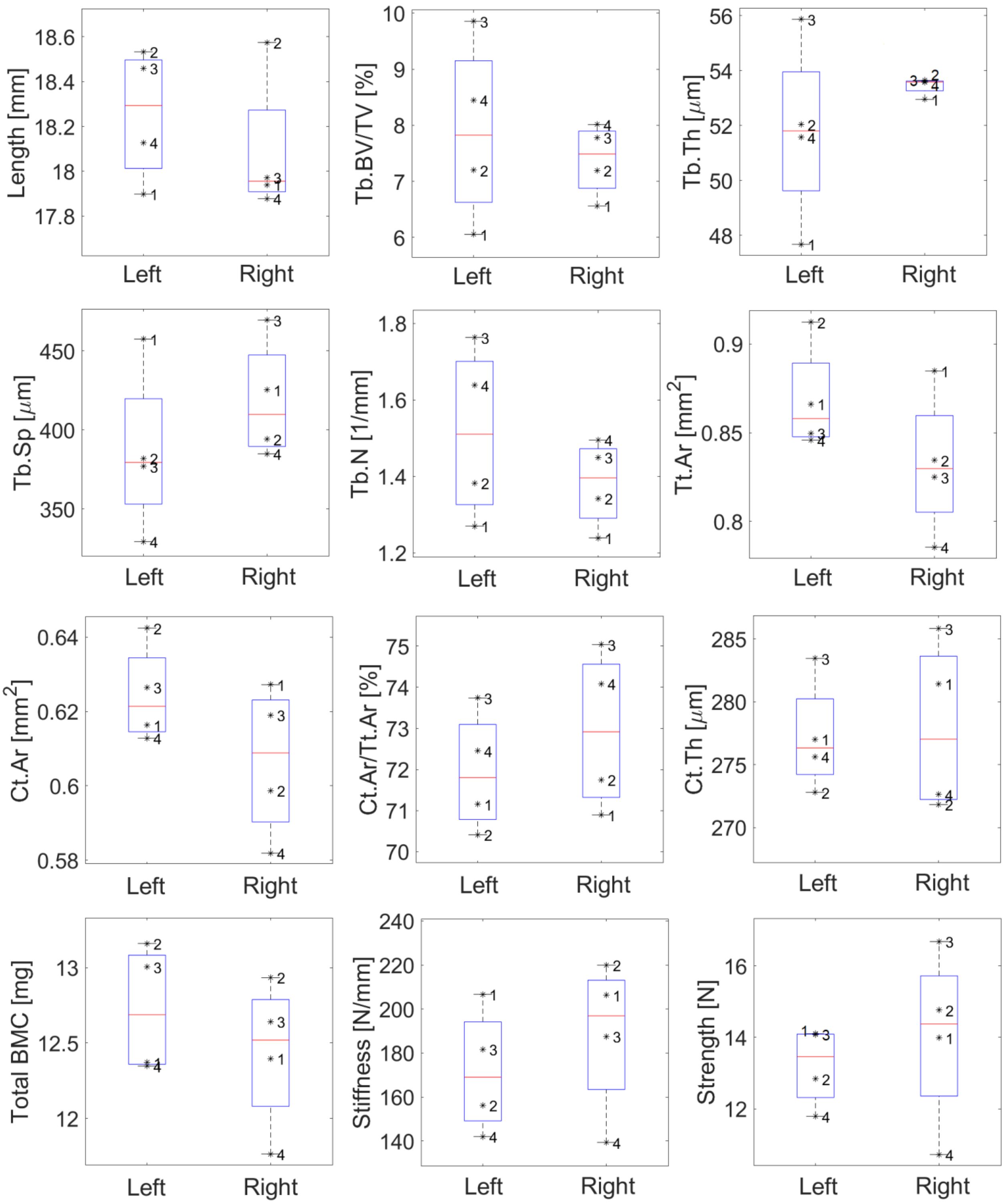

***Figure 5.5**. Effect of radiation in BalbC OVX mice (left = non-radiated, right = radiated). Parameters reported: length, trabecular parameters: bone volume fraction (Tb.BV/TV), thickness (Tb.Th), separation (Tb.Sp), number (Tb.N), cortical parameters: total area (Tt.Ar), cortical area (Ct.Ar), area fraction (Ct.Ar/Tt.Ar), thickness (Ct.Th), total bone mineral content (BMC), stiffness and strength estimated from microFE models. Numbers refer to the mouse numbers.*

B6-WT

	L	A	M	P
01	1±15	3±16	0±33	3±5
02	-3±13	1±12	1±18	5±9
03	1±13	2±9	5±19	0±6
04	2±13	3±8	9±14	-1±6
05	1±11	-3±8	1±6	3±12
06	-3±9	2±5	-1±3	1±8
07	-5±12	3±2	-4±8	0±6
08	-2±7	2±3	-2±5	-3±7
09	-3±10	0±6	-1±3	1±5
10	2±13	2±4	2±7	2±13

B6-OVX

	L	A	M	P
01	-4±10	3±15	-1±19	-9±19
02	-13±11	-3±10	4±10	-5±15
03	-7±11	-3±10	6±14	3±11
04	-2±9	-8±10	4±9	-2±9
05	-2±7	-2±9	-1±7	3±17
06	-3±9	2±8	-8±7	0±10
07	-6±5	0±8	-9±11	1±14
08	-3±7	3±10	-12±10	-1±13
09	-2±7	-1±5	-10±6	-2±8
10	1±15	-2±7	-4±11	4±9

BAL-WT

	L	A	M	P
01	-8±10	5±7	14±17	6±14
02	-5±11	5±4	8±19	7±9
03	-9±11	6±3	5±4	3±5
04	-15±11	10±5	9±7	5±5
05	-6±8	6±5	2±5	3±2
06	-6±8	5±3	-1±4	3±2
07	-5±8	1±3	-4±7	3±5
08	-3±6	4±3	-6±6	6±6
09	1±7	6±6	4±5	6±5
10	1±10	5±7	4±7	9±5

BAL-OVX

	L	A	M	P
01	-20±11	1±8	-11±16	1±9
02	-17±20	3±6	-10±9	6±9
03	-10±22	1±3	3±6	4±7
04	-17±17	3±4	2±4	6±6
05	-17±12	3±6	-1±4	4±6
06	-12±7	4±5	-7±1	5±6
07	-9±5	-1±6	-14±5	-6±10
08	-7±3	8±3	-7±4	13±5
09	-3±3	7±4	-5±5	7±3
10	-11±7	7±12	0±11	14±6

***Table 5.1**. Differences of local total BMC (both trabecular and cortical bone) between right (irradiated) and left (control) tibiae for C57BL/6 (B6) and BalbC (BAL) mice (WT = wild type, OVX = ovariectomised mice). Percentage differences (median ± SD) between the right and left tibiae are reported for the ten longitudinal sections (01 = most proximal, 10 = most distal) and four quadrants (L = lateral, A = anterior, M = medial, P = posterior). Variations were not significant for any group.*

The largest variations were not located in the same region among different groups of mice. In B6-WT mice, the largest variation was observed in the medial partition close to the midshaft (M-04, +9%±14%). In the B6-OVX group, a variation of -13%±11% was observed in the lateral sector at the proximal side (L-02). In BAL-WT mice, the largest variation was observed in the lateral partition close to the midshaft (L-04, -15%±11%). Lastly, in BAL-OVX mice, the largest difference was located in the most proximal lateral partition (L-01, -20%±11%).

In Fig. 5.6, the relationship between total BMC and mechanical properties is reported for each tibia. Stiffness was positively but weakly correlated to total BMC ($R^2 = 0.24$, $p = 0.001$). No correlation was found between strength and total BMC ($p = 0.89$), highlighting the benefit of FE modelling for evaluating the mechanical competence of the bone.

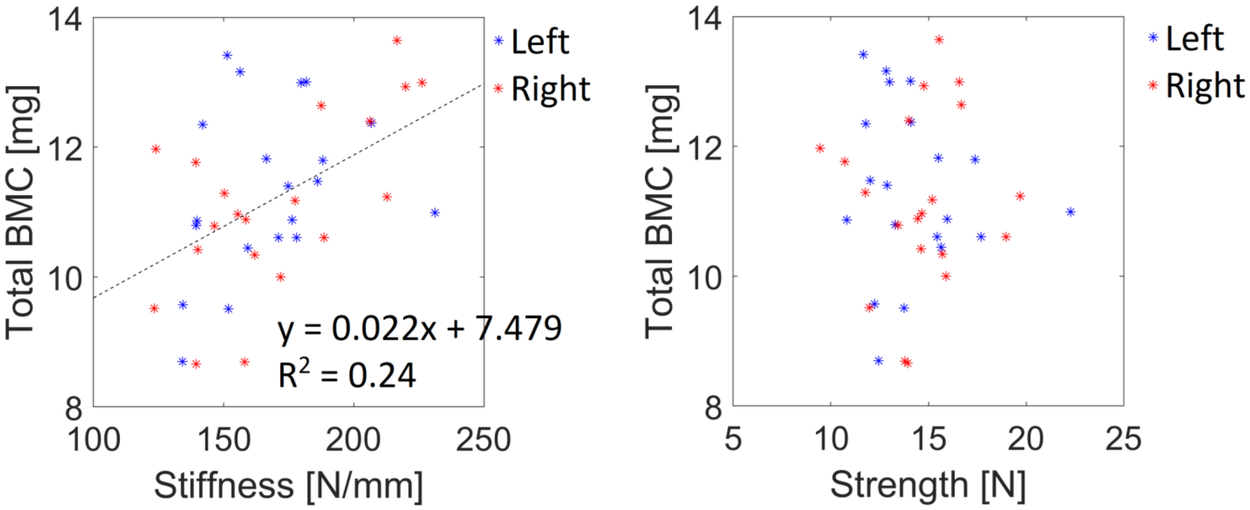

***Figure 5.6**. Relationship between total bone mineral content (BMC) and mechanical properties. A significant ($p=0.001$) but weak ($R^2=0.24$) correlation was found between total BMC and stiffness. No correlation was found between total BMC and strength.*

Differences in global stiffness between irradiated and non-irradiated bones estimated from microFE models were -8%±23% for B6-WT mice, 2%±15% for B6-OVX, +8%±29% for BAL-WT and +2%±20% for BAL-OVX mice. For strength, variations of 0%±28% in the B6-

WT group, 0%±14% for B6-OVX, +18%±21% for BAL-WT and +7%±13% for the BAL-OVX group were observed. Strain distributions were in most cases consistent between the right and left tibiae (Fig. 5.7 a-d), with peaks corresponding to similar strain levels. In some cases higher peak strains were observed in the left (5 out of 20) or in the right tibia (3 out of 20) compared to the contralateral one (Fig. 5.7 e-f). However, no consistent increase or decrease in local strains was observed in the irradiated tibia compared to the non-irradiated one.

The analysis of interactions between factors (radiation, mouse strain and OVX surgery), performed by pooling data from all groups, is reported in Table 5.2. It should be noticed that for two variables (cortical area fraction and cortical thickness) the assumption of normality was not met, therefore results should be interpreted with care for these two parameters. For Tt.Ar, a significant difference was found between the left and right leg ($p = 0.032$), however this was likely due to the significant interaction between the radiation and group factors ($p = 0.038$). For the other variables, no significant differences were found between the irradiated and non-irradiated leg, confirming the results obtained for the single groups. No interactions between radiation and OVX surgery were observed ($p > 0.05$). As expected, most variables were significantly different between the two mouse strains. Lastly, trabecular parameters and total cortical area were significantly different between wild type and OVX mice, confirming the effectiveness of the OVX intervention.

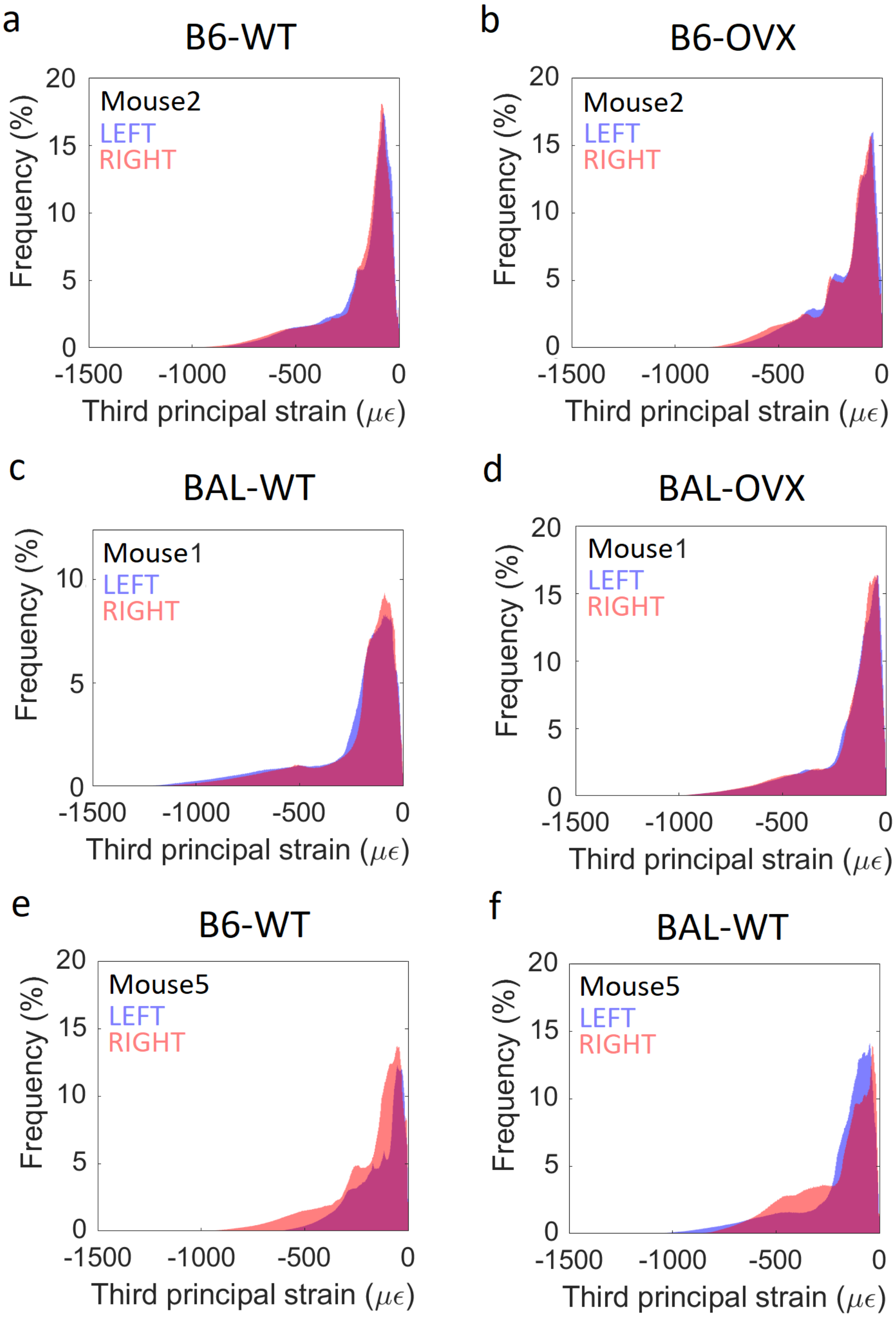

Figure 5.7. *Histograms of third principal strain in C57BL/6 (B6) and BalbC (BAL) mice (WT = wild type, OVX = ovariectomy). In a-d a representative mouse is reported for each of the four analysed groups. In e-f mice which showed the largest differences in local strains between the right and left tibia are reported.*

	Group	Strain	Side	Group*Strain	Group*Side	Strain*Side
Tt.Ar	**0.002**	<**0.001**	**0.032**	0.611	**0.038**	0.542
Ct.Ar	0.128	<**0.001**	0.182	0.366	0.158	0.594
Ct.Ar/Tt.Ar**	0.057	<**0.001**	0.529	0.934	0.529	0.745
Ct.Th**	0.869	<**0.001**	0.643	0.406	0.574	0.453
Tb.BV/TV	<**0.001**	<**0.001**	0.162	0.620	0.678	0.841
Tb.Th	**0.001**	0.140	0.313	0.887	0.387	0.531
Tb.Sp	**0.001**	0.239	0.068	0.907	0.728	0.950
Tb.N	**0.009**	<**0.001**	0.128	0.810	0.496	0.676
Total BMC	0.312	<**0.001**	0.457	0.579	0.171	0.568
Strength	0.664	**0.011**	0.589	0.634	0.982	0.318
Stiffness	0.557	0.183	0.663	0.864	0.648	0.291

***Table 5.2**. Results from two-way ANOVA tests obtained by pooling data from all groups. For each variable the effect of three factors is reported (group: wild type vs OVX, strain: C57BL/6 vs BalbC, side: left vs right), as well as interactions between factors (indicated by *). Significant differences or significant interactions ($p < 0.05$) are reported in bold. For two variables (indicated by **) the assumption of normality was not met, therefore results should be interpreted with care.*

5.4 DISCUSSION

In this chapter the effect of repeated *in vivo* microCT scans on the properties of the mouse tibia has been evaluated for two strains of mice (C57BL/6 and BalbC) and two groups (wild type, WT, and ovariectomised, OVX). For each mouse, the right tibia was scanned *in vivo* five times every two weeks, while the left tibia was used as non-irradiated control. The effect of radiation was evaluated on morphometric, densitometric and mechanical properties of the tibia, measured from microCT images.

For all mice minimal (2% increase in trabecular thickness for B6-WT mice) or no significant effect was observed for the morphometric trabecular or cortical parameters. No significant effect was found on the local BMC in the 40 partitions analysed. Differences in local bone mineral content (BMC) tended to be higher at the proximal extremity of the tibia, probably due to trends (but still not significant) in reduction of trabecular BV/TV and increase in

Tb.Sp for the irradiated tibia, especially for the BalbC group. For all groups, BMC in the lateral partitions tended to be reduced in the irradiated tibia. No consistent patterns were observed for the other partitions among the different groups. Mechanical properties did not consistently increase or decrease in the irradiated tibia compared to the non-irradiated one. These findings suggest that the used scanning procedure has minimal impact on the bone properties even after five scans, making it applicable for measuring the effect of interventions on bone remodelling. No significant interaction was found between radiation and OVX surgery, indicating that radiation effects are not influenced by the metabolic state of the bone, as reported in a previous study (Klinck et al., 2008).

When comparing these results to those reported in the literature, some similar trends can be identified, even though methodological differences exist among different studies, which are discussed later. As reported in Table 2.1, some previous studies (Klinck et al., 2008) reported that radiation (846 mGy/scan) provoked reductions in Tb.BV/TV (8-38%) and increases in Tb.Sp (14-39%), which were significant in most analysed groups. (Laperre et al., 2011) found non-significant reductions in Tb.BV/TV and Tb.N due to radiation at 434 mGy/scan radiation dose. Results from all studies suggest that radiation induces bone loss in the trabecular compartment, which seems to occur through loss of the thinner trabeculae, resulting in decreased Tb.BV/TV, increased Tb.Sp and similar or moderately increased Tb.Th. However, the effect of radiation can be reduced by tuning the scanning protocol, number and frequency of the scans. (Laperre et al., 2011) suggested that their scanning protocol (nominal radiation dose of 434 mGy/scan, 3 scans, every two weeks) is likely close to the limit of safely using for *in vivo* imaging. In fact, higher radiation doses (776-846 mGy/scan) and frequency (weekly scans) produced significant effects (Klinck et al., 2008). As expected, the number of scans seems to play a role too. In this study, a lower radiation dose (256 mGy/scan) but more scans (five scans, every two weeks) resulted in non-significant effects of radiation, with some trends for morphometric parameters in line with what reported in (Laperre et al., 2011). Lastly, the size of the scanned volume determines the total scanning time, therefore scanning the whole tibia requires an adaptation of the protocol, compared to those used for scanning the proximal tibia only. In general, each procedure needs to be tested in order to ensure that radiation effects are acceptable according to the final application. The scanning protocol defined in this study allows to scan the whole tibia at five time points with minimal radiation effects, thus providing comprehensive information about bone changes in both space and time.

Limited data is reported in literature regarding the effect of radiation on densitometric and mechanical properties of the mouse tibia. In (Buie et al., 2008) no significant effects of radiation were observed on trabecular bone mineral density and tissue mineral density. However, in their study a relatively large voxel size (19 μm) and low radiation dose (188 mGy, 12 scans over 42 weeks) were used, therefore the small effects of radiation are expected. The small variations in mechanical properties observed in this study between the right and left limb for most mice are consistent with the small effects found on cortical parameters, as the overall mechanical properties of the mouse tibia under uniaxial compression are mainly determined by cortical bone (Paragraph 3.3.6). For some mice, large differences were observed between the left and right tibiae (up to 42%), which however were not likely associated with radiation since reduced or increased mechanical properties were not consistently found for the right limb. In this study, it was assumed that the right and left tibiae had the same homogeneous material properties, therefore the observed differences could be more likely associated to geometrical factors, e.g. the alignment and curvature of the tibia. This could be evaluated by analysing the correlation between geometrical (e.g. cross-sectional moments of inertia along the longitudinal direction) and mechanical properties, which will be the objective of further investigations.

The main limitation of this study is the small sample size (N = 4-6 mice/group), which can reduce the ability of identifying significant effects of radiation. Nevertheless, in previous studies larger percentage variations and significant differences were identified for similar sample sizes (N = 4-8 mice/group) (Klinck et al., 2008, Laperre et al., 2011, Willie et al., 2013), which suggests that the scanning procedure selected in this study actually provoked limited radiation effects. Another limitation is that the observed variations between the right and left limb could potentially be due to other factors in addition to radiation. The results presented in this study are based on the assumption that contralateral limbs are not significantly different at baseline, as reported in previous studies for mice of different species (Judex et al., 2005, Margolis et al., 2004). Another potential factor affecting the analysed data is the fact that the right limb was fixed for 25 minutes during scanning in order to avoid moving artifacts in the microCT images. This procedure could potentially have an effect on the limb, e.g. by reducing the blood flow. In order to minimize this effect, during the *in vivo* procedures care has been taken to avoid fixing the limb too tight. After the scan, no apparent discomfort was observed, since mice quickly recovered their normal walking activity. Lastly, it should be noticed that in this study only the macroscopic effects of radiation were analysed, while the cell-level mechanisms resulting in potential bone loss were not investigated. Previous studies have reported reduced cell proliferation in radiated osteoblasts *in vitro* (Gal et al., 2000, Matsumura et al., 1996) and increased number of osteoclasts in mice which underwent whole-body irradiation (Willey et al., 2008). However, these effects have only been observed at much higher radiation doses (more than 2 Gy) compared to those used for *in vivo* imaging, therefore such mechanisms are still unclear. In the framework of using microCT for *in vivo* longitudinal imaging, the aim of this study was to quantify if radiation could potentially affect the longitudinal measurements of bone changes due to interventions. Higher impact on bone properties has been reported for possible interventions of interest, especially on trabecular parameters which were more influenced by radiation, e.g. *in vivo* compressive loading provoked +21-107% trabecular bone volume, +31-68% trabecular thickness (Main et al., 2014). Therefore, the observed radiation effects would have a minor influence on the measured changes. In conclusion, this method can be considered suitable for analysing the effects of bone interventions longitudinally.

5.5 CONCLUSION

In this study the effect of repeated *in vivo* microCT imaging has been evaluated on the mouse tibia of C57BL/6 mice and BalbC mice. Radiation had minimal or no significant effect on the morphometric, densitometric and mechanical properties of the mouse tibia, therefore the selected scanning procedure can be considered an adequate compromise between image quality and radiation exposure. In future studies, it will be applied for the longitudinal investigation of the effects of bone interventions, including anabolic drugs and mechanical loading, on the whole mouse tibia.

CHAPTER 6

CONCLUSIONS

6.1 CONCLUSIONS

Longitudinal studies on preclinical models are important to investigate bone remodeling and the effect of bone interventions (Waarsing et al., 2004a). In particular, the mouse tibia is commonly used in this research field (Birkhold et al., 2016, Holguin et al., 2014) since its changes can be monitored over space and time using *in vivo* micro-Computed Tomography (microCT) imaging, which provides geometrical and densitometric information with high resolution (Bouxsein et al., 2010). Additionally, micro-Finite Element (microFE) models can be generated from microCT images (van Rietbergen et al., 1995) and used to predict the mechanical properties of the tibia non-invasively and how they are affected by bone treatments. Nevertheless, previous studies have shown that repeated *in vivo* microCT scans can provoke significant variations in the bone properties (Klinck et al., 2008, Laperre et al., 2011, Willie et al., 2013), which can affect the accuracy of longitudinal measurements. Therefore it is necessary to find a compromise between image quality and radiation dose induced on the animal at each scan. Additionally, a comprehensive validation of the microCT-based microFE models of the mouse tibia is needed. So far, FE predictions have been validated against strain gauge measurements (Patel et al., 2014, Stadelmann et al., 2009) and Digital Image Correlation (DIC) measurements (Pereira et al., 2015), however these methods cannot provide volumetric measurements of strains or displacements over the whole bone volume under loading.

The aim of this PhD project was to define the best practice for selecting and validating the *in vivo* microCT scanning protocol for evaluating the morphometric, densitometric and biomechanical properties of the mouse tibia in preclinical studies. This has been achieved through three main objectives, described in Chapter 3, Chapter 4 and Chapter 5 respectively.

In Chapter 3, four scanning protocols have been tested, characterised by decreasing integration time and nominal radiation dose in order to define the best one for *in vivo* application. For each protocol, the accuracy of the image-based measurements of morphometric, densitometric and mechanical properties of the tibia has been evaluated, by comparing the obtained values against those measured from high resolution images (4.3 µm voxel size). The selected scanning protocol (energy 55 kVp, current 145 µA, voxel size 10.4 µm, integration time 100 ms, field of view 32 mm, 750 projections/180°, no frame averaging, 0.5 mm Al filter) is associated with a nominal radiation dose of 256 mGy, which is 50% lower compared to the scanning procedure used for previous studies performed in our group (Lu et al., 2017). Maximum differences in measurement errors between the two procedures were 7% for morphometric parameters, 4% for local BMC and 1% for microFE estimations of stiffness and strength.

In Chapter 4, microFE predictions of local displacements in the tibia under loading and structural mechanical properties have been validated, against Digital Volume Correlation (DVC) measurements. DVC can provide volumetric measurements of local displacements and has been recently used for validating FE models of trabecular bone specimens (Chen et al., 2017, Zauel et al., 2005) and porcine vertebrae (Costa et al., 2017). Root mean square errors in the predicted local displacements magnitude were in the range of 5 – 22%, while higher errors were associated with the Cartesian components of displacements. Errors in the prediction of structural mechanical properties were 14 ± 11% for stiffness and 9 ± 9% for strength. These results show that simple and efficient homogeneous isotropic linear elastic microFE models can provide reasonable predictions of the tibia mechanical properties. This study established for the first time a protocol for the validation of microFE models of the mouse tibia using the DVC method.

In Chapter 5, the selected scanning protocol has been tested *in vivo* in order to quantify potential radiation effects. The analysis has been conducted on mice of two different strains (C57BL/6 and BalbC) and interventions (wild type WT and ovariectomy OVX). The right tibia has been scanned *in vivo* five times (every two weeks), while the left one has been used as non-irradiated control. Non-significant or minimal radiation effects have been found on the morphometric, densitometric and mechanical properties of the tibia.

In the future, the selected protocol will be used for investigating the effect of bone interventions, including ovariectomy, as a model of osteoporosis, and anabolic treatments, such as *in vivo* passive compression (De Souza et al., 2005), parathyroid hormone (PTH) (Levchuk et al., 2014) and their combination. The defined workflow is also optimal to validate multi-scale models of bone remodeling, by comparing the model predictions of local bone apposition and resorption to the measured longitudinal changes. Lastly, the same method can be applied for evaluating the effect of bone defects (e.g. metastatic lesions) on the mechanical properties of bone.

Future work will also focus on validating more complex microFE models of the tibia. In particular, implementing smooth meshes could improve the local peaks of errors found for local displacements, while the higher errors found for displacements in the transverse directions compared to the longitudinal ones could be improved by implementing anisotropic material properties in the model. The prediction of bone strength, which is a relevant endpoint when studying the effect of interventions, will be further investigated by testing different failure criteria and comparing the obtained predictions with experimental measurements of failure load in compression. The models can also be used to investigate the relationship between mechanical properties and morphometric and densitometric parameters.

Lastly, the workflow will be implemented in a web-service for the automatic estimation of the tibia properties, in order to allow other researchers, including biologists and engineers, to use the methods developed. This can potentially facilitate the comparison between different studies and reduce the number of animals needed for preclinical investigations.

In conclusion, in this work a scanning procedure for *in vivo* microCT imaging of the whole mouse tibia has been defined and validated, which can be used for evaluating the morphometric, densitometric and mechanical properties of the bone in longitudinal studies.

REFERENCES

ANDERSON, A. E., ELLIS, B. J. & WEISS, J. A. 2007. Verification, validation and sensitivity studies in computational biomechanics. Computer Methods in Biomechanics and Biomedical Engineering, 10, 171-184.

BAB, I. A., HAJBI-YONISSI, C., GABET, Y. & MÜLLER, R. 2007. Micro-tomographic atlas of the mouse skeleton, Springer Science & Business Media.

BARBER, D. C. & HOSE, D. R. 2005. Automatic segmentation of medical images using image registration: diagnostic and simulation applications. Journal of Medical Engineering & Technology, 29, 53-63.

BARBER, D. C., OUBEL, E., FRANGI, A. F. & HOSE, D. R. 2007. Efficient computational fluid dynamics mesh generation by image registration. Medical Image Analysis, 11, 648-662.

BARTH, H. D., LAUNEY, M. E., MACDOWELL, A. A., AGER, J. W. & RITCHIE, R. O. 2010. On the effect of X-ray irradiation on the deformation and fracture behavior of human cortical bone. Bone, 46, 1475-1485.

BAY, B. K., SMITH, T. S., FYHRIE, D. P. & SAAD, M. 1999. Digital volume correlation: Three-dimensional strain mapping using X-ray tomography. Experimental Mechanics, 39, 217-226.

BAYRAKTAR, H. H., MORGAN, E. F., NIEBUR, G. L., MORRIS, G. E., WONG, E. K. & KEAVENY, T. M. 2004. Comparison of the elastic and yield properties of human femoral trabecular and cortical bone tissue. Journal of Biomechanics, 37, 27-35.

BEGONIA, M., DALLAS, M., JOHNSON, M. L. & THIAGARAJAN, G. 2017. Comparison of strain measurement in the mouse forearm using subject-specific finite element models, strain gaging, and digital image correlation. Biomechanics and Modeling in Mechanobiology, 16, 1243-1253.

BIRKHOLD, A. I., RAZI, H., DUDA, G. N., WEINKAMER, R., CHECA, S. & WILLIE, B. M. 2014a. Mineralizing surface is the main target of mechanical stimulation independent of age: 3D dynamic in vivo morphometry. Bone, 66, 15-25.

BIRKHOLD, A. I., RAZI, H., DUDA, G. N., WEINKAMER, R., CHECA, S. & WILLIE, B. M. 2014b. The influence of age on adaptive bone formation and bone resorption. Biomaterials, 35, 9290-9301.

BIRKHOLD, A. I., RAZI, H., DUDA, G. N., WEINKAMER, R., CHECA, S. & WILLIE, B. M. 2016. The Periosteal Bone Surface is Less Mechano-Responsive than the Endocortical. Scientific Reports, 6, 23480.

BIRKHOLD, A. I., RAZI, H., WEINKAMER, R., DUDA, G. N., CHECA, S. & WILLIE, B. M. 2015. Monitoring in vivo (re)modeling: A computational approach using 4D microCT data to quantify bone surface movements. Bone, 75, 210-221.

BORTEL, E. L., DUDA, G. N., MUNDLOS, S., WILLIE, B. M., FRATZL, P. & ZASLANSKY, P. 2015. Long bone maturation is driven by pore closing: A quantitative tomography investigation of structural formation in young C57BL/6 mice. Acta Biomaterialia, 22, 92 - 102.

BOUXSEIN, M. L., BOYD, S. K., CHRISTIANSEN, B. A., GULDBERG, R. E., JEPSEN, K. J. & MÜLLER, R. 2010. Guidelines for assessment of bone microstructure in rodents using micro–computed tomography. Journal of Bone and Mineral Research, 25, 1468-1486.

BOYD, S. K., DAVISON, P., MÜLLER, R. & GASSER, J. A. 2006a. Monitoring individual morphological changes over time in ovariectomized rats by in vivo micro-computed tomography. Bone, 39, 854-862.

BOYD, S. K., MOSER, S., KUHN, M., KLINCK, R. J., KRAUZE, P. L., MÜLLER, R. & GASSER, J. A. 2006b. Evaluation of Three-dimensional Image Registration Methodologies for In Vivo Micro-computed Tomography. Annals of Biomedical Engineering, 34, 1587-1599.

BRODT, M. D., ELLIS, A. B. & SILVA, M. J. 2009. Growing C57Bl/6 Mice Increase Whole Bone Mechanical Properties by Increasing Geometric and Material Properties. Journal of Bone and Mineral Research, 14, 2159-2166.

BRODT, M. D. & SILVA, M. J. 2010. Aged mice have enhanced endocortical response and normal periosteal response compared with young-adult mice following 1 week of axial tibial compression. Journal of Bone and Mineral Research, 25, 2006-2015.

BUIE, H. R., CAMPBELL, G. M., KLINCK, R. J., MACNEIL, J. A. & BOYD, S. K. 2007. Automatic segmentation of cortical and trabecular compartments based on a dual threshold technique for in vivo micro-CT bone analysis. Bone, 41, 505-515.

BUIE, H. R., MOORE, C. P. & BOYD, S. K. 2008. Postpubertal architectural developmental patterns differ between the L3 vertebra and proximal tibia in three inbred strains of mice. Journal of Bone and Mineral Research, 23, 2048-2059.

BURNETT, D. S. 1987. Finite element analysis: from concepts to applications, Prentice Hall.

CAMPBELL, G., TIWARI, S., GRUNDMANN, F., PURCZ, N., SCHEM, C. & GLÜER, C.-C. 2014. Three-dimensional Image Registration Improves the Long-term Precision of In Vivo Micro-Computed Tomographic Measurements in Anabolic and Catabolic Mouse Models. Calcified Tissue International, 94, 282-292.

CAMPBELL, G. M. & SOPHOCLEOUS, A. 2014. Quantitative analysis of bone and soft tissue by micro-computed tomography: applications to ex vivo and in vivo studies. BoneKEy Rep, 3.

CARNELLI, D., LUCCHINI, R., PONZONI, M., CONTRO, R. & VENA, P. 2011. Nanoindentation testing and finite element simulations of cortical bone allowing for anisotropic elastic and inelastic mechanical response. Journal of Biomechanics, 44, 1852-1858.

CARRIERO, A., ABELA, L., PITSILLIDES, A. A. & SHEFELBINE, S. J. 2014. Ex vivo determination of bone tissue strains for an in vivo mouse tibial loading model. Journal of Biomechanics, 47, 2490-2497.

CHEN, Y., DALL'ARA, E., SALES, E., MANDA, K., WALLACE, R., PANKAJ, P. & VICECONTI, M. 2017. Micro-CT based finite element models of cancellous bone predict accurately displacement once the boundary condition is well replicated: A validation study. Journal of the Mechanical Behavior of Biomedical Materials, 65, 644-651.

CHRISTIANSEN, B. A. 2016. Effect of micro-computed tomography voxel size and segmentation method on trabecular bone microstructure measures in mice. Bone Reports, 5, 136-140.

COSTA, M. C., TOZZI, G., CRISTOFOLINI, L., DANESI, V., VICECONTI, M. & DALL'ARA, E. 2017. Micro Finite Element models of the vertebral body: Validation of local displacement predictions. PLOS ONE, 12, e0180151.

COWIN, S. C., VAN BUSKIRK, W. C. & ASHMAN, R. B. 1987. Properties of bone. Handbook of bioengineering. McGraw-Hill New York.

CURREY, J. D. 1988. The effect of porosity and mineral content on the Young's modulus of elasticity of compact bone. Journal of Biomechanics, 21, 131-139.

DALL'ARA, E., BARBER, D. & VICECONTI, M. 2014. About the inevitable compromise between spatial resolution and accuracy of strain measurement for bone tissue: A 3D zero-strain study. Journal of Biomechanics, 47, 2956-2963.

DALL'ARA, E., BOUDIFFA, M., TAYLOR, C., SCHUG, D., FIEGLE, E., KENNERLEY, A. J., DAMIANOU, C., TOZER, G. M., KIESSLING, F. & MÜLLER, R. 2016. Longitudinal imaging of the ageing mouse. Mechanisms of Ageing and Development, 160, 93-116.

DALL'ARA, E., PAHR, D., VARGA, P., KAINBERGER, F. & ZYSSET, P. 2012. QCT-based finite element models predict human vertebral strength in vitro significantly better than simulated DEXA. Osteoporosis International, 23, 563-572.

DALL'ARA, E., PEÑA-FERNÁNDEZ, M., PALANCA, M., GIORGI, M., CRISTOFOLINI, L. & TOZZI, G. 2017. Precision of Digital Volume Correlation Approaches for Strain Analysis in Bone Imaged with Micro-Computed Tomography at Different Dimensional Levels. Frontiers in Materials, 4, 31.

DE SOUZA, R. L., MATSUURA, M., ECKSTEIN, F., RAWLINSON, S. C. F., LANYON, L. E. & PITSILLIDES, A. A. 2005. Non-invasive axial loading of mouse tibiae increases cortical bone formation and modifies trabecular organization: a new model to study cortical and cancellous compartments in a single loaded element. Bone, 37, 810-818.

DUDEK, M., GOSSAN, N., YANG, N., IM, H.-J., RUCKSHANTHI, J. P. D., YOSHITANE, H., LI, X., JIN, D., WANG, P., BOUDIFFA, M., BELLANTUONO, I., FUKADA, Y., BOOT-HANDFORD, R. P. & MENG, Q.-J. 2016. The chondrocyte clock gene Bmal1 controls cartilage homeostasis and integrity. The Journal of Clinical Investigation, 126, 365-376.

EASLEY, S. K., JEKIR, M. G., BURGHARDT, A. J., LI, M. & KEAVENY, T. M. 2010. Contribution of the intra-specimen variations in tissue mineralization to PTH- and raloxifene-induced changes in stiffness of rat vertebrae. BONE, 46, 1162-1169.

FAGAN, M. 1996. Finite element analysis.

FAGAN, M. J., JULIAN, S. & MOHSEN, A. M. 2002. Finite element analysis in spine research. Proceedings of the Institution of Mechanical Engineers, Part H: Journal of Engineering in Medicine, 216, 281-298.

FELDKAMP, L. A., GOLDSTEIN STEVEN, A., PARFITT MICHAEL, A., JESION, G. & KLEEREKOPER, M. 1989. The direct examination of three-dimensional bone architecture in vitro by computed tomography. Journal of Bone and Mineral Research, 4, 3-11.

FOX, J. & LONG, J. S. 1990. Modern methods of data analysis. Newbury Park, CA: Sage Publications,| c1990, edited by Fox, John; Long, J. Scott.

FRATZL, P. & WEINKAMER, R. 2007. Nature's hierarchical materials. Progress in Materials Science, 52, 1263-1334.

FRITTON, J. C., MYERS, E. R., WRIGHT, T. M. & VAN DER MEULEN, M. C. H. 2005. Loading induces site-specific increases in mineral content assessed by microcomputed tomography of the mouse tibia. Bone, 36, 1030-1038.

FUCHS, R. K., BAUER, J. J. & SNOW, C. M. 2001. Jumping Improves Hip and Lumbar Spine Bone Mass in Prepubescent Children: A Randomized Controlled Trial. Journal of Bone and Mineral Research, 16, 148-156.

GAL, T. J., MUNOZ-ANTONIA, T., MURO-CACHO, C. A. & KLOTCH, D. W. 2000. Radiation effects on osteoblasts in vitro: A potential role in osteoradionecrosis. Archives of Otolaryngology–Head & Neck Surgery, 126, 1124-1128.

GILLARD, F., BOARDMAN, R., MAVROGORDATO, M., HOLLIS, D., SINCLAIR, I., PIERRON, F. & BROWNE, M. 2014. The application of digital volume correlation (DVC) to study the microstructural behaviour of trabecular bone during compression. Journal of the Mechanical Behavior of Biomedical Materials, 29, 480-499.

GIORGI, M. & DALL'ARA, E. 2018. Variability in strain distribution in the mice tibia loading model: A preliminary study using digital volume correlation. Medical Engineering & Physics, 62, 7-16.

GLATT, V., CANALIS, E., STADMEYER, L. & BOUXSEIN, M. L. 2007. Age-related changes in trabecular architecture differ in female and male C57BL/6J mice. Journal of Bone and Mineral Research, 22, 1197-1207.

GRASSI, L. & ISAKSSON, H. 2015. Extracting accurate strain measurements in bone mechanics: A critical review of current methods. Journal of the Mechanical Behavior of Biomedical Materials, 50, 43-54.

GROSS, T., PAHR, D. H., PEYRIN, F. & ZYSSET, P. K. 2012. Mineral heterogeneity has a minor influence on the apparent elastic properties of human cancellous bone: a SRμCT-based finite element study. Computer Methods in Biomechanics and Biomedical Engineering, 15, 1137-1144.

HILTUNEN, A., VUORIO, E. & ARO HANNU, T. 1993. A standardized experimental fracture in the mouse tibia. Journal of Orthopaedic Research, 11, 305-312.

HOLGUIN, N., BRODT, M. D., SANCHEZ, M. E., KOTIYA, A. A. & SILVA, M. J. 2013. Adaptation of tibial structure and strength to axial compression depends on loading history in both C57BL/6 and BALB/c mice. Calcified Tissue International, 93, 211-221.

HOLGUIN, N., BRODT, M. D., SANCHEZ, M. E. & SILVA, M. J. 2014. Aging diminishes lamellar and woven bone formation induced by tibial compression in adult C57BL/6. Bone, 65, 83-91.

HOSHI, A., WATANABE, H., CHIBA, M. & INABA, Y. 1998. Effects of exercise at different ages on bone density and mechanical properties of femoral bone of aged mice. The Tohoku Journal of Experimental Medicine, 185, 15-24.

HOU, F. J., LANG, S. M., HOSHAW, S. J., REIMANN, D. A. & FYHRIE, D. P. 1998. Human vertebral body apparent and hard tissue stiffness. Journal of Biomechanics, 31, 1009-1015.

HUISKES, R. 2000. If bone is the answer, then what is the question? Journal of Anatomy, 197, 145-156.

HUSSEIN, A. I., BARBONE, P. E. & MORGAN, E. F. 2012. Digital Volume Correlation for Study of the Mechanics of Whole Bones. Procedia IUTAM, 4, 116-125.

JOHNELL, O. & KANIS, J. 2005. Epidemiology of osteoporotic fractures. Osteoporosis International, 16, S3-S7.

JUDEX, S., CHUNG, H., TORAB, A., XIE, L., RUBIN, C., DONAHUE, L. R. & XU, S. 2005. Micro-CT induced radiation does not exacerbate disuse related bone loss. 2005 2005.

JÄMSÄ, T., JALOVAARA, P., PENG, Z., VÄÄNÄNEN, H. K. & TUUKKANEN, J. 1998. Comparison of three-point bending test and peripheral quantitative computed tomography analysis in the evaluation of the strength of mouse femur and tibia. Bone, 23, 155-161.

KAMEO, Y., TSUBOTA, K. & ADACHI, T. 2018. Bone Adaptation: In Silico Approach, Springer Japan.

KATO, T., TERASHIMA, T., YAMASHITA, T., HATANAKA, Y., HONDA, A. & UMEMURA, Y. 2005. Effect of low-repetition jump training on bone mineral density in young women. Journal of Applied Physiology, 100, 839-843.

KAZAKIA, G. J., BURGHARDT, A. J., CHEUNG, S. & MAJUMDAR, S. 2008. Assessment of bone tissue mineralization by conventional x-ray microcomputed tomography: comparison with synchrotron radiation microcomputed tomography and ash measurements. MED PHYS, 35, 3170-3179.

KHODABAKHSHI, G., WALKER, D., SCUTT, A., WAY, L., COWIE, R. M. & HOSE, D. R. 2013. Measuring three-dimensional strain distribution in tendon. Journal of Microscopy, 249, 195-205.

KLINCK, R. J., CAMPBELL, G. M. & BOYD, S. K. 2008. Radiation effects on bone architecture in mice and rats resulting from in vivo micro-computed tomography scanning. Medical Engineering & Physics, 30, 888-895.

KOHLER, T., STAUBER, M., DONAHUE, L. R. & MÜLLER, R. 2007. Automated compartmental analysis for high-throughput skeletal phenotyping in femora of genetic mouse models. Bone, 41, 659-667.

LAIB, A., KUMER, J. L., MAJUMDAR, S. & LANE, N. E. 2001. The Temporal Changes of Trabecular Architecture in Ovariectomized Rats Assessed by MicroCT. Osteoporosis International, 12, 936-941.

LAPERRE, K., DEPYPERE, M., VAN GASTEL, N., TORREKENS, S., MOERMANS, K., BOGAERTS, R., MAES, F. & CARMELIET, G. 2011. Development of micro-CT protocols for in vivo follow-up of mouse bone architecture without major radiation side effects. Bone, 49, 613-622.

LEPPÄNEN, O. V., SIEVÄNEN, H., JOKIHAARA, J., PAJAMÄKI, I., KANNUS, P. & JÄRVINEN, T. L. N. 2008. Pathogenesis of Age-Related Osteoporosis: Impaired Mechano-Responsiveness of Bone Is Not the Culprit. PLoS ONE, 3, e2540.

LEVCHUK, A., ZWAHLEN, A., WEIGT, C., LAMBERS, F. M., BADILATTI, S. D., SCHULTE, F. A., KUHN, G. & MÜLLER, R. 2014. The Clinical Biomechanics Award 2012 - presented by the European Society of Biomechanics: large scale simulations of trabecular bone adaptation to loading and treatment. Clinical Biomechanics, 29, 355-362.

LI, W., CHEN, W. & LIN, Y. 2015. The Efficacy of Parathyroid Hormone Analogues in Combination With Bisphosphonates for the Treatment of Osteoporosis: A Meta-Analysis of Randomized Controlled Trials. Medicine, 94, e1156.

LIU, L. & MORGAN, E. F. 2007. Accuracy and precision of digital volume correlation in quantifying displacements and strains in trabecular bone. Journal of Biomechanics, 40, 3516-3520.

LU, Y., BOUDIFFA, M., DALL, ARA, E., BELLANTUONO, I. & VICECONTI, M. 2015. Evaluation of in-vivo measurement errors associated with micro-computed tomography scans by means of the bone surface distance approach. MED ENG PHYS, 37, 1091-1097.

LU, Y., BOUDIFFA, M., DALL'ARA, E., BELLANTUONO, I. & VICECONTI, M. 2016. Development of a protocol to quantify local bone adaptation over space and time: Quantification of reproducibility. Journal of Biomechanics, 2095 - 2099.

LU, Y., BOUDIFFA, M., DALL’ARA, E., LIU, Y., BELLANTUONO, I. & VICECONTI, M. 2017. Longitudinal effects of Parathyroid Hormone treatment on morphological, densitometric and mechanical properties of mouse tibia. Journal of the Mechanical Behavior of Biomedical Materials, 75, 244-251.

MAIN, R. P., LYNCH, M. E. & VAN DER MEULEN, M. C. H. 2010. In vivo tibial stiffness is maintained by whole bone morphology and cross-sectional geometry in growing female mice. Journal of Biomechanics, 43, 2689-2694.

MAIN, R. P., LYNCH, M. E. & VAN DER MEULEN, M. C. H. 2014. Load-induced changes in bone stiffness and cancellous and cortical bone mass following tibial compression diminish with age in female mice. The Journal of Experimental Biology, 217, 1775-1783.

MARGOLIS, D. S., LIEN, Y.-H. H., LAI, L.-W. & SZIVEK, J. A. 2004. Bilateral symmetry of biomechanical properties in mouse femora. Medical Engineering & Physics, 26, 349-353.

MARTÍN-BADOSA, E., AMBLARD, D., NUZZO, S., ELMOUTAOUAKKIL, A., VICO, L. & PEYRIN, F. 2003. Excised Bone Structures in Mice: Imaging at Three-dimensional Synchrotron Radiation Micro CT. Radiology, 229, 921-928.

MATSUMURA, S., JIKKO, A., HIRANUMA, H., DEGUCHI, A. & FUCHIHATA, H. 1996. Effect of X-Ray Irradiation on Proliferation and Differentiation of Osteoblast. Calcified Tissue International, 59, 307-308.

MEAKIN, L. B., TODD, H., DELISSER, P. J., GALEA, G. L., MOUSTAFA, A., LANYON, L. E., WINDAHL, S. H. & PRICE, J. S. 2017. Parathyroid hormone's enhancement of bones' osteogenic response to loading is affected by ageing in a dose- and time-dependent manner. Bone, 98, 59-67.

MEIJERING, E. H. W. Spline interpolation in medical imaging: Comparison with other convolution-based approaches. Signal Processing Conference, 2000 10th European, 4-8 Sept. 2000 2000. 1-8.

MEINEL, L., FAJARDO, R., HOFMANN, S., LANGER, R., CHEN, J., SNYDER, B., VUNJAK-NOVAKOVIC, G. & KAPLAN, D. 2005. Silk implants for the healing of critical size bone defects. Bone, 37, 688-698.

MELTON, L. J., III, GABRIEL, S. E., CROWSON, C. S., TOSTESON, A. N. A., JOHNELL, O. & KANIS, J. A. 2003. Cost-equivalence of different osteoporotic fractures. Osteoporosis International, 14, 383-388.

MOHANTY, S. T., KOTTAM, L., GAMBARDELLA, A., NICKLIN, M. J., COULTON, L., HUGHES, D., WILSON, A. G., CROUCHER, P. I. & BELLANTUONO, I. 2010. Alterations in the self-renewal and differentiation ability of bone marrow mesenchymal stem cells in a mouse model of rheumatoid arthritis. Arthritis Research & Therapy, 12, R149-R149.

MOUSTAFA, A., SUGIYAMA, T., PRASAD, J., ZAMAN, G., GROSS, T. S., LANYON, L. E. & PRICE, J. S. 2012. Mechanical loading-related changes in osteocyte sclerostin expression in mice are more closely associated with the subsequent osteogenic response than the peak strains engendered. Osteoporosis International, 23, 1225-1234.

MULDER, L., KOOLSTRA, J. H. & VAN EIJDEN, T. M. G. J. 2004. Accuracy of microCT in the quantitative determination of the degree and distribution of mineralization in developing bone. Acta Radiologica, 45, 769-777.

NAZARIAN, A., SNYDER, B. D., ZURAKOWSKI, D. & MÜLLER, R. 2008. Quantitative micro-computed tomography: A non-invasive method to assess equivalent bone mineral density. Bone, 43, 302-311.

NEER, R. M., ARNAUD, C. D., ZANCHETTA, J. R., PRINCE, R., GAICH, G. A., REGINSTER, J. Y., HODSMAN, A. B., ERIKSEN, E. F., ISH-SHALOM, S., GENANT, H. K., WANG, O. & MITLAK, B. H. 2001. Effect of parathyroid hormone (1-34) on fractures and bone mineral density in postmenopausal women with osteoporosis. The New England Journal of Medicine, 344, 1434-1441.

NISHIYAMA, K. K., CAMPBELL, G. M., KLINCK, R. J. & BOYD, S. K. 2010. Reproducibility of bone micro-architecture measurements in rodents by in vivo micro-computed tomography is maximized with three-dimensional image registration. Bone, 46, 155-161.

NUZZO, S., PEYRIN, F., CLOETENS, P., BARUCHEL, J. & BOIVIN, G. 2002. Quantification of the degree of mineralization of bone in three dimensions using synchrotron radiation microtomography. Medical Physics, 29, 2672-2681.

OLIVIERO, S., LU, Y., VICECONTI, M. & DALL'ARA, E. 2017. Effect of integration time on the morphometric, densitometric and mechanical properties of the mouse tibia. Journal of Biomechanics, 65, 203-211.

PALANCA, M., BODEY, A. J., GIORGI, M., VICECONTI, M., LACROIX, D., CRISTOFOLINI, L. & DALL'ARA, E. 2017. Local displacement and strain uncertainties in different bone types by digital volume correlation of synchrotron microtomograms. Journal of Biomechanics, 58, 27-36.

PALANCA, M., TOZZI, G., CRISTOFOLINI, L., VICECONTI, M. & DALL'ARA, E. 2015. Three-dimensional local measurements of bone strain and displacement: comparison of three digital volume correlation approaches. Journal of Biomechanical Engineering, 137, 071006-1 - 071006-14.

PATEL, T. K., BRODT, M. D. & SILVA, M. J. 2014. Experimental and finite element analysis of strains induced by axial tibial compression in young-adult and old female C57Bl/6 mice. Journal of Biomechanics, 47, 451-457.

PEREIRA, A. F., JAVAHERI, B., PITSILLIDES, A. A. & SHEFELBINE, S. J. 2015. Predicting cortical bone adaptation to axial loading in the mouse tibia. Journal of The Royal Society Interface, 12.

PISTOIA, W., VAN RIETBERGEN, B., LOCHMÜLLER, E. M., LILL, C. A., ECKSTEIN, F. & RÜEGSEGGER, P. 2002. Estimation of distal radius failure load with micro-finite element analysis models based on three-dimensional peripheral quantitative computed tomography images. Bone, 30, 842-848.

POLGAR, K., VICECONTI, M. & CONNOR, J. J. 2001. A comparison between automatically generated linear and parabolic tetrahedra when used to mesh a human femur. Proceedings of the Institution of Mechanical Engineers, Part H: Journal of Engineering in Medicine, 215, 85-94.

RAZI, H., BIRKHOLD, A. I., ZASLANSKY, P., WEINKAMER, R., DUDA, G. N., WILLIE, B. M. & CHECA, S. 2015. Skeletal maturity leads to a reduction in the strain magnitudes induced within the bone: a murine tibia study. Acta Biomaterialia, 13, 301-310.

RAZI, H., BIRKHOLD, A. I., ZEHN, M., DUDA, G. N., WILLIE, B. M. & CHECA, S. 2014. A finite element model of in vivo mouse tibial compression loading: influence of boundary conditions. Facta Universitatis, Series: Mechanical Engineering, 12, 195-207.

RITMAN, E. L. 2004. Micro-Computed Tomography—Current Status and Developments. Annual Review of Biomedical Engineering, 6, 185-208.

ROBERTS, B. C., PERILLI, E. & REYNOLDS, K. J. 2014. Application of the digital volume correlation technique for the measurement of displacement and strain fields in bone: A literature review. Journal of Biomechanics, 47, 923-934.

SCHILEO, E., DALL'ARA, E., TADDEI, F., MALANDRINO, A., SCHOTKAMP, T., BALEANI, M. & VICECONTI, M. 2008. An accurate estimation of bone density improves the accuracy of subject-specific finite element models. Journal of Biomechanics, 41, 2483-2491.

SCHRIEFER, J. L., ROBLING, A. G., WARDEN, S. J., FOURNIER, A. J., MASON, J. J. & TURNER, C. H. 2005. A comparison of mechanical properties derived from multiple skeletal sites in mice. Journal of Biomechanics, 38, 467-475.

SCHULTE, F. A., RUFFONI, D., LAMBERS, F. M., CHRISTEN, D., WEBSTER, D. J., KUHN, G. & MÜLLER, R. 2013a. Local mechanical stimuli regulate bone formation and resorption in mice at the tissue level. PLoS ONE, 8, e62172-e62172.

SCHULTE, F. A., ZWAHLEN, A., LAMBERS, F. M., KUHN, G., RUFFONI, D., BETTS, D., WEBSTER, D. J. & MÜLLER, R. 2013b. Strain-adaptive in silico modeling of bone adaptation--a computer simulation validated by in vivo micro-computed tomography data. Bone, 52, 485-492.

SCHWIEDRZIK, J., GROSS, T., BINA, M., PRETTERKLIEBER, M., ZYSSET, P. & PAHR, D. 2016. Experimental validation of a nonlinear μFE model based on cohesive-frictional plasticity for trabecular bone. International Journal for Numerical Methods in Biomedical Engineering, 32, e02739-n/a.

SILVA, M. J., BRODT, M. D. & HUCKER, W. J. 2005. Finite element analysis of the mouse tibia: estimating endocortical strain during three-point bending in SAMP6 osteoporotic mice. The Anatomical Record Part A, 283, 380-390.

SILVA, M. J., BRODT, M. D., LYNCH, M. A., STEPHENS, A. L., WOOD, D. J. & CIVITELLI, R. 2012. Tibial loading increases osteogenic gene expression and cortical bone volume in mature and middle-aged mice. PLoS ONE, 7, e34980-e34980.

SILVA, M. J. & GIBSON, L. J. 1997. Modeling the mechanical behavior of vertebral trabecular bone: Effects of age-related changes in microstructure. Bone, 21, 191-199.

SRINIVASAN, S., AGANS, S. C., KING, K. A., MOY, N. Y., POLIACHIK, S. L. & GROSS, T. S. 2003. Enabling bone formation in the aged skeleton via rest-inserted mechanical loading. Bone, 33, 946-955.

STADELMANN, V. A., BONNET, N. & PIOLETTI, D. P. 2011. Combined effects of zoledronate and mechanical stimulation on bone adaptation in an axially loaded mouse tibia. Clinical Biomechanics, 26, 101-105.

STADELMANN, V. A., HOCKE, J., VERHELLE, J., FORSTER, V., MERLINI, F., TERRIER, A. & PIOLETTI, D. P. 2009. 3D strain map of axially loaded mouse tibia: a numerical analysis validated by experimental measurements. Computer Methods in Biomechanics and Biomedical Engineering, 12, 95-100.

STAUBER, M. & MÜLLER, R. 2008. Micro-Computed Tomography: A Method for the Non-Destructive Evaluation of the Three-Dimensional Structure of Biological Specimens. In: WESTENDORF, J. J. (ed.) Osteoporosis: Methods and Protocols. Totowa, NJ: Humana Press.

SZTEFEK, P., VANLEENE, M., OLSSON, R., COLLINSON, R., PITSILLIDES, A. A. & SHEFELBINE, S. 2010. Using digital image correlation to determine bone surface strains during loading and after adaptation of the mouse tibia. Journal of Biomechanics, 43, 599-605.

TASSANI, S., ÖHMAN, C., BARUFFALDI, F., BALEANI, M. & VICECONTI, M. 2011. Volume to density relation in adult human bone tissue. Journal of Biomechanics, 44, 103-108.

TURNER, C. H., TAKANO, Y. & OWAN, I. 1995. Aging changes mechanical loading thresholds for bone formation in rats. Journal of Bone and Mineral Research, 10, 1544-1549.

ULRICH, D., VAN RIETBERGEN, B., WEINANS, H. & RÜEGSEGGER, P. 1998. Finite element analysis of trabecular bone structure: a comparison of image-based meshing techniques. Journal of Biomechanics, 31, 1187-1192.

VAINIONPÄÄ, A., KORPELAINEN, R., VIHRIÄLÄ, E., RINTA–PAAVOLA, A., LEPPÄLUOTO, J. & JÄMSÄ, T. 2006. Intensity of exercise is associated with bone density change in premenopausal women. Osteoporosis International, 17, 455-463.

VAN RIETBERGEN, B., WEINANS, H., HUISKES, R. & ODGAARD, A. 1995. A new method to determine trabecular bone elastic properties and loading using micromechanical finite-element models. Journal of Biomechanics, 28, 69-81.

VAN RUIJVEN, L. J., MULDER, L. & VAN EIJDEN, T. M. G. J. 2007. Variations in mineralization affect the stress and strain distributions in cortical and trabecular bone. Journal of Biomechanics, 40, 1211-1218.

WAARSING, J. H., DAY, J. S., VAN DER LINDEN, J. C., EDERVEEN, A. G., SPANJERS, C., DE CLERCK, N., SASOV, A., VERHAAR, J. A. N. & WEINANS, H. 2004a. Detecting and tracking local changes in the tibiae of individual rats: a novel method to analyse longitudinal in vivo micro-CT data. Bone, 34, 163-169.

WAARSING, J. H., DAY, J. S. & WEINANS, H. 2004b. An Improved Segmentation Method for In Vivo μCT Imaging. Journal of Bone and Mineral Research, 19, 1640-1650.

WALLACE, I. J., JUDEX, S. & DEMES, B. 2015. Effects of load-bearing exercise on skeletal structure and mechanics differ between outbred populations of mice. Bone, 72, 1-8.

WALLACE, R. J., PANKAJ, P. & SIMPSON, A. H. R. W. 2014. Major source of error when calculating bone mechanical properties. J BONE MINER RES, 29, 2697-2697.

WEATHERHOLT, A. M., FUCHS, R. K. & WARDEN, S. J. 2013. Cortical and trabecular bone adaptation to incremental load magnitudes using the mouse tibial axial compression loading model. Bone, 52, 372-379.

WEBSTER, D. J., MORLEY, P. L., VAN LENTHE, G. H. & MÜLLER, R. 2008. A novel in vivo mouse model for mechanically stimulated bone adaptation – a combined experimental and computational validation study. Computer Methods in Biomechanics and Biomedical Engineering, 11, 435-441.

WILLEY, J. S., LLOYD, S. A. J., ROBBINS, M. E., BOURLAND, J. D., SMITH-SIELICKI, H., BOWMAN, L. C., NORRDIN, R. W. & BATEMAN, T. A. 2008. Early Increase in Osteoclast Number in Mice after Whole-Body Irradiation with 2 Gy X Rays. Radiation Research, 170, 388-392.

WILLIE, B. M., BIRKHOLD, A. I., RAZI, H., THIELE, T., AIDO, M., KRUCK, B., SCHILL, A., CHECA, S., MAIN, R. P. & DUDA, G. N. 2013. Diminished response to in vivo mechanical loading in trabecular and not cortical bone in adulthood of female C57Bl/6 mice coincides with a reduction in deformation to load. Bone, 55, 335-346.

WILLINGHAMM, M. D., BRODT, M. D., LEE, K. L., STEPHENS, A. L., YE, J. & SILVA, M. J. 2010. Age-related changes in bone structure and strength in female and male BALB/c mice. Calcified Tissue International, 86, 470-483.

WOLFF, J. 1870. Ueber die innere Architectur der Knochen und ihre Bedeutung für die Frage vom Knochenwachsthum. Archiv für pathologische Anatomie und Physiologie und für klinische Medicin, 50, 389-450.

WOLFF, J. 2010. The Classic: On the Inner Architecture of Bones and its Importance for Bone Growth. Clinical Orthopaedics and Related Research®, 468, 1056-1065.

WOLFRAM, U., WILKE, H.-J. & ZYSSET, P. K. 2010. Valid μ finite element models of vertebral trabecular bone can be obtained using tissue properties measured with nanoindentation under wet conditions. Journal of Biomechanics, 43, 1731-1737.

YANG, H., BUTZ, K. D., DUFFY, D., NIEBUR, G. L., NAUMAN, E. A. & MAIN, R. P. 2014. Characterization of cancellous and cortical bone strain in the in vivo mouse tibial loading model using microCT-based finite element analysis. Bone, 66, 131-139.

YENI, Y. N. & FYHRIE, D. P. 2001. Finite element calculated uniaxial apparent stiffness is a consistent predictor of uniaxial apparent strength in human vertebral cancellous bone tested with different boundary conditions. Journal of Biomechanics, 34, 1649-1654.

ZAUEL, R., YENI, Y. N., BAY, B. K., DONG, X. N. & FYHRIE, D. P. 2005. Comparison of the Linear Finite Element Prediction of Deformation and Strain of Human Cancellous Bone to 3D Digital Volume Correlation Measurements. Journal of Biomechanical Engineering, 128, 1-6.

ZYSSET, P. K., DALL'ARA, E., VARGA, P. & PAHR, D. H. 2013. Finite element analysis for prediction of bone strength. BoneKEy reports, 2, 386-386.